An Atomic Scale View on a Model Catalyst

Pd Nanoparticles on TiO$_2$

An Atomic Scale View on a Model Catalyst

Pd Nanoparticles on TiO$_2$

PROEFSCHRIFT

DOOR

Martin Jacobus Johan Jak

GEBOREN TE OPMEER IN 1971

An atomic scale view on a model catalyst: Pd nanoparticles on TiO$_2$
Martin Jacobus Johan Jak

aan mijn ouders

This thesis is partly based on the following articles:

M.J.J. Jak, C. Konstapel, A. van Kreuningen, J. Verhoeven, R. van Gastel,
and J.W.M. Frenken,
*Automated detection of particles, clusters and islands in Scanning Probe
Microscopy images,* (Chapter 2)
in preparation.

M.J.J. Jak, A. van Kreuningen, J. Chrost, J. Verhoeven, C. Konstapel,
and J.W.M. Frenken,
*Thermische veroudering van een modelkatalysator, 'gezien' met Scanning
Tunneling Microscopie,* (Chapters 3 and 5)
Nevacblad **37**, 67–72 (1999), in dutch.

M.J.J. Jak, A. van Kreuningen, J. Verhoeven, and J.W.M. Frenken,
The effect of stoichiometry on the direction of steps on TiO$_2$(110), (Chapter 4),
in preparation.

M.J.J. Jak, C. Konstapel, A. van Kreuningen, J. Verhoeven, and J.W.M. Frenken,
*Scanning tunnelling microscopy study of the growth of small palladium particles
on TiO$_2$(110),* (Chapter 5)
Surf. Sci. **457**, 295–310 (2000).

M.J.J. Jak, C. Konstapel, A. van Kreuningen, J. Chrost, J. Verhoeven,
and J.W.M. Frenken,
*The influence of substrate defects on the growth rate of palladium nanoparticles
on a TiO$_2$(110) surface,* (Chapter 6)
submitted to Surf. Sci.

M.J.J. Jak, A. van Kreuningen, C. Konstapel, J. Verhoeven and J.W.M. Frenken,
Hydrogen induced reduction of TiO$_2$ and Pd/TiO$_2$ surfaces. (Chapter 7)
in preparation.

Contents

Contents

Contents

I

Introduction

In this chapter I discuss the motivation for the research presented in this thesis. The interest in very small particles, or nanoparticles, originates from their physical properties, which can be vastly different from those of bulk material. They are not only of fundamental importance, but also of interest for many potential applications such as heterogeneous catalysis. We use a microscopic technique with atomic resolution, Scanning Tunneling Microscopy, to study these very small particles in a model geometry, in which they are supported on a flat substrate.

1.1 Size does matter

Very small clusters of atoms form a state of matter that can be considered to lie somewhere in between a bulk solid material and an ensemble of single atoms or molecules. Aggregates of a few, up to several thousands of atoms, show many interesting properties. This was understood already by Mie, who wrote in 1908 [1, 2]

> *"Da Goldatome sich sicher optisch anders verhalten als kleine Goldkügelchen wäre es daher wahrscheinlich sehr interessant, die Absorption der Lösungen mit allerkleinsten amikroskopischen Teilchen zu untersuchen und gewissermaßen optisch den Vorgang zu verfolgen, wie sich die Goldteilchen aus den Atomen aufbauen."*

> — Gustav Mie [1]

Indeed one of the most striking properties of 'nanoparticles' is their optical behaviour [2]. Whereas the optical spectra of single atoms show sharp absorption lines, bulk metals usually show wide absorption bands. When more and more atoms join together lines split and bands develop. On the other hand, when a large

particle is made smaller and smaller, bands open and band gaps grow wider. Therefore the emission wavelengths of small nanocrystals depend on their size and this can be used for example to tune the wavelength of 'quantum dot' lasers [3, 4].

The optical spectrum is not the only difference between small particles and bulk solids. Small clusters often exhibit a whole variety of exceptional physical and chemical properties. Even though their bulk solid counterparts may form close packed crystal structures, nanoparticles may prefer icosahedral or decahedral structures, depending on their size [5]. The higher volume energy involved in these structures can be compensated by a lower surface free energy. Furthermore, nanoparticles have the freedom to contract their lattice constant slightly in response to surface tension [6]. These effects sometimes lead to materials with superior mechanical properties, such as a hardness approaching that of diamond [6]. The stability of small particles can depend strongly on the size. Particles with a specific number of atoms can be significantly more stable than particles with one atom more or one atom less. These 'magic sizes' are caused either by the geometric structure, when the number of atoms is exactly right to fill up all the faces of a polyhedron, or by electronic effects, when the total number of valence electrons in the particle is exactly right to completely fill an electronic shell [7]. Some properties even depend on whether a particle contains an even or odd number of electrons [8].

Besides these exotic features there is another important difference between nanoparticles and bulk solids, namely the ratio between the numbers of surface and bulk atoms. A major fraction of the atoms in a nanometer-size particle is located at the surface whereas this fraction is extremely small for macroscopic crystals. This property can be exploited in processes where surfaces are important, such as catalysis. An illustration of a very small particle, consisting of only 201 atoms is shown in Figure 1.1. Approximately 60 % of the atoms resides at the surface of the particle.

Although the properties of free, isolated clusters, for example in cluster beams, are mainly determined by the number of atoms in the aggregate, interaction with the surroundings can also be very important. In practical applications particles are almost never isolated. Nanoparticles used in optical applications or in new materials with improved mechanical properties are usually embedded in a matrix. In catalysis, the particles are supported on the surface of a support material. The interaction of a cluster with the matrix or support may enhance, weaken
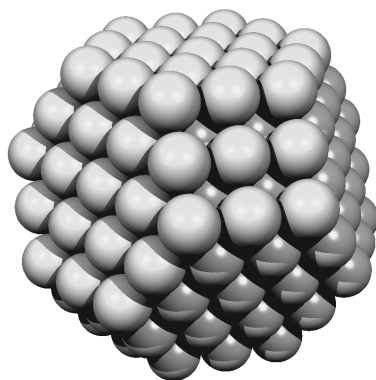
Figure 1.1: *Illustration of a fcc Wulff polyhedron consisting of 201 atoms. The surface consists of ⟨001⟩ and ⟨111⟩ facets. In total 122 atoms are located at the surface, and of these 122, 60 are located at edges or corners.*

or modify many of the effects described above.

1.2 Catalysis

The introduction of catalytic converters in the exhaust line of automobiles was mainly initiated by the US Clean Air Act of 1970 [9]. The purpose of this catalyst is to reduce the emission of harmful gases such as CO, NO_x and hydrocarbons. The introduction in the USA influenced regulations in other countries, and since 1993 all cars within the European Union have to be equipped with such a catalyst.

The concept of catalysis was first introduced by Berzelius in 1836. Later Ostwald defined a catalyst as a compound *which increases the rate of a chemical reaction, but which is not consumed by the reaction*. This definition followed a number of puzzling observations by Davy, Faraday and others at the start of the 19th century. However, catalytic processes had been used long before this time, but since the concept of catalysis was not yet invented they were not recognized as such. Fermentation for example, had already been applied for thousands of years in brewing beer, and making wine and bread. In the Middle Ages sulphuric acid was synthesized, using nitrous vapours as a catalyst [10]. Our own body is one of the places were catalytic reactions play a very important role. Enzymes accelerate reactions that would otherwise require temperatures which destroy most of the

cells, which makes them a vital ingredient of living organisms. Nowadays catalysis is very important in nearly all industrial chemical processes. Catalysts are used to produce the desired products in a cheaper, safer, or for example environmentally more friendly way. Needless to add that catalysis has an enormous economic impact.

If the catalyst is in another phase than the reactants, it is said to be a heterogeneous catalyst [9, 11]. The catalytic converter in automobiles is an example of this kind of catalyst. The catalyst is a solid and the reactants are in the gas phase. This configuration is also frequently encountered in industrial processes. Since the gas phase reactants only come in contact with the *surface* of the solid catalyst, the properties of this surface are very important. The active species, for example platinum or palladium, can be very expensive. This provides an additional reason to maximize the surface area of these materials. For this purpose, the active species are often dispersed as small particles on a support material. This makes it a so-called supported catalyst.

The support material is usually not catalytically active itself, although it may be in some cases, and it should be relatively stable at high temperatures under reaction conditions. In order to maximize the active surface area to volume ratio the support material is often highly porous. Frequently used support materials are Al_2O_3, SiO_2, active Carbon, zeolites, and sometimes also TiO_2 [10]. Since the reactants and products need to be transported to and from the active sites, different processes are important on different scales. This is illustrated in Figure 1.2. On a large scale, reactor beds are filled with the catalyst. The reactants have to diffuse and flow through the bed. An important parameter from an engineering point of view is for example the amount of pressure over such a bed that is needed to sustain a sufficient flow. On a smaller scale both the reactant and the product molecules need to diffuse through the pores of the catalyst particles. On this level the pore size distribution is an important parameter. Finally on the smallest scale, the reactant molecules adsorb on the active species and they react. After this reaction the product molecules can desorb and will try to find their way out of the catalyst bed.

Clearly, an investigation of a catalyst is an investigation of many simultaneous processes in a complex system. Needless to say that it may be very difficult to extract the desired information from such an investigation. For example, if one attempts to study the rates of adsorption or desorption of products and reactants at the surface of the active species one can easily end up in a situation where the

(a)   (b)   (c)
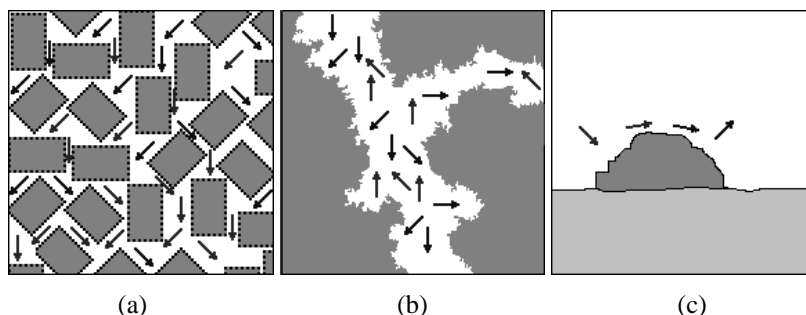
Figure 1.2: *Illustration of the different phenomena taking place in a catalyst bed at different length scales (Ref. [12]). (a) On a macroscopic scale both reactants and products flow through the catalyst bed. (b) On an intermediate scale the reactants and products diffuse through the pore structure of the catalyst, and (c) on a microscopic scale reactants adsorb and diffuse over the surface. They react and the products desorb.*

rate is limited by the transport properties instead of the adsorption and desorption at the active surface. The lack of information about processes on a local scale in such a catalyst seriously hinders research aimed at fundamentally understanding and systematically improving the fabrication of catalysts in a controlled way. At present, catalysts are still developed mostly by 'trial and error'.

In order to improve our understanding of the processes taking place in a catalyst on a microscopic scale, one is forced to first investigate these processes in a simplified system [13]. In such a model system, one can isolate and investigate specific phenomena without being overwhelmed by other processes taking place at the same time. The knowledge gained by these model investigations can then be combined to interpret experiments on more complex systems.

1.3 Model catalysts

In principle there are two possible strategies to model a supported catalyst. One can start with a real industrial catalyst and leave out certain components in order to simplify it, or one can start with the simplest model system and add features in order to make it more realistic. The simplest model catalyst is probably a single crystal surface of the active metal.

Soon after the formulation of catalysis by Berzelius it was realised that the surface of the catalyst plays a key role. Although the study of surfaces was initiated

in the 19th century, most of our present understanding is based on research of the last 25 years. The invention of the transistor has produced a strong additional driving force for the investigation of the properties of surfaces. Ultra-high vacuum (UHV) systems were developed in which surfaces can be kept clean for a sufficient period of time and an impressive collection of surface sensitive techniques was invented. In the last decades many clean single crystal surfaces have been studied. Fundamental studies of adsorption, desorption and surface reactions have revealed many intriguing phenomena. Adsorption of molecules on a single crystal surface for example leads in many cases to a reconstruction of the surface [14, 15]. Even a simple reaction, such as the oxidation of CO can lead to a very complicated process with oscillatory behaviour in which patterns are formed on the surface with regions covered mainly by oxygen and regions covered mainly by CO [16].

Studies of single crystals have contributed a great deal to the understanding of the processes that play a role on the microscopic scale in a catalyst. Nevertheless, their practical value is often limited. In modeling the surface of a catalyst by a single crystal surface many aspects have been neglected. The most obvious simplification is the complete absence of a support material. This implies that processes in which for example a reactant adsorbs on the support and diffuses to a supported metal particle where it reacts, as well as processes in which molecules adsorb on a metal particle and spill over to the support, are completely absent on the single crystal model surface. In practical catalysis however, these processes may be very important. Also the properties of the surface of a small metal particle are not always properly represented by the single crystal counterpart. On a small particle different kinds of facets are present, and the density of edge and corner sites is much higher than on a low index single crystal surface (see Fig. 1.1). Finally, the electronic structure of small particles differs from the electronic structure of large crystals [17]. The transition from metallic to insulating behaviour for very small clusters, may significantly influence the catalytic properties [18].

A more realistic model for a supported catalyst necessarily includes a support. Small particles supported on a *flat* support may be the ideal compromise between reality and simplicity. Such a system can be made in several ways. For the flat support one can think of a single crystal oxide surface. However, many oxides have a very poor electrical conductivity, which limits the range of experimental techniques that can be applied. Furthermore, the surfaces of these oxides are often much harder to prepare at a high quality than are metal single crystal surfaces [19].

Alternatives can be graphite, which is sufficiently conductive, or very thin films of oxide on top of a conducting substrate.

Unfortunately, the two most common support materials, Al_2O_3 and SiO_2 are very poorly conducting. Therefore thin films are the only option to study these materials with most of the surface science techniques. Indeed thin films of alumina and silica have been grown, and they have been used as a support material for small metal clusters [20, 21]. Nevertheless, growing high quality oxide films can be a complex problem in itself, and the properties of thin films may only partly resemble the properties of a bulk oxide, just like the properties of small particles can be different from bulk material. The most studied single crystal oxides are TiO_2 [19], MgO [22] and ZnO [23]. MgO and ZnO surfaces can be prepared relatively easily by cleavage, whereas TiO_2 has a relatively high electrical conductivity.

Depositing metal particles on these model supports can be achieved by several means. One can either first make small particles and deposit those particles on a substrate, or one can deposit an amount of material, and have the deposit aggregate into particles on the support. In cluster beams one can select clusters with a specific mass and 'soft land' these particles on a surface. Particles with a specific size may also be stabilized chemically and deposited from a colloidal solution. Vapour deposition of metals in UHV is a very well controlled way of depositing material. The material is deposited on the surface atom by atom, and particles form as a consequence of nucleation and growth from the deposited material. Wet chemical techniques show more resemblance to the preparation methods used for practical catalysts. Spin coating for example can mimic the process of pore volume impregnation [24]. Finally, modern lithography techniques can be applied to produce very well defined regular arrays of small particles. At present however, this is still limited to particles larger than several nanometers. Understanding the deposition and growth of metals on oxides is also of importance for the semiconductor industry. For metallic contacts on top of oxide films usually uniform smooth layers are required. The formation of particles from the deposited material is an unwanted effect in this case.

The particle size distribution forms one of the most important characteristics of the model catalyst. This distribution can be determined with the use of a suitable type of microscopy. With Scanning Tunneling Microscopy (STM) atomic resolution can be obtained, but it requires relatively flat surfaces for optimum performance. Therefore it is not very well suited for the study of real catalysts. The tech-

nique is available at many places and is compatible with UHV and other surface analysis techniques. This allows for *in-situ* experiments, i.e. sample preparation and characterization can all be performed in the same UHV set-up, without transferring the sample through air. Scanning Electron Microscopy (SEM) and Transmission Electron Microscopy (TEM) have been applied to both real and model catalysts [25, 26]. However, the resolution of SEM is usually not sufficient to observe the smallest particles of just a few tens of atoms, whereas the use of TEM requires difficult sample preparation techniques. Furthermore, both the small particles and the oxide support materials often are very sensitive to damage induced by the irradiating electron beam, and both kinds of electron microscopy are usually not available for *in-situ* experiments. In this thesis, I have used Scanning Tunneling Microscopy to investigate a model supported catalyst. This technique will be introduced in the following section.

1.4   Scanning Tunneling Microscopy

Scanning Tunneling Microscopy (STM) is a relatively new technique in the world of surface science. It was invented in the early eighties by Binnig and Rohrer at the IBM research facilities in Zürich [27–29]. Only a few years later they were awarded the Nobel Prize for this development. With this type of microscope it is possible to image surfaces with atomic resolution [30]. The basic operation of the STM is illustrated in Figure 1.3.

The microscope probes the surface with the tip of a very sharp needle. This needle is moved in the x, y and z directions with the aid of a piezo-electric actuator that shrinks, expands or bends, depending on the electrical potentials applied to its electrodes. With this actuator the tip can be moved over distances up to a few micrometers with an accuracy down to one percent of an Ångström. When a potential difference is applied between tip and sample, an electrical current will flow when the tip and the sample are very close to each other. At a few atomic spacings distance between sample and tip their electronic wavefunctions will start to overlap and electrons tunnel through the vacuum barrier. The overlap depends more or less exponentially on the distance, and so does the tunneling current. Therefore the tunneling current is an extremely sensitive measure of the distance between tip and surface. Usually the STM is operated in *constant current* mode. When the tip is scanned in x and y directions, a feedback circuit regulates the z position in order
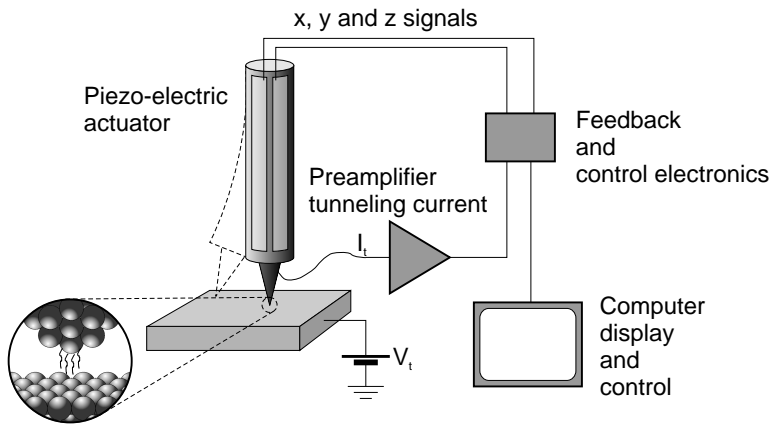
Figure 1.3: *Schematic illustration of the Scanning Tunneling Microscope. When a bias voltage V_t is applied to the sample, a tunneling current I_t will flow that depends very strongly on the distance between tip and sample. In order to keep the tunneling current constant, a feedback circuit continually adjusts the height of the tip as it is scanned over the surface. In this way a topographic map of the surface is obtained.*

to keep the current constant. By recording the z coordinate as a function of x and y a topographic map of the surface is obtained.

Since the tunneling current measures the overlap between wavefunctions one does not measure pure topography. Instead electronic and topographic information is mixed in the images. In simple metals this is usually not so important, but on oxides one needs to be careful when interpreting images on an atomic scale. The resolution of the STM originates from the strong dependence of the tunneling current on the distance between tip and sample. Although the overall radius of the tip may be relatively large, the local protrusion that happens to be closest to the surface will completely dominate the tunneling current. Therefore STM images of flat surfaces can show a superb resolution. However, when the surface is not flat, the macroscopic size of the tip becomes important, which broadens the high features in an image. This is usually called 'tip convolution'. For supported nanoparticles this effect seriously limits the measurement of the particle size distribution.

The Scanning Tunneling Microscope is a relatively slow instrument. Instead of making a snapshot, an image is built up line by line. The time needed to scan one image typically ranges from just below one second to several minutes. On this

time scale surfaces are often in motion [31]. This results in a frizzy appearance of the moving features in the images. Very rapidly moving objects, like single atoms, will be simply invisible.

One of the great virtues of STM for the study of a model catalyst is that it can in principle be operated in gaseous atmospheres, whereas most of the surface science analysis techniques and sample preparation methods require a vacuum. Therefore STM may be the tool to bridge the so-called 'pressure gap' between surface science studies at very low pressures, like described in this thesis, and practical catalysis at high pressures [32, 33]. Finally, the recent development of Non-Contact Atomic Force Microscopy (AFM) [34], has opened the way to atomically resolved studies of truly non-conducting support materials.

1.5   This thesis

In this thesis I present investigations of very small palladium 'nanoparticles', supported on a TiO_2 (110) substrate. As is outlined above, the choice for TiO_2 can be considered as a compromise between practical relevance and experimental feasibility. Its relatively high electrical conductivity allows for the use of Scanning Tunneling Microscopy and with this technique the surface can be observed in great detail. The high electrical conductivity of TiO_2 originates from minor deviations from the perfect stoichiometry. In Chapters 3 and 4, I show that non-stoichiometry can have very large consequences for the surface morphology. Furthermore, a reaction of the crystal surface with gaseous oxygen leads to a considerable increase in surface roughness. Clearly the TiO_2 (110) surface is not as stable and inert as support materials are often thought to be. Before discussing the TiO_2 surface in detail in Chapters 3 and 4, I first describe the experimental equipment in Chapter 2. In this chapter I also discuss the software that we developed to analyze STM images of a substrate covered with nanoparticles.

In Chapters 5 and 6 the growth of very small palladium particles is investigated. Very small particles of just a few tens of atoms could easily be created by vacuum deposition of palladium metal. At elevated temperatures these particles grow. This also happens in real catalysts. As a consequence the total surface area of the active species decreases, which makes this a highly undesirable phenomenon. By using the software presented in Chapter 2, the particle growth could be studied quantitatively and it could be compared with different growth models. We find that

very small particles are highly mobile and coalesce when they 'collide'. The rate of this process turns out to be influenced very strongly by the (non-)stoichiometry of the oxide substrate. This also has a marked influence on the particle shape. Finally, in Chapter 7, I discuss the effect of a hydrogen atmosphere on a Pd/TiO_2 model catalyst. Surprisingly, the small palladium particles seem unaffected by the presence of the hydrogen atmosphere, but the TiO_2 substrate changes noticeably.

Chapter 1. Introduction

II

Experimental set-up and data analysis

2.1 Introduction

The experiments which are described in this thesis were performed mainly in one experimental set-up. This ultra-high vacuum (UHV) chamber, called NACRA, which stands for Nano Crystal Analysis, is described in this chapter. First a general description of the set-up is given, after which several specific items are treated in more detail.

Most of the measurements were performed with a Scanning Tunneling Microscope. The images produced by this type of microscope can contain a very large amount of information. In order to extract the relevant quantitative information from the measured images, several special filtering techniques and other automatic procedures were used. These are described at the end of this chapter.

2.2 The UHV set-up: NACRA

2.2.1 General description

The use of ultra-high vacuum (UHV) has some great advantages for the investigation of model supported catalysts. First of all it allows for a very well-defined preparation of the studied samples and it provides a means to keep the surface clean for a prolonged period of time. UHV is also required for many of the standard surface science techniques. The NACRA set-up is shown in Figures 2.1 and 2.2.

The set-up consists of three parts, which are separated by valves: the main experimental chamber, a deposition chamber with an e-beam evaporation source and a sample/microscope loading chamber. Evaporation material can be added or changed without breaking the vacuum of the main chamber. Also new substrates can be introduced and tips in the microscope can be changed while the vacuum in
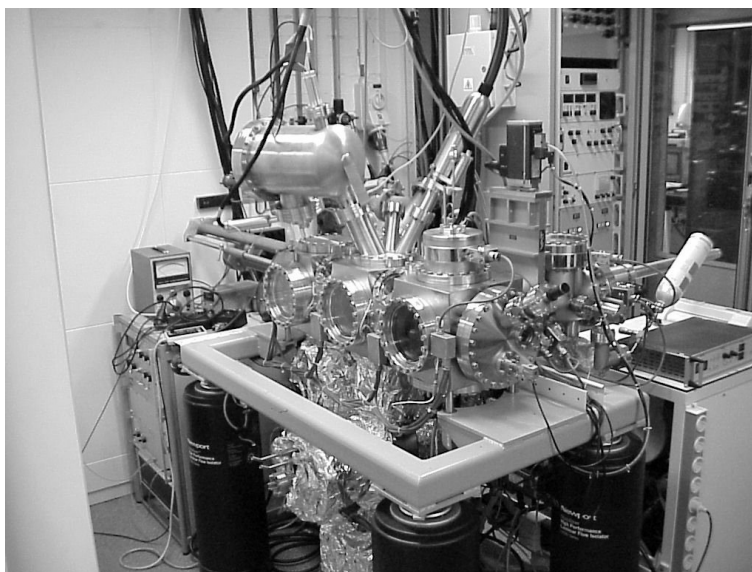
Figure 2.1: *Picture of the set-up.*

the main chamber is maintained. The system is pumped by two 50 l/s turbo molecular pumps, a 2000 l/s titanium sublimation pump and a 200 l/s getter ion pump. The two turbo molecular pumps are backed by one rotary vane pump via a buffer vessel. The complete system can be baked at a temperature of 150°C. This results in a base pressure of 1×10^{-10} mbar in the main chamber and loading chamber. When the deposition chamber is shut off from the main chamber by closing the valves, it is only pumped by one of the turbo molecular pumps, resulting in a base pressure of 1×10^{-9} mbar in that chamber. When all valves are open an overall working pressure of 2×10^{-10} mbar is obtained in all the chambers.

The substrate, as well as the 'scanner' of the microscope can be transferred from the loading chamber into the main experimental chamber. This main chamber is equipped with a high-temperature Scanning Tunneling Microscope (STM), retarding field optics (VG Microtech) for Low Energy Electron Diffraction (LEED) and Auger Electron Spectroscopy (AES), an X-ray source (VG XR3E2) combined with a hemispherical analyzer (VG CLAM 2) for X-ray Photo-electron Spectroscopy (XPS), and a Quartz Crystal Microbalance (Leybold Inficon) for monitoring the deposition process.
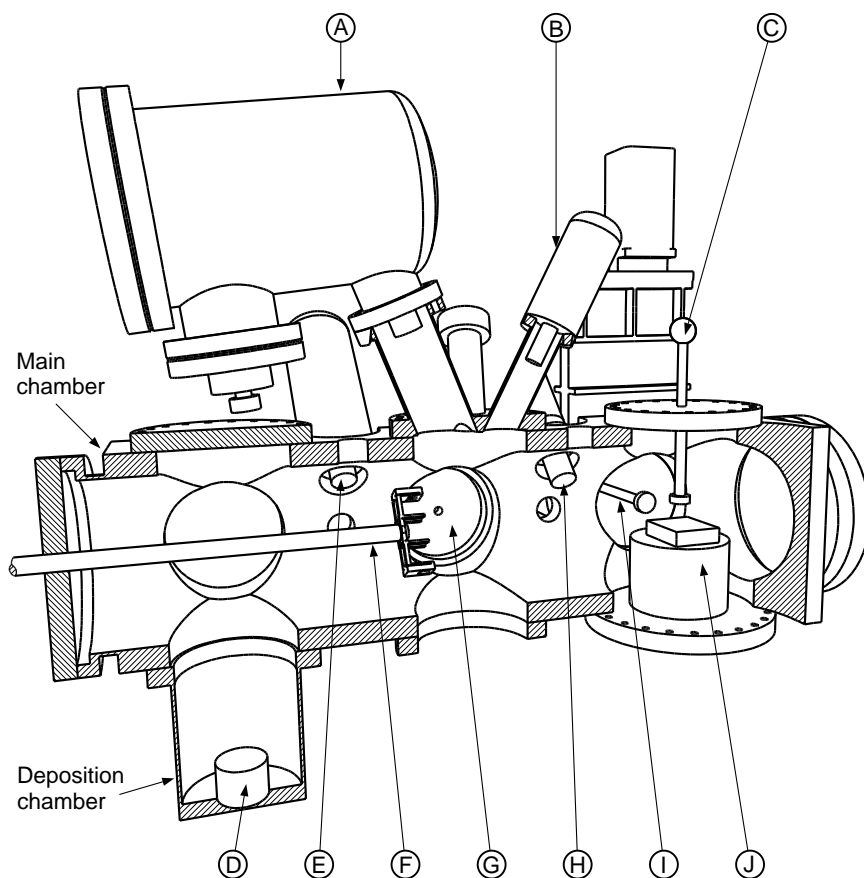
Figure 2.2: *Schematic view of the set-up.* **(A)** *Hemispherical analyzer for XPS,* **(B)** *X-ray source for XPS,* **(C)** *Wobble stick,* **(D)** *Evaporation source,* **(E)** *Quadrupole Mass Spectrometer,* **(F)** *Sample manipulator,* **(G)** *Retarding Field Analyzer for LEED and AES,* **(H)** *Sputter gun,* **(I)** *Transfer to loading chamber,* **(J)** *Scanning Tunneling Microscope. In this schematic representation the valve between the deposition chamber and the main chamber is not shown. The loading chamber is hidden behind the main chamber.*

The high-temperature STM was developed by Kuipers *et al.* and is described elsewhere [35]. The design of this microscope has been optimized with finite element analysis in order to reduce thermal drift in the z-direction. This prevents tip crashes upon temperature changes. The drift in the lateral x and y directions has not been optimized. The lateral movement during temperature changes can well be larger than the piezo range, but once the temperature has stabilized the drift is very low (0.01 Å/s) [35]. Measurements can be performed with this microscope between room temperature and $\approx 750\,$K. However, most of the measurements described in this thesis were performed at room temperature. The STM is equipped with a high rate data acquisition system. The maximum pixel frequency is 100 kHz, which is equivalent to 10 (small) images per second of 100×100 pixels. On surfaces with larger height differences than one or two atomic layers, such as the surfaces studied in Chapters 5 and 6, the maximum scanning speed was usually limited by the feedback control of the microscope, instead of the maximum data acquisition rate. In these cases we used the high available sampling rate for oversampling and thus improving image quality.

The XPS system was added only during the final stages of the project and was therefore not available during most of the experiments. A low-energy ion source was used for sputter cleaning of the samples. Gases can be introduced from a reservoir into the main chamber via a leak valve. The reservoir can be filled from 4 different gas bottles and it can be pumped by one of the turbo molecular pumps. A Quadrupole Mass Spectrometer is available to determine the gas composition. The residual gas consisted mainly of hydrogen.

In order to reduce the level of mechanical vibrations, the complete set-up rests on four air-damped legs and the main chamber has been machined out of one massive block of stainless steel. This results in a very stiff chamber with a high mass. The turbo molecular pumps are connected to the chamber via bellows to reduce transmission of their vibrations into the chamber.

Samples are mounted in a molybdenum holder which fits in the STM as well as in a translation/rotation stage. This stage is used to move the sample through the main chamber and to position it in front of the other surface analysis techniques and the evaporation source. By use of a wobble stick the sample can be transferred between the microscope and the translation/rotation stage. At both positions the sample holder can be heated with a filament by heat radiation or electron bombardment to the rear side of this holder. A piece of tantalum was mounted in the

sample holder, behind the crystal, in order to prevent non-uniform heating, which can otherwise easily result in cracks in the oxide crystals. Tantalum has a much higher thermal conductivity than TiO_2. Since the design of the sample holder and the necessary transfer between the STM and the translation/rotation stage did not allow for permanent electrical connections to the sample holder, it was not possible to use a thermocouple or other temperature sensor in our experiment. Therefore the sample temperature was calibrated separately as a function of the heating power. For this calibration both an infrared pyrometer and a thermocouple, spotwelded to a stainless steel 'dummy' sample, were used. The emissivity of this stainless steel sample was estimated to be 0.5. The absolute accuracy of the temperature measurement is estimated to be $\sim 30\,\mathrm{K}$ (at $700\,\mathrm{K}$).

2.2.2 Sample characterization

The substrates were prepared by a combination of ion sputtering and heating. Sputtering was typically performed with $600\,\mathrm{eV}$ Ar^+ ions, with a beam intensity of $\approx 1\,\mu\mathrm{A/cm}^2$. Annealing was usually performed in 10 minute periods to temperatures between $800\,\mathrm{K}$ and $1200\,\mathrm{K}$, requiring heating powers of $30\,\mathrm{W}$ to $80\,\mathrm{W}$. Furthermore palladium could be deposited and the sample could be exposed to gases. The deposition process will be explained in more detail below.

After preparation, the sample can be characterized with several techniques. The majority of the measurements was performed with the Scanning Tunneling Microscope and the results of these measurements will be presented in the following chapters. Both XPS and AES provide information about the composition of the surface. These techniques were mainly used to determine the level of contamination of the sample and to check the amount of deposited material. Examples of an AES and a XPS spectrum obtained on TiO_2 are shown in Figure 2.3.

For AES an electron beam with a beam energy of typically $2.5\,\mathrm{keV}$ and a current on the sample of $2\,\mu\mathrm{A}$ were used. The spot size is estimated to be $1\,\mathrm{mm}^2$ and the retarding field of the analyzer was modulated with $1-5\,\mathrm{V}$ at $\nu = 1819\,\mathrm{Hz}$. The signal was detected with a lock-in amplifier at 2ν, which results in a differentiated spectrum.

AES was also used to check the electrical conductivity of the sample. If the sample is so poorly conducting that it charges under the influence of an electron beam, the Auger peaks shift in energy, since the electrons leaving the surface are repelled by the negatively charged surface. The elastic peak however does not shift,
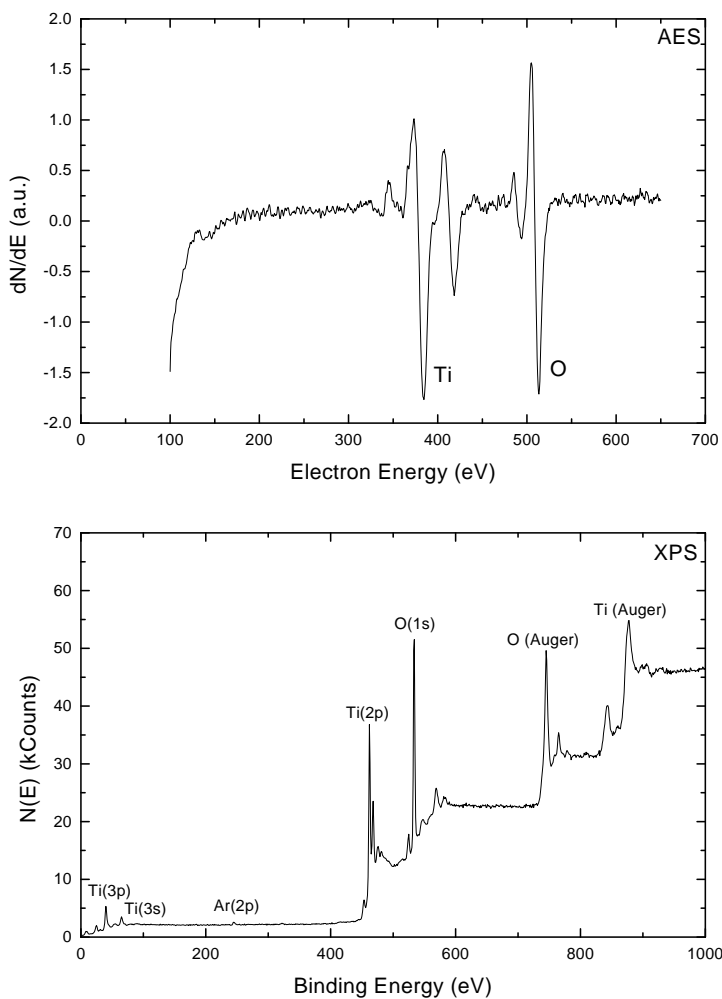
Figure 2.3: *Examples of both an AES and an XPS spectrum obtained on TiO$_2$. The incident electron beam in the AES experiment had an energy of 2.5 keV and the retarding field was modulated with 5 V. For XPS, Mg Kα X-ray radiation with an energy of 1253.6 eV was used. The analyzer pass energy was set to 100 eV.*

28

since the elastically reflected electrons lose the same amount of energy when they approach the sample. Therefore, a shift of the Auger peaks with respect to the elastic peak serves as a straightforward indicator of surface charging.

LEED provides information about the crystallographic order at the surface. A 'good quality' substrate is usually characterized by sharp diffraction spots and a low background intensity. Unfortunately, electron stimulated surface modification effects can play an important role on TiO_2 [36, 37]. For example, one can see the LEED pattern degrade within minutes under the influence of the irradiating electron beam (electron energy 50 eV to 100 eV, target current $\leq 1\,\mu A$ and spot size $\approx 1\,mm^2$). Therefore LEED and AES were not used between the last preparation cycle and the STM measurements.

2.2.3 Metal deposition

Material can be deposited on the sample by placing it above the e-beam evaporator in the deposition chamber. In the evaporator an electron beam is used to heat and evaporate the material which is to be deposited, palladium in this case. The evaporated material condenses on the sample. The crucible of the evaporator is cooled with water. The distance between evaporator and the sample is approximately 50 cm, which is quite large. This minimizes the heat load on the sample and thus prevents a rise in sample temperature during deposition. A typical deposition rate used in the work presented in Chapters 5–7 is 4×10^{11} atoms/s·cm^2. This requires approximately 150 W, which is only a fraction of the maximum power of 2 kW. Since the 1 cm^2 sample covers only 3×10^{-5} sr viewed from the source, the power on the sample due to the thermal radiation of the source is indeed completely negligible. In order to avoid material deposition on the chamber walls, two shields are positioned between the source and the sample. When the valve separating the evaporator from the main chamber is closed, the evaporator can easily be degassed without contaminating the vacuum in the main chamber. During deposition the valve is obviously open and the pressure in the main chamber can temporarily go up to 2×10^{-8} mbar.

The amount of deposited material is measured with a quartz crystal oscillator, positioned just a few cm away from the sample. When material is deposited on this quartz crystal, its resonance frequency changes. Since the frequency can be measured very accurately, small, submonolayer amounts of deposited material can be detected, with a resolution of 0.12 nanogram/cm^2. Because the quartz
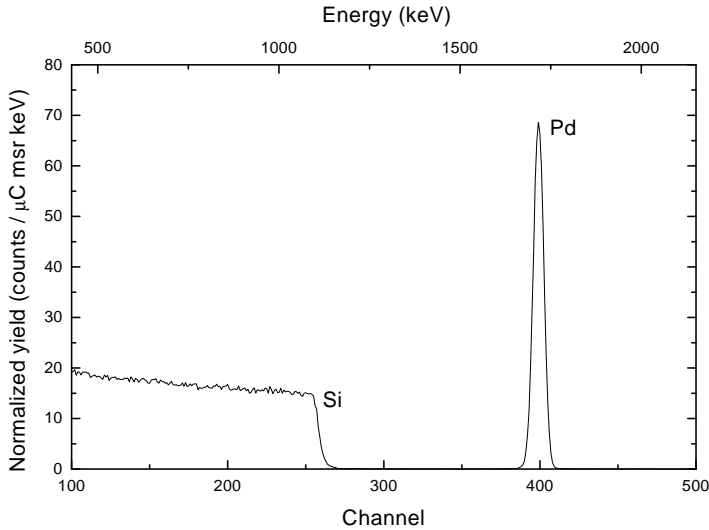
Figure 2.4: *RBS measurement of a ~20nm thick palladium layer deposited on the native oxide on a silicon wafer. The absolute coverage of palladium was determined to be $(138 \pm 1) \times 10^{15}$ atoms/cm^2. We used 2.0 MeV ^{4}He$^+$ ions at an angle of incidence of 3°. Detection was performed at a scattering angle of 165°.*

oscillator measures the deposition flux at a position different from the sample position, we decided to calibrate the real flux on the sample *ex-situ* with Rutherford Backscattering Spectrometry (RBS). For this purpose a thick layer of palladium was deposited on a piece of a silicon wafer, while the deposition was monitored with the quartz crystal. After deposition, the sample was removed from the vacuum chamber and RBS measurements were performed. An example of such an RBS measurement is shown in Figure 2.4. Since Pd is much heavier than silicon, the Pd signal is nicely separated from the Si signal. By integrating the Pd peak and accounting for the scattering angle, the dose of incoming ions, and the known scattering and stopping cross-sections for He with Si and with Pd, one can obtain an absolute measure of the coverage with an accuracy better than 1 %. The coverages obtained from the RBS measurements were approximately 20 % lower than the direct reading of the quartz crystal and were used to calibrate the quartz crystal.

2.3   Image processing

STM images can contain an enormous amount of information. In order to extract the relevant parts of this data we used several image processing techniques. The main goal in this project has been to determine the properties of metal clusters on an oxide surface. In order to quantify the information stored in an STM image, we developed an algorithm which automatically determines the size and position of clusters in such an image. The algorithm consists roughly of three stages: *pre-processing, segmentation,* and *data extraction*. The goal of the preprocessing step is background subtraction and in some images noise suppression. For this purpose several non-linear filters were implemented. These are well-known filters, and only a brief description of their operation will be given in the following subsections. In the segmentation step the objects of interest are identified, and in the final step the desired properties, i.e. position and size, of these objects are measured. We stress that without these automated methods it would have been close to impossible to obtain the detailed quantitative statistical information that we present in Chapters 5 and 6.

2.3.1 Erosion and Dilation

Since STM images are built up of pixels one can think of an image as a two-dimensional matrix with values (the heights). Many filters compute a new value for a pixel, using its old value and the values of the surrounding pixels. For example by averaging over these pixels one obtains a simple smoothing filter. The erosion and dilation filters work similarly. Instead of calculating the average of a group of pixels they determine the minimum (erosion) or maximum (dilation) value [38,39]. The erosion filter causes hills to shrink and valleys to grow, whereas the dilation filter does the opposite. Repetitive use of the erosion (or dilation) filter is equivalent to an erosion (or dilation) with a larger 'mask'. For example, if we apply the erosion (dilation) procedure twice with a mask of 3×3 pixels, the result is equivalent to applying it only once with a mask of 5×5 pixels. This can result in square like structures after many subsequent calls to this filter. The imaging of a surface by an STM in itself resembles a *dilation*-like process, although one usually speaks about tip-*convolution*. Therefore these filters are also used in image restoration techniques [40,41].
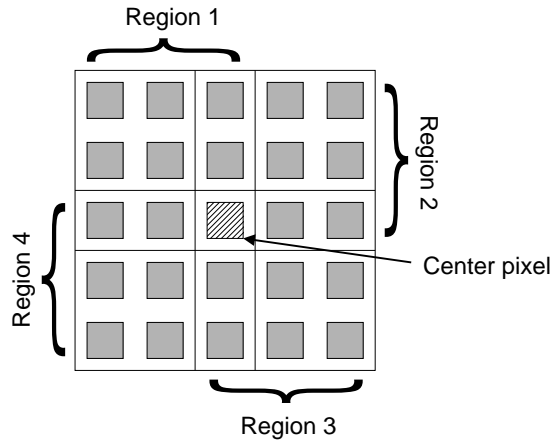
Figure 2.5: *Illustration of the Kuwahara filter. In order to obtain a new value for the center pixel, four 3×3 pixel regions are defined within the 5×5 pixel neighbourhood. In each of these regions the average value μ_i is calculated, as well as the standard deviation. The average value of the 3×3 region with the lowest standard deviation is selected as the new value of the center pixel.*

2.3.2 Kuwahara filter

Averaging over the values of a group of neighbouring pixels is a very simple efficient way of suppressing noise in images. However, in processing STM images it has a major drawback. Very often flat terraces are imaged, that are separated by steps. The optimum result of a noise filter would be to suppress the noise on the terraces to make them flat, but also to keep the steps as sharp as possible. A conventional smoothing (i.e. low pass) filter smears out the steps. This can be circumvented by using the Kuwahara filter, which is an *edge preserving filter* [39]. As an input to calculate a new pixel value it uses a 5×5 pixel environment. In this group of 5×5 pixels 4 groups of 3×3 pixels are defined as indicated in Figure 2.5. In each of these 4 groups the average value and the standard deviation are calculated. As the new value of the center pixel the Kuwahara filter chooses the average value of the group with the lowest standard deviation. This means that the new value corresponds to the height of the nearest flat part. Therefore it produces the desired result: the terraces are smoothed, whereas the steps are even sharpened.

The results of the Kuwahara filter and the erosion and dilation filters are
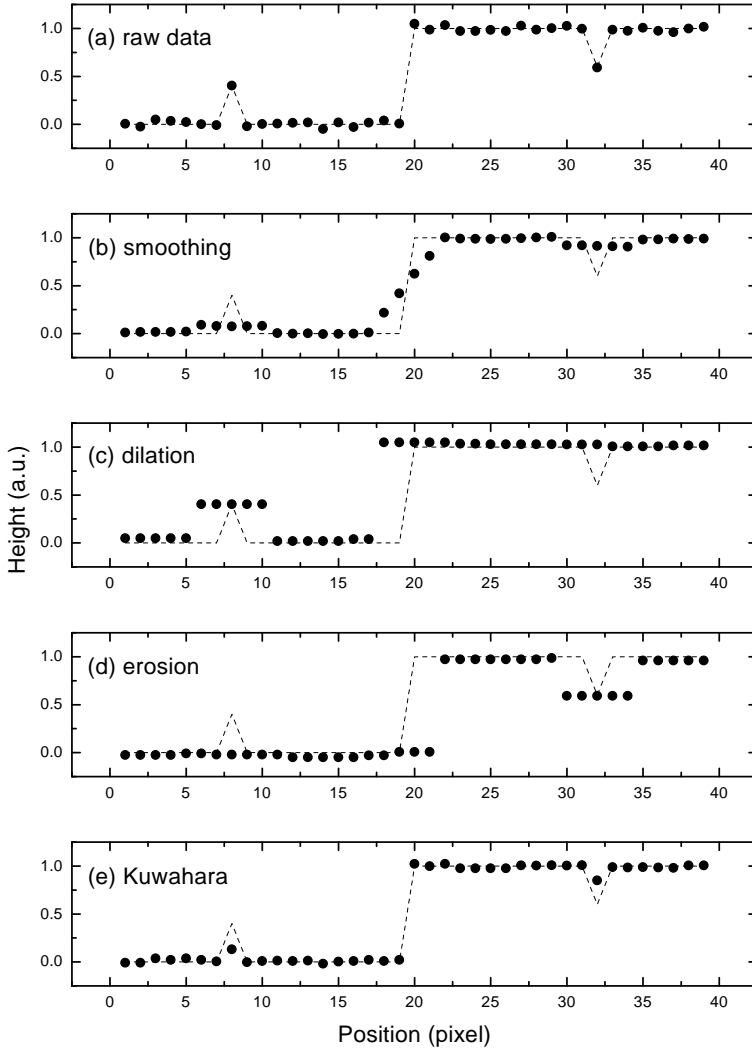
Figure 2.6: *Illustration of the effect of several filters on one-dimensional data. (a) The raw data, (b) ordinary smoothing: 5-point averaging, (c) 5-point dilation, (d) 5-point erosion, (e) 5-point Kuwahara filter with two 3-point regions.*
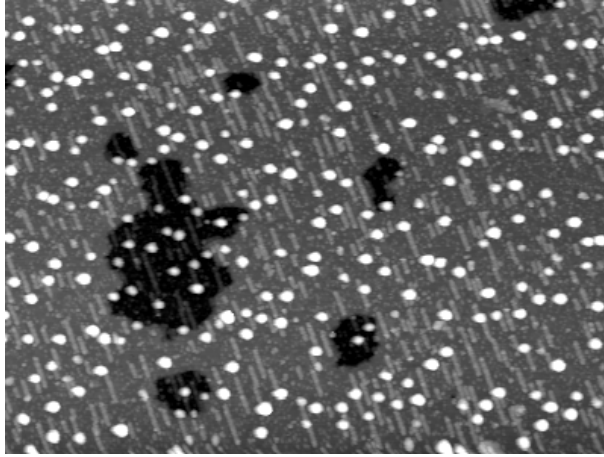
Figure 2.7: *Example of a STM-image of the TiO_2 surface covered with Pd clusters. One can see two different layers of the TiO_2 crystal, separated by steps. The one-dimensional shapes are added-row structures formed by the substrate (see Chapter 3) and the bright round objects are the clusters. The objective of the cluster detection algorithm is to automatically obtain the positions and sizes of all clusters in the image.*

illustrated in Figure 2.6 for a one-dimensional data set, and compared with an ordinary smoothing filter.

2.3.3 Particle detection

Our aim is to automatically determine the position and the height of the particles in an image. An example of such an image is shown in Figure 2.7. Several techniques can be used to identify the particles in an image. We used a very simple selection criterion, namely the height. Every pixel that sticks out above a certain reference height is interpreted as (part of) a particle. This is not a sufficient recipe since two pixels fulfilling this criterion can belong either to two separate particles or to the same particle. Therefore an additional criterion is used. If two neighbouring pixels both fulfill the first criterion (they are higher than the reference height), then they belong to the same particle. In this way groups of pixels are formed and segmentation is completed. For each group of pixels the average x and y coordinates and the maximum height are determined. These numbers are given as the output of the algorithm as position and size of the corresponding particle.

However, applying the height criterion directly to select the particles in an image leads to many errors if the substrate shows height variations comparable to the particle heights. Also for a determination of the heights of the individual nanoparticles the local level of the substrate needs to be known. In particular, steps on the surface can cause problems. By subtracting an image of the substrate without particles from the original image, both these problems are solved. One can obtain an image of the substrate without particles by applying a suitable combination of the filters described previously. This is illustrated in Figure 2.8.

The particles can very efficiently be removed by sequential use of the erosion filter. This shrinks the particles, but hardly changes the flat terraces (Fig. 2.8a). However, also the steps move due to this filter. The higher terrace is 'eaten away'. Once the particles have disappeared, an image is obtained with only the terraces and steps of the substrate, but the steps are no longer at their original position (Fig. 2.8b). Although dilation is *not* the inverse of erosion it can be used to move the steps in the opposite direction. If the dilation filter is applied the same number of times as the erosion filter was used, the steps will return approximately to their original positions. Finally, the noise in this reference image can be reduced by using the Kuwahara filter (Fig. 2.8c). If the resulting image (Fig. 2.8c) is subtracted from the original image (Fig. 2.7), the result (Fig. 2.8d) can easily be processed by the particle detection algorithm. This completes the preprocessing procedure. If the particles in the image are very large (i.e. many pixels per particle), the erosion filter has to be applied very many times before the particles disappear. This makes it more difficult to restore the original substrate. When there are just a few pixels per nanoparticle, the height of the particle may be difficult to determine. Finally, terraces that are very narrow, e.g. with a width comparable to the cluster size, can disappear due to the filtering. They will not be subtracted from the original image and therefore the final, subtracted image can contain some small spurious 'islands' due to these parts of the substrate. If remnants of the substrate structure would be falsely identified as particles by the segmentation routine, such errors need to be corrected 'by hand'.

After subtraction of the substrate features from the image, the nanoparticles are found by thresholding, as was described above. This is illustrated in Figure 2.9. Thresholding results in a binary image with all pixels above the reference height 'on', and all pixels below the reference height 'off' (Fig. 2.9b). In order to help the user find a proper setting of the reference height, this binary image is overlayed on

(a)

(b)

(c)

(d)
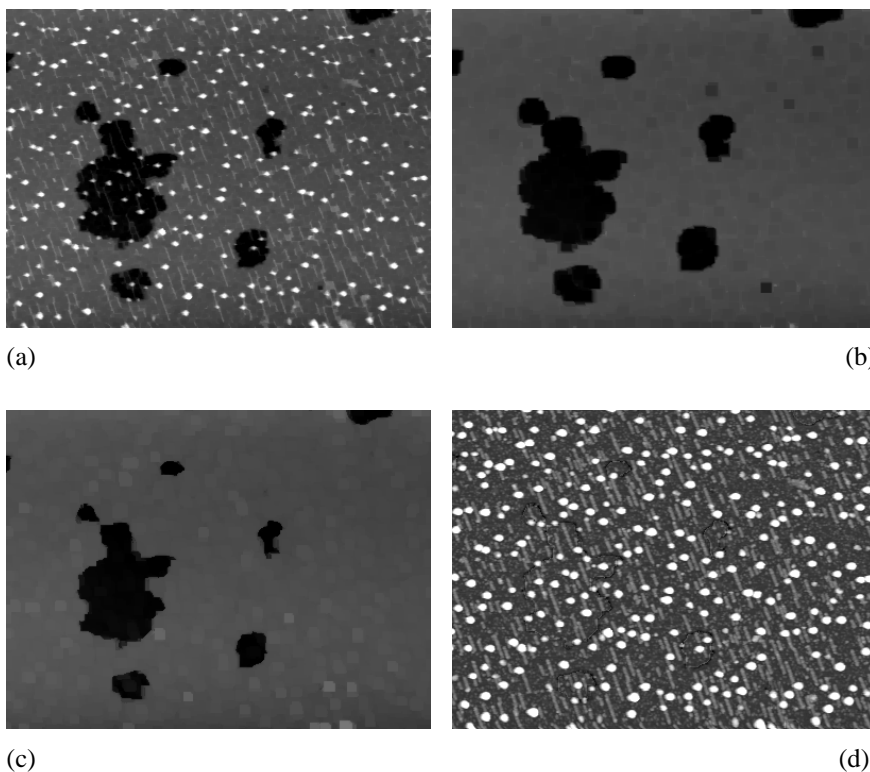
Figure 2.8: *In these images the filtering process is illustrated. The original image is shown in Figure 2.7. The final result of the filtering is an image of the bare substrate, without the Pd particles. (a) The result of one erosion step. The particles are smaller and the lower terraces have increased in size. (b) After a total of 4 erosion steps the particles have disappeared. The lower terraces are significantly larger than in the original image. (c) After a total of 4 dilation steps and a filtering step with the Kuwahara filter, an image is obtained that is very close to the original substrate without particles. Due to the dilation filter, the steps have returned approximately to their original positions. (d) Subtraction of the filtered image from the original results in an image in which all Pd particles (and added rows) reside on a completely flat, featureless substrate. This image can easily be processed by the particle detection algorithm.*

(a)
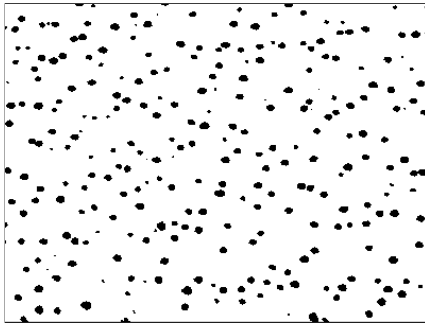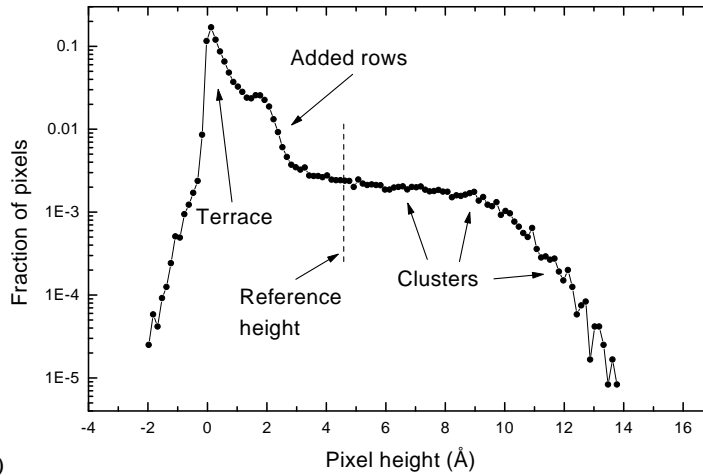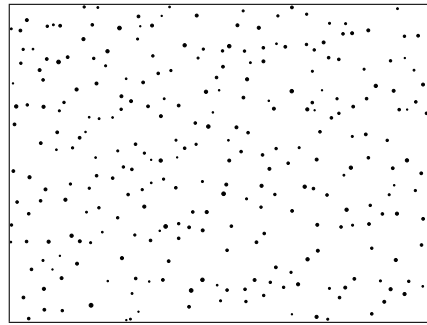
(b)   (c)

Figure 2.9: *Illustration of the particle detection algorithm. (a) The height distribution of the pixels in Fig. 2.8d. Note the logarithmic vertical scale. Contributions of the terraces and the added rows can be distinguished easily. The Pd particles give rise to a very broad height distribution, since also the edges of the particles contribute to the distribution. (b) By thresholding the image shown in Fig. 2.8d with a reference height set by the user, a binary image is obtained. All pixels higher than the reference height are shown black, all pixels lower than the reference height are shown white. (c) From each connected group of pixels in (b) the average position and the maximum height are determined. The result of this is illustrated here. The size of the dots is proportional to the determined height of the corresponding cluster. In total 279 clusters with an average height of 9.3 Å were detected in this image.*
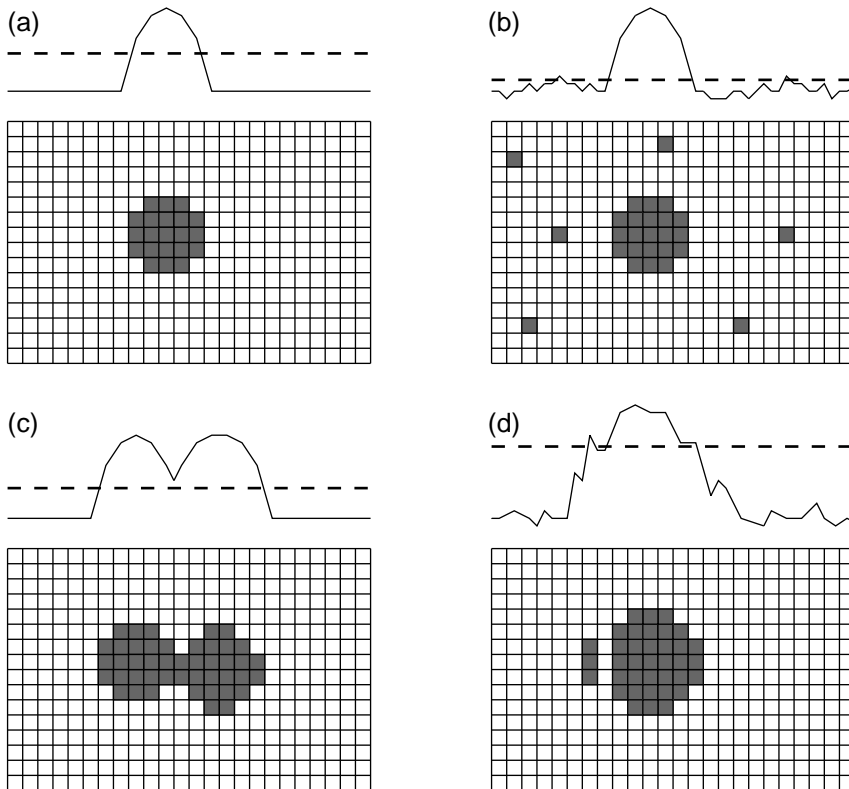
Figure 2.10: *Illustration of the cluster detection algorithm and several potential sources of error. (a) shows the algorithm as it should work. All pixels higher than the reference value are identified and one group of pixels corresponds to one particle. (b) The reference height is set so low that at some places the noise on the terrace exceeds the reference height. These fluctuations are wrongly identified as particles. (c) If two particles are very close together, the output of the algorithm might be only a single particle. (d) A high noise level can cause some parts of one particle to drop below the reference height and therefore two particles can be 'recognized' where there is only one. Finally a particle is not detected if the detection level is set above the maximum height of the cluster (not shown). If high-quality images are used the errors of the detection algorithm are usually smaller than the statistical variations.*

the computer screen in another color on the image to be processed. In this way it is usually easy to find the optimal choice for the reference height. Once this level has been set, the average position and maximum height of each connected group of pixels in the binary image is determined.

The combination of background subtraction and thresholding works very well (Figs. 2.7–2.9), but it is not perfect. There are several sources of error, illustrated schematically in Figure 2.10. First of all it is difficult to detect very small particles. If the reference height is set too high, small nanoparticles will be overlooked. If the reference height is set too low, height variations in the substrate can be wrongly identified as particles. Also a pair of nearby particles can be recognized as only one single particle. The latter problem depends strongly on the degree of tip convolution, which broadens the apparent lateral dimensions of each particle. Finally, if there is much noise in the image and the reference height is set high, the particle detection algorithm may sometimes identify two or more particles where there is only one. Of course, noise can also cause errors in the determination of the heights of the particles. When high-quality images are used, i.e. with a sharp tip and a low noise level, the detection errors are usually insignificant with respect to statistical variations. As an example, the analysis shown in Figures 2.7–2.9 resulted in a total of 279 nanoparticles. By a careful visual inspection of these figures we found only three errors of the kind shown in Fig. 2.10c, which is only 1% of the total number of particles in the image.

III

The TiO$_2$ (110) surface

In this chapter we describe the titania surface. Using Scanning Tunneling Microscopy we investigated the surface morphology and its dependence on preparation procedures. Low temperature annealing does not completely restore the damage created by sputtering, whereas high temperature annealing results in the loss of oxygen from the crystal. At elevated temperatures in UHV TiO$_2$ is reduced. This results in a color change and an increase in electrical conductivity. At the surface, the reduction results both in isolated atomic size defects which are attributed to oxygen vacancies, and in line defects. After reoxidation of the crystal the surface is rough. This can be explained by the nucleation and growth of new layers of oxide.

3.1 Introduction

During the last decades the surfaces of metals and semi-conductors have been studied extensively and many phenomena on those surfaces are understood in great detail. For a long time research focused on metals and semi-conductors because of their important technological applications in catalysis and microelectronics. The understanding of the surfaces of oxides, however, is more limited. For a large part this is because they have received much less attention, but also because of their complexity [19, 42]. Furthermore, the study of oxides involves several practical experimental problems. First of all, most oxides are electrically insulating or very poorly conductive. Since many surface science techniques use an electric current to probe or prepare the surface this can be a serious problem. A second practical problem concerns the surface composition. The sample preparation steps can leave the surface and near-surface region with a stoichiometry different from that of the bulk oxide. In principle this is a problem, although it can sometimes also lead to

advantageous modifications of the surface properties (see below).

In spite of the relatively modest number of investigations of oxide surfaces, oxides do have many important applications. Therefore oxide surfaces are now rapidly gaining interest. With the decreasing feature size in integrated circuits, the properties of the insulating oxide used, become more and more important. Also in catalysis oxides play an important role. They are used to support and disperse small catalytically active metal particles, but they can also act as the catalyst themselves. [9, 43, 44]. Titanium dioxide is an efficient catalyst for the photo-dissociation of water for example [45].

One of the most studied oxide surfaces is the TiO$_2$ (110) surface. TiO$_2$ can have a relatively high electrical conductivity (see below), which makes it relatively easy to use standard techniques. Although this surface exhibits very complex behaviour, as will be explained in the remainder of this chapter, TiO$_2$ (110) is considered to be one of the most easily prepared and stable oxide surfaces [19]. Therefore it has become the model oxide surface, and it has been studied with several techniques, Scanning Tunneling Microscopy being one of the most prominent [19, 46–57].

3.2 Properties of the TiO$_2$ (110) surface

Titanium dioxide exists in three different crystallographic structures: rutile, anatase and brookite. Rutile is the most common and most stable structure of the three. Also in this study rutile crystals were used. The rutile structure is shown in Figure 3.1.

Besides the different crystal structures of TiO$_2$, titanium oxide does also exist in several compositions. The fully oxidized state discussed above, TiO$_2$, is the most stable, but it can be reduced relatively easily. A stable bulk phase with Ti$_2$O$_3$ exists with a corundum structure, but also phases with intermediate compositions can be formed by introducing so called 'crystallographic shear planes' into the rutile structure. A crystallographic shear plane is an extended planar defect structure that arises from a shear in the crystal structure, in such a way that a complete plane of oxygen vacancies is eliminated [19]. Finally also a TiO structure can be formed, but this is much less stable than the Ti$_2$O$_3$ structure [19].

The fully oxidized compound, TiO$_2$ has a bandgap of $\approx 3\,\text{eV}$ and therefore it is not a very good conductor at room temperature. However, as soon as the ox-

Figure 3.1: *Schematic representation of the rutile crystal structure of TiO$_2$. The dark and light spheres correspond to titanium and oxygen atoms, respectively (a= 4.594 Å, c= 2.958 Å).*

ide is reduced mildly, so that oxygen vacancies are present, donor states appear in the band gap region and the electrical conductivity increases dramatically [19, 58]. Also the optical properties depend very strongly on the density of oxygen vacancies. A fully oxidized crystal is transparent, but with increasing oxygen vacancy concentration it becomes yellow, light blue, dark blue and finally completely black. Although these changes are dramatic and clearly visible with the naked eye, the change in composition associated with them is very small. The Ti:O ratio changes by far less than 1% under the conditions described in this chapter [59, 60]. Oxygen vacancies can be introduced into a titanium dioxide crystal by several means. The easiest process is simple heating in a UHV environment, or any other environment with a low oxygen pressure [59]. Irradiation with an electron beam causes electron stimulated desorption (ESD) of oxygen [36, 37]. Finally the composition of the crystal might be changed by preferential sputtering when sputter cleaning is used in the sample preparation. Whereas the effects of ESD and sputtering are mainly limited to the surface region, annealing also effects the bulk of the crystal, as is evident from the changes in color. Since 'normal' sample preparation procedures in UHV involve both sputtering and annealing they usually result in a reduced sample. By annealing the sample in an oxygen atmosphere the extend of reduction may be limited, but this also affects the surface morphology (see below).

Figure 3.2 shows a ball model of the expected bulk termination of the (110)
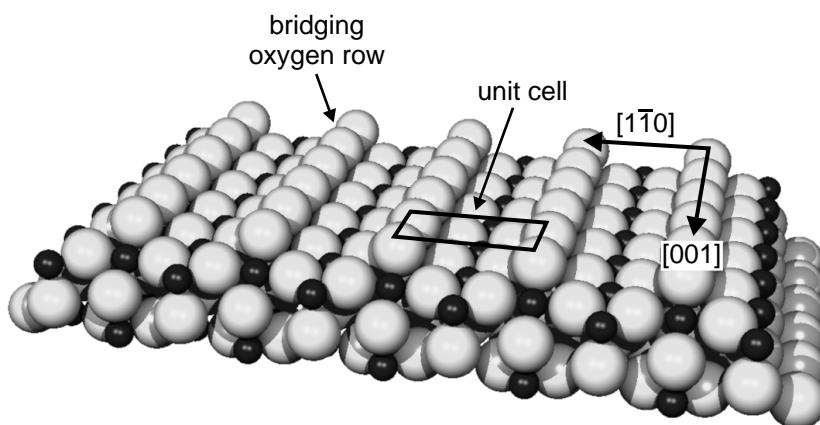
Figure 3.2: *Schematic representation of the 110 surface of titanium dioxide. Titanium atoms are indicated by dark spheres, oxygen atoms by the light spheres. The unit cell measures 6.50 Å along $[1\bar{1}0]$ and 2.96 Å along $[001]$.*

surface. Most striking are the so called bridging oxygen atoms, which form rows along the [001] direction. Since a TiO$_2$ crystal treated in UHV is always slightly reduced, oxygen vacancies will also be present at the surface. For example a bridging oxygen atom could be missing, or one of the in-plane oxygen atoms. Even oxygen vacancies in the sub-surface region, just one or two layers deep, might influence the surface.

3.3 Experimental procedures

The experiments described in this chapter were performed in the UHV set-up described in Chapter 2. The 1×1 cm^2 polished TiO$_2$ single crystals used in this work were obtained from the Surface Preparation Laboratory [61]. The samples were mounted in a molybdenum holder which could be heated by thermal radiation and electron bombardment from a tungsten filament. The samples were prepared by a combination of sputter cleaning and annealing. For sputtering we always used 600 eV Ar$^+$ ions, with a total current collected on the sample holder of 1 μA. LEED was used to check the crystallographic ordering at the surface whereas AES (and later XPS) were used to inspect the composition. AES was also used to check the conductivity of the samples by checking the positions of the Ti and O peaks. If the

sample charges under the influence of the irradiating electron beam these peaks shift.

Newly introduced, fully oxidized samples have a very poor conductivity, as expected. We observed positive shifts in the Auger peaks of 80 eV or more, when we used a beam energy of 2.5 keV and a target current of 1 μA. This shift indicates a negative surface charging. Annealing for 10 min to 800 K turned out to be sufficient to lower the resistance of the sample below or close to 1 MΩ. In nearly all cases our crystals had a light blue color which indicates that the bulk of the crystals was only mildly reduced. Only in a few cases the bulk of the sample was more strongly reduced and where this is the case it will be mentioned.

Titanium dioxide is relatively inert and therefore contamination is usually not a major problem. Nevertheless we found small amounts (typically a few percent of a monolayer) of K and Ca on some crystals. This could be removed by repeated cycles of 30 min sputtering and 10 min annealing to 800 − 1000 K. Typically, after 10 – 20 cycles no contamination could be detected anymore. For further preparation several combinations of sputtering dose, annealing time and annealing temperature were used in this project. The precise preparation details and their effect on the resulting surface morphology will be discussed in Section 3.4.

The STM measurements were all performed at room temperature with tungsten tips that were electrochemically etched. Best results were obtained with relatively large positive sample bias (≈ 2 V) and low currents (≈ 0.1 nA). Although tip changes can greatly change the appearance of the STM images we did not find indications of tip induced changes at the surface under these conditions.

3.4   Results

3.4.1 The titania surface in UHV

The observed surface structure of the TiO_2 (110) crystal depends strongly on the preparation procedure. Annealing time and temperature, and sputter dose play a role, as well as the preceding sample history. When the sample is sputtered, the surface is damaged severely. Crystallographic order is destroyed and roughness is created. After sputtering, LEED only shows a uniform background, indicating the absence of crystallographic order at the surface. Also the XPS spectrum is strongly affected by sputtering. Consistent with the model shown in Figure 3.2 all Ti atoms on the annealed surface are in the 4+ state. After sputtering, however, we observe
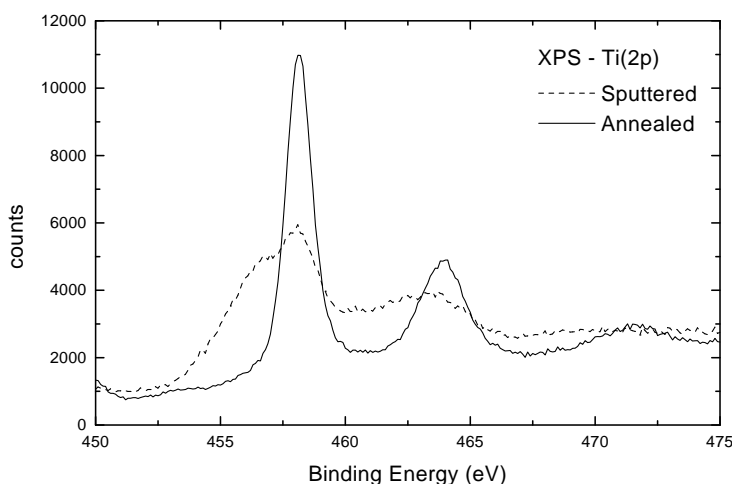
Figure 3.3: *XPS spectrum of the Ti–2p peak after sputtering (dashed line), and subsequent annealing to 920 K (solid line). Sputtering was performed with 600 eV Ar$^+$-ions for 10 min at a target current of 1 μA. The spectrum after annealing is characteristic for Ti^{4+}, whereas the low energy shoulder after sputtering is a Ti^{3+} contribution [50]. The sample was irradiated with Mg Kα radiation (1253.6 eV) and the pass energy of the analyzer was set to 20 eV.*

a large fraction of Ti^{3+}, as is shown in Figure 3.3. After annealing to 920 K LEED shows a 1 × 1 pattern, and only Ti^{4+} is observed [50]. Since the total Ti:O signal ratio does not change significantly, the Ti^{3+} signal probably reflects local disorder, which causes some Ti atoms to be coordinated by a lower number of oxygen atoms than in the bulk structure.

After 15 minutes of sputtering and 10 minutes of annealing to 850 K also a 1 × 1 LEED pattern is obtained. An STM image of the resulting surface morphology is shown in Figure 3.4a. Subsequently annealing the sample to 900 K for 20 min results in the image shown in Fig. 3.4b. The LEED pattern indicates that at short length scales the crystallographic order was already restored in the first annealing step, but the STM images show that on a larger scale there is still 'damage' present in the form of steps. The islands and vacancy islands are small and irregularly shaped, but grow upon further annealing as is evident from comparing Figures 3.4a and b. In the lower left part of Figure 3.4a mainly vacancy islands are present, whereas in the right part one can observe both islands and vacancy
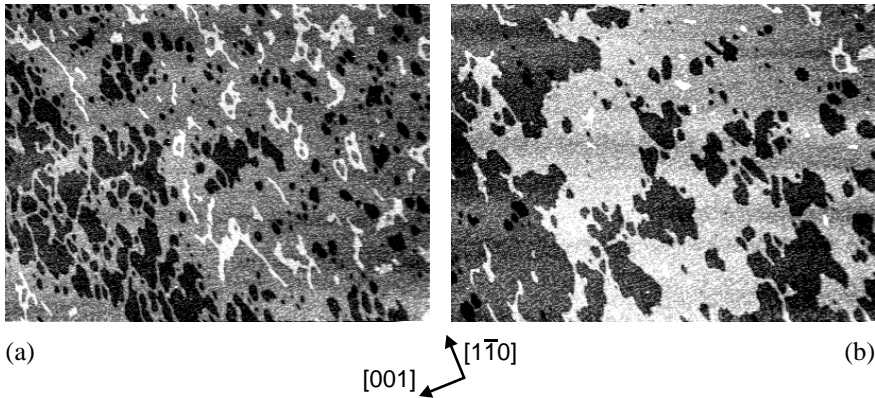
Figure 3.4: *Two STM images illustrating the annealing process of the TiO$_2$ (110) surface. Image (a) was recorded after 15 min sputtering and 10 min annealing to 850 K, whereas (b) was recorded after subsequently annealing the sample to 900 K for 20 min. Both images have dimensions 5550 Å × 4160 Å and were recorded with sample bias V$_t$ =2 V, and tunneling current I$_t$ =0.1 nA. The islands and vacancy islands grow in size upon annealing and are irregularly shaped.*

islands. Due to the miscut of the sample with respect to the (110) direction the surface shows regions with mainly islands and regions with mainly vacancy islands. In between these regions both kinds of islands are present. In regions where both islands and vacancy islands are present, the step density is usually lower than in regions where only one of the two kinds is present. This is illustrated in Figure 3.4a. In this image the step density is higher at the left side of the image (mainly vacancy islands) than on the right side of the image (both islands and vacancy islands).

The STM images shown in Figure 3.5 were obtained after 10 min sputtering and 10 min annealing to 920 K. They were accompanied by a good quality 1 × 1 LEED pattern. The large scale image (Fig. 3.5a) shows large terraces, although also some smaller islands are present on the surface. In the small scale image (Fig. 3.5b) rows parallel to the [001] direction with a width of 6.5 Å can be observed. Comparing this with the model shown in Fig. 3.2 one is tempted to associate these bright rows with the rows of bridging oxygen atoms, which are also separated by 6.5 Å. However, the Scanning Tunneling Microscope does not simply image the topography, but combines topographic and electronic information. The bright rows have been assigned both to the bridging oxygen rows [62] and to the exposed Ti ions in between these rows [53,63]. The STM contrast has been found to depend

(a) [001] [1$\bar{1}$0] (b)
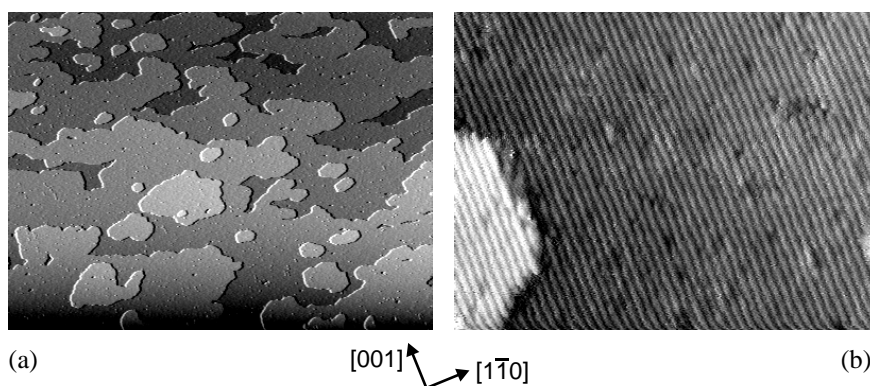
Figure 3.5: *STM images obtained after 10 min sputtering and 10 min annealing to 920 K. (a) Large scale image (5550 Å × 4160 Å) showing large terraces with some smaller islands. (b) Small area scan (333 Å × 250 Å) showing the atomic corrugation along the [001] direction. The dark features along the rows are ascribed to oxygen vacancies. Both images were recorded with $V_t = 2.9$ V and $I_t = 0.07$ nA.*

on the tunneling conditions, and contrast reversal has been observed [64]. Closer inspection of Figure 3.5b reveals another feature. Several depressions seem to be present in the bright rows. These correspond most likely to missing oxygen atoms [62], and we will come back to this in section 3.5.

When the sample is heated to higher temperatures this has a marked effect on the surface morphology. In Figure 3.6 STM images are shown of a TiO$_2$ crystal which was prepared by 15 min sputtering and 10 min annealing to 1150 K. In these images the terraces are covered by one-dimensional structures. In between these bright 'added rows' again the 1 × 1 structure as well as isolated defects can be observed. LEED still shows the 1 × 1 spots, but now also streaks along the [1$\bar{1}$0] direction can be observed. The steps in Fig. 3.6 mainly consist of straight segments (especially along [001]) and sharp corners.

After treating the sample at again higher temperatures, or simply annealing it longer we see an increase of the density of the added rows observed in Fig. 3.6. In Figure 3.7 STM images of the surface are shown, obtained after annealing the surface shown in Fig. 3.6 for another 20 min to 1150 K. The surface is completely covered by bright rows and a 1 × 2 structure is formed. This is confirmed by LEED which shows a 1 × 2 diffraction pattern. At this high temperature the color of the sample changes quickly. The treatment resulted in a dark blue crystal. The terraces

(a)

(b)
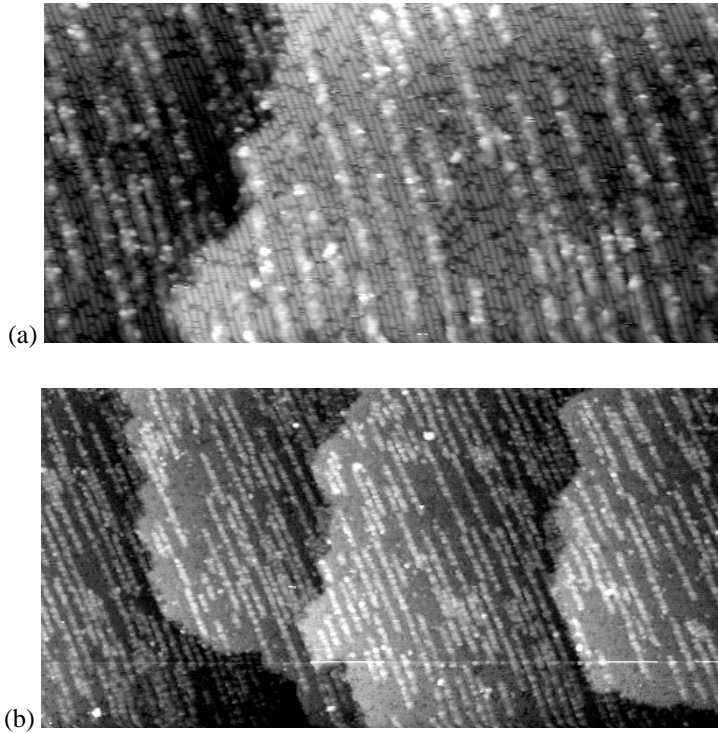
Figure 3.6: *STM images of the TiO$_2$ (110) surface after 15 min sputtering and 10 min annealing to 1150 K. In both images bright one-dimensional structures, 'added rows', can be observed. In (a) one can also observe the corrugation shown in Fig. 3.5b as well as many isolated defects (dark spots) (700 Å × 350 Å). Image (b), 1735 Å × 868 Å, shows that the steps have straight sections along the [001] direction. Both images were recorded with V$_t$ =2.0 V and I$_t$ =0.1 nA*

(a)

(b)

(c)
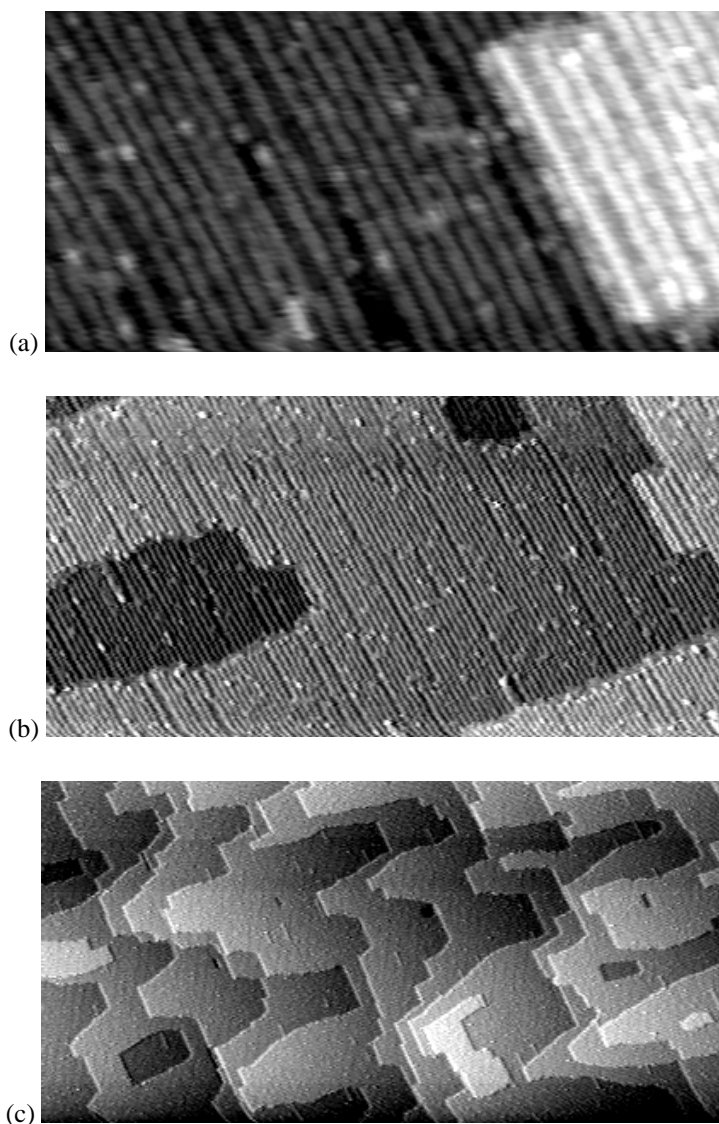
Figure 3.7: *STM images of the 1 × 2 structure which is formed on a reduced sample after 30 min annealing to 1150 K, recorded with V$_t$ =2.0 V and I$_t$ =0.1 nA. (a) 416 Å × 208 Å, (b) 1365 Å × 683 Å and (c) 5550 Å × 2775 Å. In image (c) one can clearly see that steps prefer the ⟨001⟩ and ⟨1$\bar{1}$1⟩ directions.*
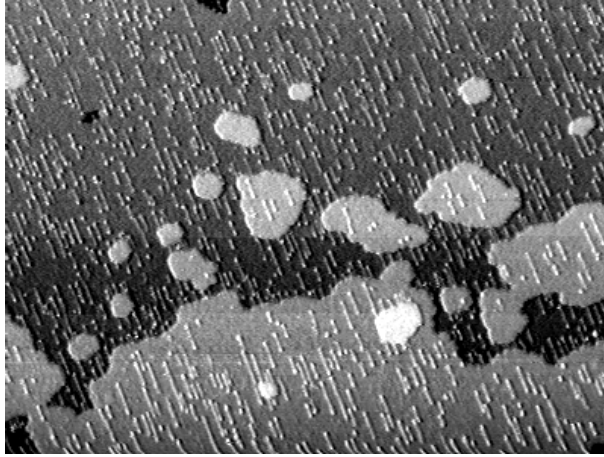
Figure 3.8: *STM image of the TiO$_2$ (110) surface after 30 min sputtering and 10 min annealing to 920 K. Large terraces with some smaller islands can be seen. Terraces are covered by added rows. Another experiment under similar conditions (Fig. 3.5) resulted in a surface with a much lower density of added rows. This difference is probably related to a difference in sample history. The dimensions of the image are 2220 Å × 1665 Å (V_t = 2.5 V and I_t = 0.2 nA).*

can be quite large, of course depending on the local miscut angle with respect to the (110) plane. Steps have a very clear preference for certain specific directions, mainly $\langle 001 \rangle$ and $\langle 1\bar{1}1 \rangle$. As will be discussed below, the formation of the 'added rows' is related to the reduction of the oxide.

Summarizing, at low annealing temperatures a 1 × 1 surface structure is formed with small terraces with irregular shapes. At high temperatures one-dimensional rows and eventually a 1 × 2 reconstruction are formed. The terraces are large and steps often are straight, running preferentially along the $\langle 001 \rangle$ and $\langle 1\bar{1}1 \rangle$ directions.

Unfortunately, this is not the complete story. As was explained before, the annealing temperature and sputter dose are not the only important parameters and therefore the preparation can sometimes be seemingly irreproducible. This is illustrated in Figure 3.8. This STM image was obtained after 30 min sputtering and 10 min annealing to 920 K. This is basically the same treatment as was used to obtain the images shown in Fig. 3.5. Comparing the images in Figures 3.5 and 3.8 one can see a large difference in added row density. Although a high density of
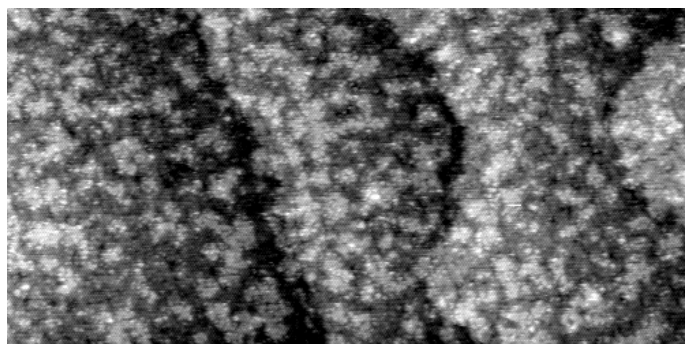
Figure 3.9: *STM image of a sample which was annealed to 1150 K for 10 min and exposed to 10^{-6} mbar oxygen during the first 15 min after switching off the heating power (1805 Å × 903 Å, V_t =2.0 V, I_t =0.1 nA). On top of already existing, large terraces many small new islands with irregular shapes have been formed.*

added rows can be observed in Fig. 3.8, the steps do not have many straight sections along [001] and do not have many sharp corners, as is observed in most cases on strongly reduced surfaces, like for example was shown in Fig. 3.6. Most likely these different results after similar treatments are related to differences in sample history.

3.4.2 Re-oxidation

In the previous section the effects of sample treatment on the resulting surface morphology were discussed. These results indicate that it is very hard to obtain a defect free surface with large terraces. Low temperature annealing results in high step densities, high temperature annealing in high oxygen vacancy concentrations and added rows. However, Pan *et al.* [50] reported that the oxygen vacancy concentration can be significantly reduced by exposing the sample to oxygen during the time in which the sample is cooling down to room temperature. STM measurements, however, reveal that the response of the surface to oxygen exposure is much more complicated than the mere filling of the oxygen vacancies. The STM image shown in Figure 3.9 was obtained after annealing the sample to 1150 K for 10 min and exposing the sample to 10^{-6} mbar of O$_2$ during the first 15 min after switching off the heating power. On the terrace many small islands are present. Thus, although the oxygen vacancy concentration may have decreased, the step density
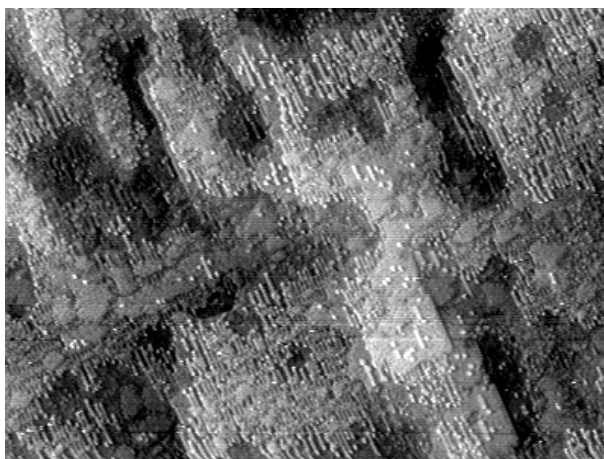
Figure 3.10: *STM image of a strongly reduced, dark blue TiO$_2$ crystal after reoxidation in 10^{-6} mbar O$_2$ at 750 K for 45 minutes. This results in a rough surface with many small terraces. A large part of the surface is densely covered by added rows (1667 Å × 1250 Å, V_t =2.0 V, I_t =0.07 nA).*

has definitely increased. If the sample is annealed in an oxygen atmosphere the changes are even more dramatic. An STM image measured on a strongly reduced dark blue sample which was annealed to 750 K for 45 min in a 10^{-6} mbar O$_2$ atmosphere is shown in Figure 3.10. The surface has become very rough, and even though the sample was exposed to oxygen, added rows are still present.

3.5   Discussion

We have shown that after relatively low temperature annealing the terraces are small and the step density is quite high. Many islands and vacancy islands have irregular shapes. This morphology is probably the result of only a partial restoration of the roughness created by ion sputtering. During annealing the terrace structure is restored and the islands grow in lateral size. Due to the low temperature, however, this process is not fully completed. The irregular shapes are caused by a memory of the coalescence events by which the islands and vacancy islands can grow. Regions with mainly islands and regions with mainly vacancy islands are alternatingly present on the surface. In the intermediate regions where both kinds of islands are present the step density is lower than in the regions where one of the

two clearly dominates. This is probably related to the miscut of the sample surface with respect to the (110) direction and the ion sputter dose. When precisely an integer number of crystallographic layers is removed, the damage is more easily restored than when half a layer more (or less) is removed [65]. Initially, flattening can proceed very fast by filling the depressions with the elevated regions. This can proceed until only two or three levels are exposed, and only islands and vacancy islands are left. If precisely an integer number of layers is removed during sputtering, the amount of material in islands is equal to the amount missing in the vacancy islands, and the surface can easily flatten by filling the vacancy islands by the islands. If only islands or only vacancy islands are left, the annealing process is much more difficult, requiring ripening or coalescence growth of these (vacancy) islands [65].

If the crystal is annealed longer or at higher temperature the islands grow to larger sizes, as illustrated in Figure 3.4b. Eventually the steps run predominantly along the directions with the lowest step free energy. Since we observe steps mainly along $\langle 001 \rangle$ and $\langle 1\bar{1}1 \rangle$ these are probably the directions with the lowest step free energy. These observations are in agreement with previous findings [53, 56, 66] and it has been argued that these orientations are favoured because in these directions steps can be formed which are *autocompensated* or *charge neutral* [66].

As was mentioned in the previous section, it has been a longstanding issue whether the Ti or the O atoms are 'seen' in images with atomic corrugation, such as Figure 3.5. Fischer, *et al.* [62] concluded that the bright rows correspond to the bridging oxygen rows. They observed dark pits in these rows and assigned these to missing bridging oxygen atoms. However, most of the recent studies concluded that the bright rows correspond to the rows of Ti atoms in between the bridging oxygens. Onishi *et al.* [53] observed that formate ions adsorbed on top of the bright rows, which indicates that these are probably Ti atoms. Diebold *et al.* [63] also concluded that the Ti atoms are imaged bright and observed bright features between the bright rows. They attributed these bright spots to isolated oxygen vacancies. This seemed to have solved the controversy, but very recently Suzuki *et al.* [67] concluded that the bright spots observed by Diebold *et al.* might very well be due to adsorbed hydrogen instead of oxygen vacancies. The hydrogen atoms may form hydroxyl species (O-H) on bridging oxygen rows, and hydride species (Ti-H) on oxygen vacancies [67].

In our measurements we usually observe dark spots on the bright rows, in agreement with the observations by Fischer *et al.* [62]. However, the appearance of these defects depends strongly on the state of the STM tip, as was also noticed already by Diebold *et al.* [66]. Since we could not detect contamination which could account for these dark spots, hydrogen (which is not detected by AES and XPS) and oxygen vacancies seem to be the only two possible explanations for these features. Since Suzuki *et al.* concluded from a combination of STM and ESD measurements that hydrogen is imaged as a bright feature [67], it is tempting to associate the dark features with oxygen vacancies. However, there can be different kinds of oxygen vacancies, for example missing bridging oxygen atoms, missing in-plane oxygen atoms, and even subsurface defects. The appearance of each of these defects will vary with the tip state [66], so that a definite assignment can probably not be made on the basis of STM measurements alone. The origin of the hydrogen (or hydroxyl) species in the measurements of Suzuki *et al.* is not very clear. There may be some dissociative adsorption of water molecules from the residual gas in the vacuum chamber. Alternatively hydrogen atoms may be present in the bulk of the crystal and diffuse towards the surface. The sticking and dissociation probabilities for hydrogen molecules are very low, probably requiring steps or defect sites [19, 50]. Furthermore, water and hydroxyl groups desorb far below the annealing temperature. This argument was used by Diebold *et al.* [66] to exclude the possibility that hydrogen species are responsible for the features with a coverage of roughly 10% in their measurements. Finally, the density of the atomic size depressions seems to increase with increasing annealing time and annealing temperature. This indicates that the density is probably related to the degree of bulk reduction.

In summary, all studies agree on the fact that oxygen vacancies are present at the surface. Their appearance may differ from one study to another, but this may be related to differences in tip state. The presence of hydrogen or hydroxyl groups on the surface may result in features with a similar shape, but it can probably not explain the relatively high density of point 'defects'. Based on this body of circumstantial evidence we assume throughout the remainder of this thesis that the dark spots in our images are oxygen vacancies.

In the literature several models have also been described to explain the one-dimensional features in Fig. 3.6. The simplest model, assumes the removal of a row of bridging oxygens, which would expose the Ti atoms underneath. This could in-

crease the tunneling probability and thus result in an apparent increase in height. However, this model can be disqualified on the basis of conflicting AFM and ES-DIAD measurements [68, 69]. In two other models the bright rows represent true topographic information, i.e. both models assume added rows to be present on the surface. Onishi *et al.* [52] proposed a row structure with a Ti$_2$O$_3$ composition, whereas more recently Pang *et al.* [70] proposed a structure which continues the bulk rutile structure and results in an added row with a Ti$_3$O$_5$ composition. Our measurements do not clearly favour one of the two models. In fact, very recently it was suggested that both structures might be present at the surface [71]. All models developed for these added or missing row structures have in common that they correspond to a lower O:Ti ratio than the normal TiO$_2$ stoichiometry. This agrees with our experience that the added row density is usually higher on samples with a darker color and thus a larger degree of bulk reduction.

When the added row density is low these rows do not show up in the LEED pattern, and a normal 1×1 pattern is observed. When the density of rows increases this will start to affect the LEED pattern, but since the rows are not very regularly distributed, they show up as diffuse streaks along the $[1\bar{1}0]$ direction. Only when the density becomes so high that the rows order, the LEED pattern shows extra spots and the 1×2 pattern is observed.

Evidently the formation of added rows is energetically favoured on reduced samples and at high temperatures. However, the rate of formation can differ largely even under seemingly similar conditions and on samples with a similar degree of reduction as is illustrated by the difference between Figures 3.5 and 3.8. In fact the sample shown in Figure 3.8 was probably less reduced than the one in Fig. 3.5, as it was exposed to a lower number of sputter/annealing cycles. Since both the isolated defects and the added rows are related to missing oxygen, the density of these features depends on the density of oxygen vacancies in the surface region. When the sample is annealed at high temperatures, oxygen vacancies are created at the surface, and when the bulk of the sample is strongly reduced, oxygen vacancies from the bulk can diffuse to the surface. Because there is a difference in the density of defects at the surface and the density of defects in the bulk also the sputter dose in the cleaning cycles, i.e. the extent to which the oxygen depleted surface layer is removed, is important. Although it seems obvious that diffusion of oxygen vacancies in a reduced crystal plays a role, it has been argued that the diffusion of Ti interstitials present in the bulk is also important, and probably even

dominates [60, 72].

The added row structures are most likely formed when Ti interstitials from the bulk of the sample diffuse to the surface [53]. In that scenario the nucleation rate of the rows depends both on the Ti interstitial concentration, i.e. the degree of reduction, and the rate of diffusion of these Ti interstitials and thus on temperature. We often see the added rows growing out of a higher terrace (see Fig. 3.8). In that case the step provides the necessary material. When the sample is reduced, many properties change, as is evident from the changes in color and electrical conduction. It might be that also the diffusion rate of the Ti interstitials is affected by the degree of reduction and accompanying structural changes in the bulk [73]. This could result in a very complex dependence of the added row density on both annealing temperature and degree of bulk reduction, which might explain some of the seemingly contradicting results.

The reoxidation reaction at the surface of reduced TiO_2 (110) has attracted a lot of very recent interest from several groups [71, 73–76]. The behaviour under oxidizing conditions is even more complicated than what is observed in UHV. All studies consistently show that the exposure to oxygen at elevated temperature can lead to a major restructuring at the surface, as we observed in Figures 3.9 and 3.10. The nucleation of new 1×1 terraces, of two types of added rows and of a rosette-like structure have all been reported. These observations are most easily explained by the diffusion of Ti interstitials from the reduced bulk to the surface. At the surface, added rows and/or rosette-like structures can be formed which can be oxidized to new 1×1 terraces. In this way small islands on top of the existing terraces are formed. But as the process continues also on these islands added rows are formed, which can be oxidized, and so on. Finally the surface can become quite rough. *In-situ* measurements [74, 76] confirm this scenario and also our measurements fit in this description. The surface shown in Fig. 3.9 was only exposed to oxygen when the sample was cooling down. Therefore it was only briefly at an elevated temperature during the exposure. At low temperatures oxygen exposure does not affect the surface noticeably. Therefore only small new islands were formed and the process could not continue. The image shown in Fig. 3.10 was recorded after long annealing in oxygen and therefore the process progressed much further. Indeed we see that the surface has become rough. Many small islands are present, many of which are also covered by added rows. All of this is in agreement with the description given above.

The influence of hydrogen on the TiO$_2$ (110) surface is discussed in Chapter 7. At room temperature exposure to 10^{-5} mbar H$_2$ does not result in changes in surface morphology. At higher temperatures similar exposures lead to an enhanced reduction. Under 'normal' conditions the hydrogen partial pressure is $< 10^{-9}$ mbar and the effect is expected to be negligible.

3.6 Conclusions

The behaviour and surface morphology of TiO$_2$ (110) are quite complex. Besides steps, also isolated point defects and added rows are formed at elevated temperatures. Most likely the formation of these features is related to a change in composition, i.e. reduction, of the surface region. Their appearance in the STM images is depending on the tip state. At elevated temperatures oxygen vacancies and Ti interstitials are created at the surface and in the bulk. These defects can diffuse from the surface to the bulk and vice versa. At the surface atomic-scale depressions are observed, as well as bright lines. The depressions are probably oxygen vacancies, whereas Ti interstitials organize themselves in added rows (the bright lines) with either Ti$_2$O$_3$ or Ti$_3$O$_5$ composition. The density of these rows increases with annealing temperature and bulk reduction of the crystal. High densities of added rows result in a transformation of the 1×1 structure to a 1×2 reconstruction. After annealing to elevated temperatures steps run mainly along the $\langle 001 \rangle$ and $\langle 1\bar{1}1 \rangle$ directions, although in the next chapter we will see that probably this too depends on starting conditions and level of reduction. Upon re-oxidation of a reduced crystal, the crystal forms new oxide layers on top of existing terraces. The continuous nucleation of new layer results in significantly rougher surfaces after oxidation.

Since it was our aim to use the TiO$_2$ surface as the starting point, as the model support, of our model catalyst, we will now consider how well the results of the different treatments suit the requirements in that respect. Ideally we would like to prepare a flat surface with large terraces, without defects. In order to minimize the density of defects and the degree of reduction one would need to use low annealing temperatures and/or expose the sample to oxygen in order to re-oxidize it. Both procedures result in a rough surface with a large step density. On such a rough surface deposited metal will probably stick to the steps and will be hard to identify with the Scanning Tunneling Microscope. Large terraces can easily be

obtained by heating the sample to sufficiently higher temperatures. However, this results in a very rapid reduction of the crystal and this change in composition is likely to have significant consequences. Therefore the substrates used in the following chapters were prepared by a combination of sputtering and annealing in the intermediate temperature range of $900 - 1000\,\mathrm{K}$. This results in surfaces flat enough to 'find' the deposited material. Although at the surface defects are formed the crystal stays partially transparent indicating that the bulk composition is still nearly stoichiometric. However, before using this oxide as a substrate for further studies, we discuss in the next chapter how the surface responds to more severe changes in stoichiometry.

IV

The effect of stoichiometry on the direction of steps on TiO$_2$ (110)

The equilibrium composition of titanium oxide depends on temperature and partial oxygen pressure. Deviations from the TiO$_2$ stoichiometry cause changes in color and an increase in electrical conductivity. In this chapter we use ex-situ Atomic Force Microscopy observations to show that changes in stoichiometry also affect the morphology of steps on the TiO$_2$ (110) surface. Upon annealing a sputtered stoichiometric surface at 1135 K, first hexagonal islands are formed. During further annealing these hexagonal shapes do not simply grow in size. Instead elongated structures form along the [001] direction, and the surface tends to maximize the length of the [001] steps. We propose that the formation of a [001] step allows the surface to make a non-stoichiometric structure without destroying the crystal structure. Finally, after annealing at 1170 K, we find that [001] is still a favoured step direction but the elongated structures are no longer formed. We suggest that other structures, such as added rows are formed to accommodate the non-stoichiometry.

4.1   Introduction

Titanium dioxide and its (110) termination were introduced in Chapter 3. TiO$_2$ plays an important part in research of metal oxide surfaces since it was found to be an efficient catalyst for the dissociation of water [45], and it is currently being used in a variety of applications, ranging from gas sensing to photocatalysis. Furthermore it is used as a support material in heterogeneous catalysis and it is one of the components of the TiO$_2$-V$_2$O$_5$ catalyst that is being used for the reduction

of NO_x with NH_3. In Chapter 3 we already saw that the composition of titanium oxide is not constant but depends on the preparation conditions.

The equilibrium stoichiometry depends both on temperature and on partial oxygen pressure. Typical surface science preparation procedures in ultra-high vacuum (UHV) usually result in crystals that are slightly oxygen deficient. Even though deviations from 'perfect' TiO_2 stoichiometry can be very small ($< 10^{-4} - 10^{-3}$ [58, 59, 77]) the consequences can be severe. The color changes from transparent via blue to black with increasing oxygen depletion, and at the same time the electrical conductivity increases strongly.

In this chapter we show that changes in composition affect the surface morphology. In particular the relative energies of steps in different directions depend on the average stoichiometry of the surface. When TiO_2 (110) is annealed and the oxide becomes increasingly depleted in oxygen, the equilibrium shapes of islands and vacancy islands change, and one specific step direction becomes strongly favoured over the others.

4.2   Experimental procedures

The experiments described in this chapter were *not* performed with the set-up described in Chapter 2. Instead, the samples were prepared in a high vacuum (HV) chamber with a base pressure of 2×10^{-8} mbar.

The preparation chamber was equipped with a broad-beam ion source for sputtering the sample surface (Kaufmann 3 cm ion source model II). A neutralizer was used to supply electrons to the sputter beam, to prevent the samples from charging up. The ion source was mounted under an angle of $45°$ with respect to the surface normal. The samples ($10 \times 10 \times 1$ mm³) were mounted in the same molybdenum holder that was used in the Nacra system (see Chapter 2). The upper part of the holder was mounted on a ceramic plate, and therefore the holder was electrically isolated from the vacuum chamber.

The sample was heated by thermal radiation from a filament to the back part of the sample holder. Additional heating was achieved by bombarding the holder with 1.2 keV electrons. In this way a total heating power of 83 Watt could be achieved. The temperature of the sample was measured both with a pyrometer and with an chromel-alumel thermocouple, attached to the sample holder within 1 mm of the side of the sample. The reading of the thermocouple could be as much

as 50 K lower than that of the pyrometer due to a significant temperature difference between sample and holder. Independent calibration measurements indicated that the pyrometer provided the most reliable estimates for the real sample temperature. Therefore the temperatures mentioned in the rest of this chapter are the pyrometer values.

After the preparation, the samples were removed from the HV chamber and characterized with Atomic Force Microscopy (AFM). The AFM measurements were performed at room temperature, in air, with a Nanoscope II from Digital Instruments. We used commercially available Si_3N_4 tips (Digital Instruments standard tips) and imaged the surface in contact mode. The stability of the TiO_2 during the AFM measurements was checked by scanning the same area of the surface several times, and by imaging a different area of the same sample again a few days later. We found no indications of scanning induced changes at the surface, and storing the samples in air for a few days did not change the surface morphology.

A separate UHV chamber was used to examine the samples with Low Energy Electron Diffraction (LEED) and Auger Electron Spectroscopy (AES). The base pressure of this system was 1×10^{-10} mbar, and LEED and AES were performed with a 4-grid LEED system with a Retarding Field Analyzer. The samples were transferred from the preparation chamber to this UHV chamber through air. Without further treatment we could not observe a LEED pattern. However, after slightly heating the sample to 750 K in order to desorb the contaminants from the ambient atmosphere, vague 1×1 spots could be observed. These spots were sufficiently intense to determine the crystallographic directions of the sample.

Each series of experiments started with a new stoichiometric, fully transparent sample. First the samples were sputtered with Ar^+-ions with a high dose (up to 20 mC/cm^2), and then annealed to temperatures in the range of 1000 to 1300 K. The heating rate was approximately 10 K/min in all experiments, the cooling rate was 20 K/min. In order to investigate the restoration process of the surface damage introduced by sputtering, we interrupted the annealing several times. At this point the sample was taken out of the HV chamber and the surface topography was imaged with AFM. After imaging, the sample was reloaded into the preparation chamber and annealing continued. After the last AFM measurements the samples were transferred to the UHV chamber in order to check the crystallographic orientation and possible contamination of the samples with LEED and AES. The contamination level on our samples was below the detection limit of the AES sys-

tem (a few percent of a monolayer). However, when the sample is exposed to air, probably a layer of water adsorbs and hydroxyl groups are formed. Since oxygen is part of the substrate and hydrogen is not detected with AES, adsorption of water cannot be detected with AES. Thus, the presence of a layer of water may explain the absence of a LEED pattern before extra treatments. At the preparation temperatures of 750 K and higher water desorbs from TiO$_2$.

4.3 Results

In many studies on TiO$_2$ it has been found that the surface morphology can depend critically on the preparation history, via the degree of bulk reduction (see for example Chapter 3 and Refs. [19, 49]). In order to maximize the reproducibility of the experiments, we started each series of experiments with a new, stoichiometric, fully oxidized, transparent sample. The result of a typical series of experiments is shown in Figures 4.1 and 4.2.

First, the stoichiometric crystal was sputtered in the HV preparation chamber with 620 eV Ar$^+$-ions (15 μA/cm^2 for 30 minutes). As is shown in Figure 4.1, sputtering results in a surface with a relatively large roughness at short length scales. The vertical corrugation of the surface is about 2.5 nm. This corresponds to height differences of 7 to 8 layers of oxide. As is shown below, individual levels can easily be distinguished with AFM. The small structures are roughly oriented along the [001] direction, which coincides with the direction of sputtering. Previous Scanning Tunneling Microscopy measurements in UHV also showed a rough surface with much small scale structure, but they did not show anisotropy in the structure [53]. The formation of these ripple-like structures may very well depend on the precise sputtering conditions [78–81].

AFM images at different stages of annealing in HV are shown in Figure 4.2. The images illustrate the repair of the sputter damage, and the flattening of the surface in a single series of experiments. In other series we reproduced the qualitative behaviour. The surface was annealed to 1135 K for 10, 20, 30 and 60 minutes respectively. After 10 minutes (Fig. 4.2a) much of the very short length scale damage has been removed and elongated hexagonal structures have formed, with steps running mainly along the [001], [$\bar{1}$11] and [1$\bar{1}$1] directions. Upon further annealing (Figs. 4.2b–d) the structures on the surface become more and more elongated. First the hexagonal structures become rectangular, bounded by [001]
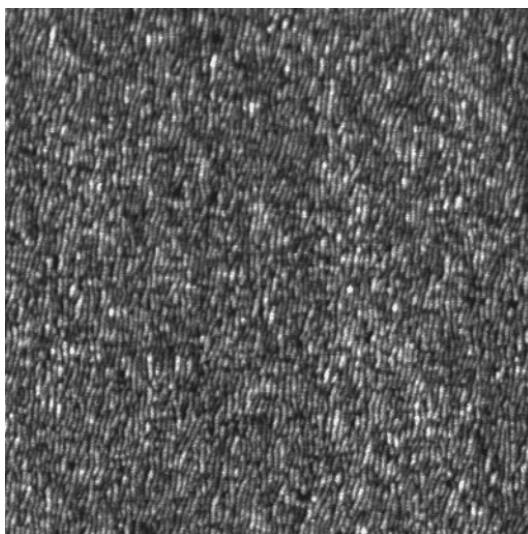
Figure 4.1: *AFM image of a rutile TiO$_2$ (110) surface after sputtering with Ar$^+$ ions (620 eV, 15 μA/cm^2 for 30 minutes) under an angle of 45° with respect to the surface normal. The size of this image is 1.00 μm × 1.00 μm, the vertical corrugation of the surface is about 2.5 nm. The small structures in the image are aligned along the [001] direction, which is the same as the direction under which the sputter-source is placed.*

and [1$\bar{1}$0] steps, but eventually very narrow pieces of terrace along the [001] direction appear, branching off from the [1$\bar{1}$0] steps. At this stage the [001] steps dominate the surface morphology. The number of atomic levels that can be seen in the images does not change from Figure 4.2a to d. The total step density increases by a factor 1.5 from Fig. 4.2a to Fig. 4.2d. Annealing also causes a reduction of the oxide crystal. This is evident from a change in visual appearance. The initially white transparent crystal becomes dark and opaque.

At slightly higher temperatures we did not observe the striking increase in step density. Figure 4.3 shows a similar series of experiments as shown above. A new, stoichiometric TiO$_2$ crystal was sputtered with 620 eV Ar$^+$-ions (20 μA/cm^2 for 25 minutes) and annealed in the HV preparation chamber to 1170 K for a total of 30 minutes (Fig. 4.3a) and 60 minutes (Fig. 4.3b) respectively. After annealing to 1170 K for 30 minutes we observe an array of strongly meandering steps, mainly dictated by the local miscut of the sample with respect to the perfect (110) orientation. Terraces are roughly 80 nm wide on average. In quite a few terraces

(a) 10 min

(b) 20 min

(c) 30 min

(d) 60 min

[001]

[$\bar{1}$11]

[1$\bar{1}$1]

[1$\bar{1}$0]
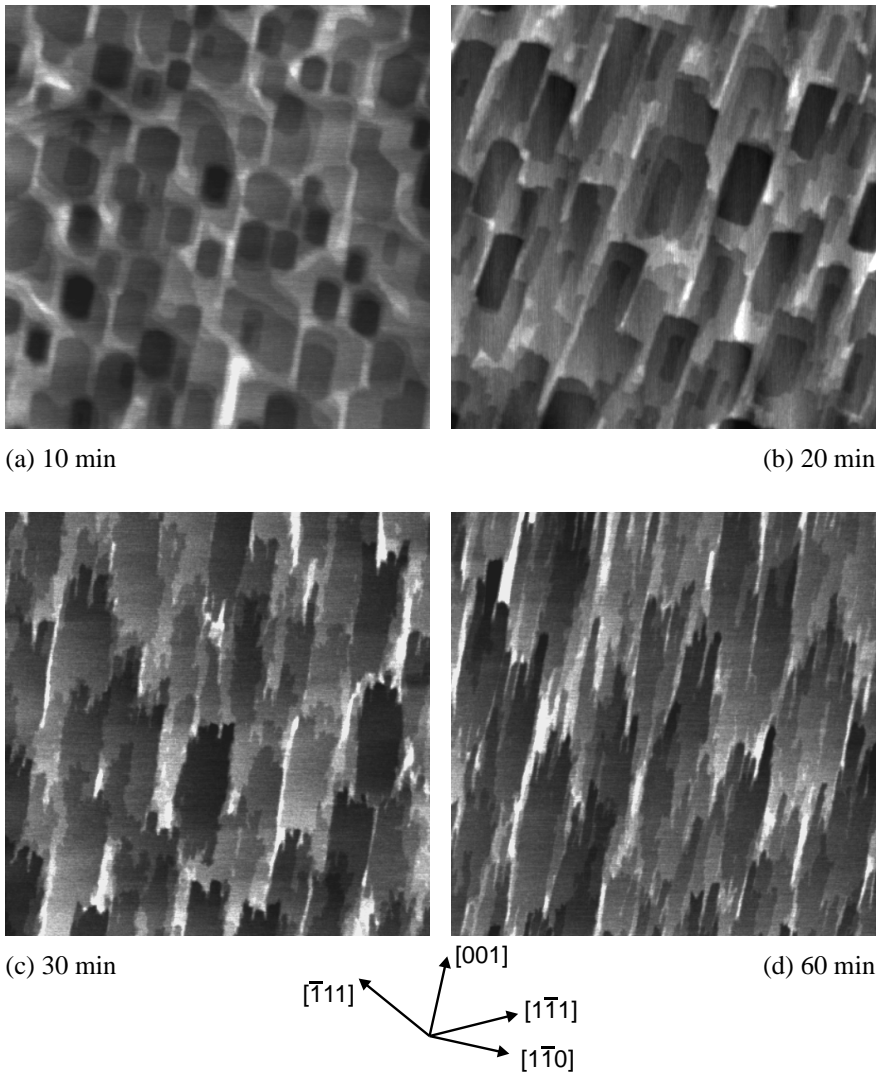
Figure 4.2: *This series of AFM images shows the changes in surface topography during annealing of a sputtered, stoichiometric crystal to 1135 K. All images measure 1.00 µm × 1.00 µm. They were recorded after (a) 10 min, (b) 20 min, (c) 30 min, and (d) 60 min of annealing. After 10 minutes, islands and holes have elongated hexagonal shapes and are bounded by steps running preferentially along* [001], [1$\bar{1}$1] *and* [$\bar{1}$11]. *During the annealing all features on the surface become more elongated. After 20 minutes rectangular structures have formed with* [001] *and* [1$\bar{1}$0] *steps. After 30 and 60 minutes narrow pieces of terrace along the* [001] *direction have appeared.*

(a)   (b)
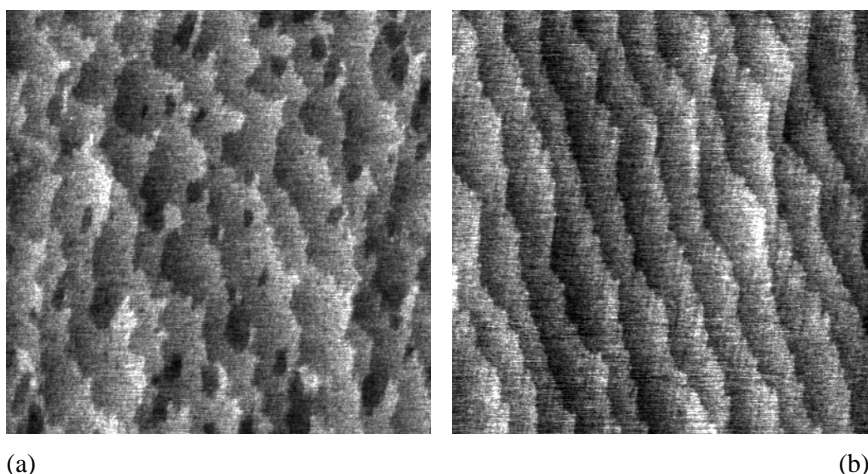
Figure 4.3: *These AFM images (1.00μm × 1.00μm) were acquired after sputtering a new TiO₂ crystal and annealing it to 1170 K for (a) 30 minutes and (b) 60 minutes. The images were measured in air. In both images an array of steps can be observed reflecting the local miscut of the sample with respect to the perfect (110) orientation. After 30 minutes the steps meander strongly and some vacancy islands are present. After 60 minutes these vacancy islands have disappeared, and the steps are more regular and show a preference for the [001] orientation.*

single atomic level deep vacancy islands are present. Upon further annealing (Fig. 4.3b) the steps become more regular and the vacancy islands disappear. As is evident from the many straight step sections, again the [001] direction is favoured, similar to the situation after annealing to 1135 K. However, we do not observe the formation of the thin elongated pieces of terrace that dominate the surface in Figs. 4.2c and d.

A smaller scale image of the surface after 60 minutes annealing to 1170 K reveals that there is also structure in the terrace that runs parallel to the [001] direction (Fig. 4.4). The period perpendicular to [001] is approximately 10 nm. This is an order of magnitude larger than the period of the common 1×2 reconstruction that forms on strongly reduced titania (see for example Chapter 3 and Refs. [53, 55, 70, 71]), and therefore it must have another origin than the 1×2 reconstruction.
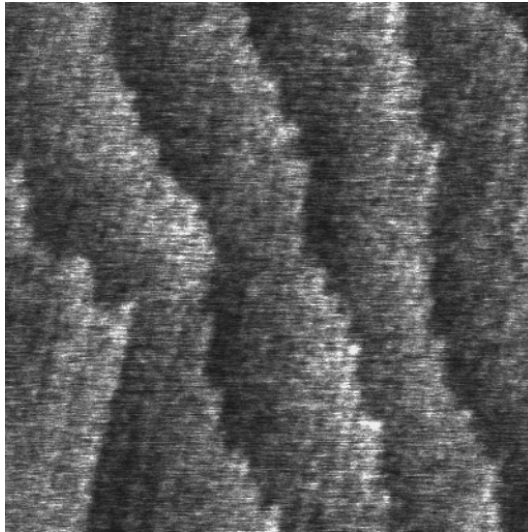
Figure 4.4: *Smaller scale AFM image (370 nm × 370 nm) of the surface shown in Figure 4.3b. The sample has been heated to 1170 K for 60 minutes. Steps have large straight sections along the [001] direction. On the terraces structures along [001] can be observed, with a periodicity perpendicular to the [001] direction of approximately 10 nm.*

4.4 Discussion

The changes in surface morphology observed at 1135 K (Figure 4.2) are very different from what is usually found in annealing experiments on sputtered surfaces. The equilibrium shape of islands and holes is determined by the relative values for the step free energies along the different directions, via the two-dimensional analogue of the well-known Wulff construction [82, 83]. Annealing usually makes all shapes (e.g. islands) more compact and leads to a steady increase of the average feature size and an accompanying decrease in the total step density. Upon annealing to 1135 K we observe a clear evolution towards less compact shapes, which is depicted schematically in Figure 4.5. After 10 minutes annealing most of the sputter damage has been removed and vacancy islands remain with an equilibrium shape that is close to hexagonal. It is clear that 10 minutes was not enough time for the surface to flatten completely but the uniformity in shapes and the straight sections of the steps indicate that on a local scale equilibrium has been reached. The main step directions, [001], [$\bar{1}$11], and [1$\bar{1}$1], have been argued to be the most
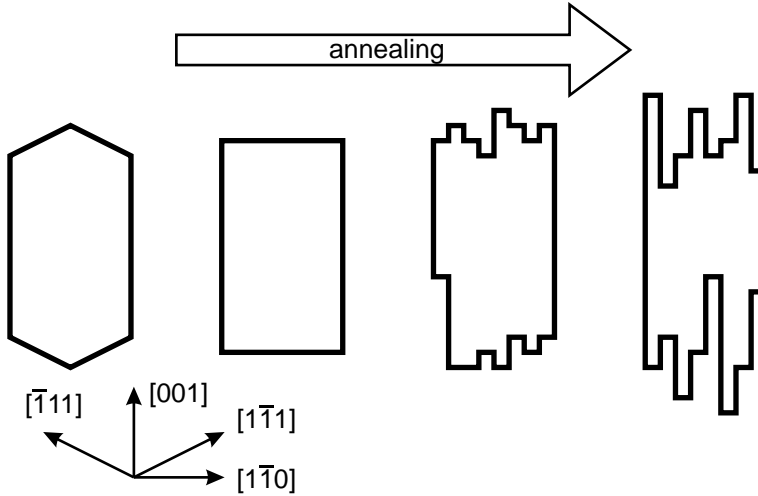
Figure 4.5: *Schematic representation of the changes in typical island shape on the TiO$_2$ (110) surface at different stages of annealing at 1135 K (see Fig. 4.2).*

stable on (near) stoichiometric TiO$_2$ (110) [53, 66]. However, upon further annealing the [001] steps become more and more favourable. After 30 and 60 minutes these steps apparently have become so low in energy that the surface starts making spontaneous [001] oriented excursions on the [1$\bar{1}$0] sides of the islands. In this way the total step density becomes substantially higher than the density necessary to accommodate the local roughness and the overall miscut. The surface could easily settle for straight [1$\bar{1}$0] steps, or even [1$\bar{1}$1] and [$\bar{1}$11] steps, but instead the surface *chooses* to zig-zag around this direction in order to *maximize* the length of the [001] step.

In order to quantify the changes in the AFM images we calculated the 2-dimensional autocorrelation function of the images. This measures the correlation between the height values of two pixels as a function of the distance between these pixels. Pixels that are very close together show positive correlation, i.e. they are likely to be at approximately the same height, and pixels that are far apart will show no correlation at all. This results in a central peak in the two-dimensional autocorrelation function. The full width at half maximum (FWHM) of this peak is a quantitative measure of the correlation length on the surface. In the 2-dimensional autocorrelation function this FWHM can easily be determined in two separate di-
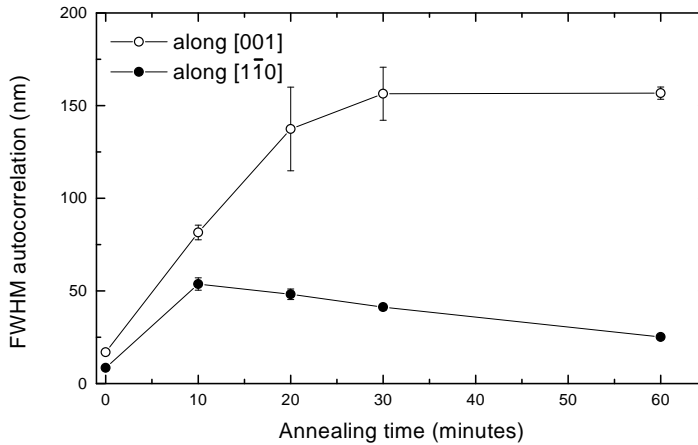
Figure 4.6: *The FWHM in the autocorrelation of the AFM images in the* $[001]$ *(open circles) and* $[1\bar{1}0]$ *(filled circles) directions. The solid lines serve as guides to the eye. The correlation length increases in the* $[001]$ *direction upon annealing to 1135 K, but in the* $[1\bar{1}0]$ *direction it decreases again after an initial increase.*

rections. In Figure 4.6 the FWHM has been plotted of the autocorrelation of the images shown in Figs. 4.1 and 4.2, along the $[001]$ and $[1\bar{1}0]$ directions. After sputtering, the correlation length is small, but it increases during annealing, as the surface rearranges. Along the $[001]$ direction the correlation length continues to grow up to 30 min of annealing, after which it levels off at a value close to the average terrace width in this direction. By contrast, after 10 min of annealing, the correlation length *decreases* in the perpendicular $[1\bar{1}0]$ direction! This is caused by the new, narrow excursions created along the $[001]$ direction. The initial increase in the correlation length along $[1\bar{1}0]$ proves that the surface is sufficiently mobile on the considered length scales and that the shape changes are not caused by kinetic limitations. The fact that the correlation length along $[1\bar{1}0]$ not only levels off, but actually decreases by a factor two, shows that the surface generates a significant extra density of steps along the $[001]$ direction. Fig. 4.6 suggests that the generation of extra $[001]$ steps is by no means finished after 60 minutes.

The most obvious reason for the spontaneous generation of steps during annealing lies in the change in composition taking place at the same time. We start with a stoichiometric crystal, but at these elevated temperatures oxygen is leaving the crystal. We speculate that the steps along [001] provide a way for the surface to

70

cope with the non-stoichiometry. STM studies of TiO_2 (110) in UHV have shown the formation of added row structures along [001] in response to reduction of the crystal [52, 53, 55, 62, 70, 71], and the evolution observed here may be a larger-scale manifestation of the same effect. After all, an added row can be thought of as an extremely narrow piece of terrace, basically only consisting of a step up, immediately followed by a step down. In other words, the natural composition of the step region could be lower in oxygen content than TiO_2, similar to the added rows. The AFM images seem to imply that the [001] steps form an energetically favourable way for the surface to accommodate moderate to high levels of oxygen deficiency.

Within the scenario outlined here, the highest density of missing oxygen is reached for the maximum step density, i.e. with up and down steps following each other immediately. This extreme structure is actually realized by the 1×2 reconstruction, which is formed spontaneously at high temperatures. We speculate that this is the end situation, which is not yet reached after 60 min at 1135 K, but which is close to completion after 60 min at 1170 K. The vague superstructure in Fig. 4.4 might be an indication that the density of added rows (or steps) is not yet at the very maximum of a perfect 1×2 lattice. We did not observe the half order LEED spots of a 1×2 reconstruction, but this may very well be due to the poor quality of the LEED patterns after air exposure. Although Figs. 4.3b and 4.4 show a striking resemblance to images presented in Ref. [84] we do not think that the structures along [001] are caused by crystallographic shear plane formation (see section 3.2 and Ref. [19]). The $\{121\}$ and $\{132\}$ series of shear planes [84] do not intersect the (110) plane along [001]. Furthermore, we did not observe half steps that are usually related to the formation of crystallographic shear planes.

The final question is why we (or others) did not observe the spontaneous formation of steps before in UHV-STM experiments (Chapter 3). One important difference with the UHV experiments is that here we started every series with a completely new, stoichiometric crystal, whereas typical UHV-STM experiments are performed after a large number of sputter-anneal cycles. In that case the crystal is already reduced at the start of the measurements. A second, related difference is the roughness of the starting surface. Due to the large number of sputter-anneal cycles usually used in UHV experiments the surface becomes flatter and flatter, i.e. roughness of the polishing treatments is at least partially removed. Further-more the sputtering treatment is relatively mild, and so is the damage created by it.

Here we sputtered only once, and necessarily the surface is not as flat as it could be. Furthermore, the dose is much larger than usual. This results in larger height differences and therefore there are more steps on our surface. This may make the formation of [001] steps dominate on this surface whereas added row formation is the dominant process on a flatter surface.

4.5   Conclusions

Summarizing, we have used Atomic Force Microscopy to investigate the flattening of TiO$_2$ (110). At elevated temperatures the surface flattens, but at the same time the oxide is reduced. This has important consequences for the surface morphology. At 1135 K, first an elongated hexagonal equilibrium shape is formed, but as reduction continues the relative step free energies change and so do the shapes of the surface features. They become more and more elongated along the [001] direction. Eventually it even becomes favourable for the surface to form extra steps along the [001] direction. This causes the appearance of many narrow excursions along this direction. Ultimately this results in the 1×2 reconstruction.

At 1170 K we observe a more or less regular array of steps. Although [001] is still a preferred direction the excursions are no longer formed. Probably the surface has been reduced more strongly than at 1135 K and a 1×2 reconstruction has been formed.

The measurements described in this chapter also demonstrate that it is possible to use *ex-situ* Atomic Force Microscopy measurements to determine the surface morphology of titanium dioxide. The adsorbed water layer that is likely to be present is simply invisible to contact mode AFM. The fact that we can clearly observe large terraces in air is a strong indication that major restructuring does not take place when titanium dioxide is exposed to air at room temperature.

V

Growth of small palladium particles on TiO$_2$ (110)

We studied the thermal stability of small palladium clusters on a TiO$_2$ (110) surface. Upon heating the number of particles decreases and the average size of the particles increases. This corresponds to a decrease of palladium surface area of this model catalyst. The decrease in particle density cannot be used to distinguish between different kinds of mass transport over the surface, but on the basis of the resulting size distribution we conclude that the coalescence of diffusing particles is the main mechanism. This is supported by a direct observation of mobile clusters. During growth the palladium clusters change their shape.

5.1   Introduction

Metallic layers on oxide surfaces form a very relevant area of research in view of a number of important applications. In the semiconductor industry metallization of oxides requires the growth of uniform smooth films. In heterogeneous catalysis small particles are required with a large surface area. One of the problems encountered in catalysis is the progressive loss of active surface area due to particle growth at elevated temperatures [9]. This can clearly influence the performance of such a catalyst. Furthermore, the physical and chemical properties of small particles can be different from those of large particles and this can also influence the catalytic activity [18]. This implies that not only the preparation of these small particles, but also the stability of these particles once they are formed is very important.

A practical catalyst often consists of small particles of a catalytically active metal dispersed on a porous inert support, usually an oxide. Because of this complex geometry it is extremely hard to get detailed experimental information about for example the diffusion processes involved in the growth of the metal particles.

Therefore the use of model systems is often required. Small metal particles deposited on a flat oxide support form such a model system [20–23]. Probably the most studied model oxide surface is the TiO_2 (110) surface [19]. Other oxides, such as SiO_2 or Al_2O_3, often require the use of thin films of these oxides supported on a metal or semiconductor in order to obtain the electrical conductivity needed for most surface science techniques [21, 85]. Examples of model catalysts prepared in this way are Pd and Pt/Al_2O_3 [85], Pd/MgO [86], Pd/SiO_2, Au/TiO_2 [18] and Pd/TiO_2 [64,87–89]. Microscopic techniques like STM are clearly among the most powerful to study this kind of systems. Most of the recent STM studies have focused on the shape of the metal particles and on the nucleation behaviour. Also electron microscopy has been used to study the formation of small particles during metal deposition [22, 25] although for very small particles electron beam damage can be very important [25, 26]. Many experiments have been done on the growth or sintering of particles in real catalysts by a variety of techniques [90, 91], but the physical phenomena controlling the growth are still not very clear. Usually the growth of the average particle size can be described by a power law that describes the growth of the average radius r as a function of time t:

$$r = r_0 + k t^{1/m} \tag{5.1}$$

Conclusions about the growth mechanism are often drawn directly from the value of m. If the particles grow there has to be some kind of mass transport between the particles. In short, this transport can proceed atom by atom, in which case the atoms should be able to detach from a cluster. In this scenario clusters grow by Ostwald ripening. Alternatively, the transport can proceed cluster by cluster, provided these clusters are mobile. Growth then results from coalescence events. For Ostwald ripening $m = 3$ or $m = 4$ is expected, but in practice much higher values for m (5–11) are often found. Moreover, the value of m often decreases with increasing temperature. These higher values of m are usually ascribed to particle growth due to coalescence. In spite of the many studies devoted to this subject there is, however, still no satisfactory understanding of this ageing behaviour.

In this chapter we report an STM study of palladium on TiO_2 (110). In particular, we studied the growth and thermal stability of very small ($\approx 10\,\text{Å}$) particles. At elevated temperatures the average size of the particles grows. First we discuss our STM measurements and then we compare them with the two competing models for the surface mass transport. We find that the growth in average particle size can be described by both models, but the size distribution of the clusters strongly

suggests that cluster diffusion and coalescence are responsible for the observed particle growth.

5.2   Experimental procedures

The experiments described here were performed in the ultrahigh vacuum chamber described in Chapter 2. As was explained there the chamber has a base pressure of 1×10^{-10} mbar. The system is equipped with a system for Low Energy Electron Diffraction (LEED) and Auger Electron Spectroscopy (AES), a quadrupole mass spectrometer, and a high-speed, high-temperature Scanning Tunneling Microscope (STM) which has been described previously [35]. The sample is mounted in a molybdenum sample holder and can be heated by thermal radiation or electron bombardment from a filament.

The TiO_2 (110) crystal was cleaned by cycles of 600 eV Ar^+-ion sputtering and annealing at 950 K in UHV. Annealing the sample not only restores the surface structure after sputtering, it also causes a slight reduction of the oxide. This 'doping' of the oxide improves the electrical conductivity and is accompanied by a slight change in color of the crystal. The initially transparent crystal turns blue after many of these preparation cycles. The deviation from bulk stoichiometry is, however, still very small [76]. The contamination level was below the detection limit of AES. More details of the preparation of the TiO_2 substrate are given in Chapter 3.

Palladium was deposited with an e-beam evaporator. Deposition rate and coverage were determined with a quartz crystal oscillator which was calibrated *ex-situ* with Rutherford Backscattering Spectroscopy (RBS), as described in Chapter 2. In all measurements discussed here the total coverage was $(4.9 \pm 0.2) \times 10^{13}$ atoms/cm^2 and the deposition rate was $(3.4 \pm 0.2) \times 10^{11}$ atoms/s·cm^2. We assumed that at room temperature all the palladium atoms arriving at the oxide surface will stick. The total coverage corresponds to roughly 3% of a complete layer of close-packed palladium atoms. In order to study the effect of elevated temperatures, the sample was heated in 10-minute cycles. The 10 minutes counts the time during which the heating power was on. The temperatures mentioned are the final temperatures reached at the end of this heating. After every 10 minutes we could interrupt the particle growth, and thus follow the entire process.

All STM measurements were performed at room temperature with positive

sample bias voltages $1.5 - 2.5$ V and tunneling currents of typically 0.1 nA. The tip was electrochemically etched from a 0.25 mm tungsten wire. The sizes and positions of the clusters were determined from the STM images with the aid of the home-made cluster detection algorithm described in Chapter 2. In this procedure, we did not use the lateral dimensions of the clusters in the images, since these can easily be influenced by tip convolution effects. Even tips giving atomic resolution on a flat terrace can severely overestimate the lateral dimensions of structures with a height of more than one layer. Therefore we used the heights of the clusters, which do not suffer from these effects, as the only measure of the cluster size. This implies that in order to determine the volume of a cluster assumptions concerning the shape have to be made. For the determination of the size and spatial distributions of the clusters we always used at least several hundred clusters.

5.3   Results

5.3.1   The clean TiO$_2$ (110) surface

The morphology of the TiO$_2$ (110) surface depends strongly on preparation conditions, e.g. the annealing temperature, and on the entire preparation history. Especially the degree of bulk reduction (oxygen depletion) of the sample is an important factor [49]. Although this was already explained in Chapter 3 we will summarize some aspects here. The preparation method used in the measurements described in this chapter resulted in a surface with large terraces and a low step density, but also in a relatively large density of oxygen defects, i.e. missing oxygen atoms. These defects tend to organize themselves into short added-row structures along the [001] direction [53, 55, 70]. This is shown in Figure 5.1a. On a smaller scale, as shown in Figure 5.1b, one can see the structure of the underlying terrace. Rows are observed along the [001] direction, with a width of 6.5 Å. Also in between the added rows, on the terraces, defects are present. Since we could not detect any contamination, which could account for these defects, typically $\sim 5\%$ of a monolayer, we conclude that these are oxygen vacancies too. The appearance of both the isolated defects in the terrace and the added row structures in the STM images depends strongly on the state of the STM tip. The influence of the tip state on the appearance of oxygen defects on TiO$_2$ (110) in STM images was recently reported by Diebold *et al.* [66]. Vacancies can be imaged both as dark and as bright spots on the terrace. At lower annealing temperatures the defect density is lower

(a) (b)
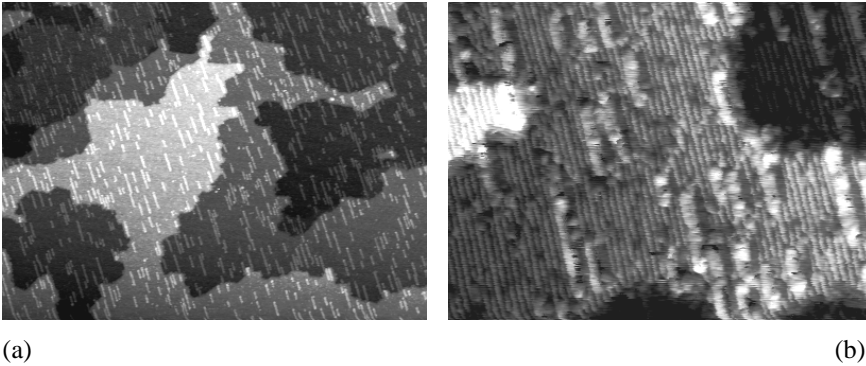
Figure 5.1: *STM images of the clean TiO$_2$ (110) surface after sputtering and annealing to 950 K. (a) Large-scale image (2220 × 1670 Å) in which one can clearly observe individual terraces, separated by single height steps (3.25 Å). The terraces are decorated by added rows along the [001] direction. These added rows, probably Ti$_2$O$_3$, are formed due to the reduction of the crystal surface, caused by the high-temperature treatment in UHV. (b) Higher magnification view (444 × 333 Å) of part of the image in (a). The anisotropic structure of the terrace is visible, as well as a few of the added rows. One can also see several dark pits in the terrace, which we ascribe to oxygen vacancies. ($V_t = +2.5$ V, $I_t = 0.03$ nA)*

in general but also the terraces on the surface are significantly smaller. Attempts to reoxidize the defects by annealing the crystal in 10^{-6} mbar O$_2$ resulted in a much rougher surface with a much higher step density due to the nucleation of new oxide terraces [71, 74, 76]. To ease the analysis we used the preparation procedure explained in section 5.2 which results in a flat substrate, but it is clear that the TiO$_2$ (110) surface is anisotropic and very inhomogeneous. Clearly the defects can strongly influence the nucleation of deposited material [92, 93].

5.3.2 TiO$_2$ supported Palladium clusters

If small amounts of palladium are deposited at room temperature on TiO$_2$ (110), small three-dimensional clusters are formed. This is shown in Figure 5.2. The clusters shown in Figure 5.2 are approximately 6 Å high. Since there is no adsorbed monolayer of palladium between the clusters and the clusters are more than one atomic layer high, this confirms the expected Volmer-Weber growth type of this system. It also indicates that the energy barrier for palladium atoms to jump from the oxide substrate on top of a palladium island, the up-step barrier, is low enough
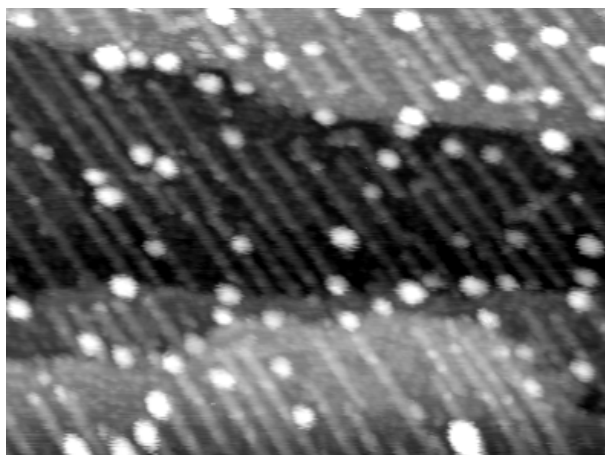
Figure 5.2: *During deposition of palladium on TiO$_2$ (110) at room temperature small 3-dimensional clusters are formed. This image (555×416 Å) was measured after deposition of 0.03 ML. On average the clusters are 6 Å high. ($V_t = +2.25$ V, $I_t = 0.03$ nA)*

to be overcome at room temperature. In Figure 5.2 it seems as if clusters have a small preference to be either at step sites or at added-row sites, but on average the clusters are distributed over the surface more or less randomly. The added-row density in Figure 5.2 is so high that it is hard to distinguish whether the clusters touch an added row by chance or by preference. In contrast to the results of Xu *et al.* [64] we did not observe a strong tendency for step decoration by the clusters. This is illustrated in Figure 5.3. An explanation for this difference might be the higher step density and palladium coverage in Ref. [64]. Also differences in the preparation of the substrate might cause differences in decoration behaviour. For example the oxygen defect concentration on our substrate may have slowed down the mobility so much that the palladium atoms or clusters were not able to reach the step edges.

After deposition at room temperature we observed that some of the clusters were mobile. Especially the smallest clusters (± 10 atoms) sometimes moved so fast that even at our maximum imaging speed of a few images per second we could not clearly resolve the motion. The larger particles however did not move at all at room temperature on the experimental timescale of 30 to 60 minutes. An example of a moving cluster is shown in Figure 5.4. On average the cluster

(a)   (b)
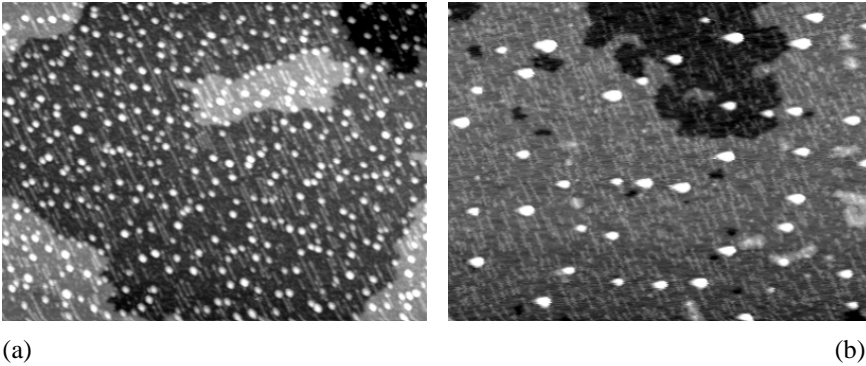
Figure 5.3: *STM images illustrating the effect of heating the sample. Before heating (a) the surface contains many small clusters. They are distributed more or less randomly, although there is a slight tendency for decoration of the steps. (b) After heating the sample to 830 K for 120 min, the cluster density has decreased and the average size of the palladium clusters has increased. We do not observe preferred positions for the clusters. Both images are 1667 × 1250 Å. ($V_t = +2.5$ V, $I_t = 0.1$ nA)*

diffusion was significantly faster along the atomic rows, the [001] direction, and defects seemed to slow down the diffusion. The number of observations of mobile clusters was insufficient for a detailed statistical analysis of the mobility. Also we have measured this only for a few different combinations of tunneling parameters and we cannot completely exclude a possible influence of the presence of the STM tip on the motion of the individual clusters.

5.3.3 Cluster growth

If the sample is heated to 830 K we observe a decrease in the cluster density and a corresponding increase in the average size. Figure 5.3 demonstrates that neither steps nor the added rows on the substrate pin the clusters completely or inhibit cluster growth. If the added rows would have blocked the diffusion the remaining cluster density would have been much higher, and if steps would pin the clusters we would have seen many more clusters at step sites. Simply by counting the number of clusters per unit area as a function of annealing time we can study the particle growth more quantitatively. The decrease in particle density at an annealing temperature of 672 K is shown in Figure 5.5. At first the cluster density decreases very rapidly, but at longer times this decrease slows down strongly. The density decrease
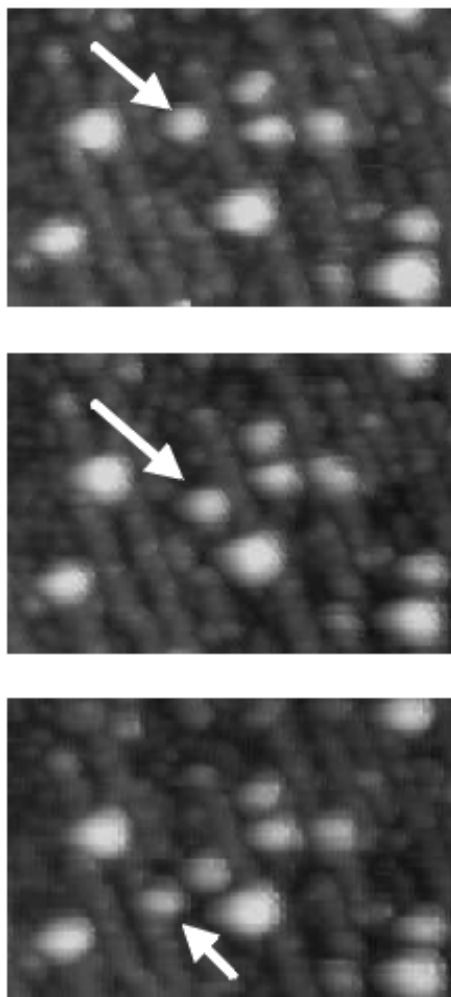
Figure 5.4: *Series of STM images (200× 134Å) showing cluster diffusion at room temperature. The time between subsequent images is 160s. In the second image one of the clusters has changed its position and in the last image a new cluster has appeared. ($V_t = +2.5$ V, $I_t = 0.05$ nA)*

can be fitted by a simple power law, $n(t) = n_0(1 + t/\tau)^{-3/m}$ with $m = 15.9 \pm 1.1$. This 'power-law-like' behaviour is very similar to what is commonly observed for the decrease in active surface area of real catalysts [91]. Figure 5.5 also shows that the average cluster height increases. As was explained in the introduction, two kinds of mass transport can be responsible for this cluster growth: atom by atom, via Ostwald ripening, or cluster by cluster, via coalescence of diffusing clusters. We will come back to this point in the next section.

Information about diffusion properties can be obtained from the spatial distribution of the clusters. In the formation of the clusters one can roughly distinguish between three regimes. During the deposition, the clusters first nucleate. Then they grow due to the imposed supersaturation. Finally, this supersaturation disappears when the deposition is stopped. In this final stage clusters continue to grow due to Ostwald ripening and/or coalescence events. The observable spatial distribution of the clusters is the result of all of these three stages, although the extent to which the final stage has progressed, of course, depends strongly on the temperature.

In general, overlapping of clusters is not possible without the merging of the clusters to a single, larger cluster. This implies a minimum center to center distance. The average nucleation distance between neighbouring clusters is expected to scale with a power of the diffusion constant of the deposited adatoms [94]. Once a cluster has nucleated, it reduces the supersaturation in its environment. As a consequence nucleation of a new cluster within a small distance from an existing one will be nearly impossible, resulting in a so-called denuded zone [95–97]. The radius of this denuded zone scales with the diffusion constant of the adatoms.

Nucleation at defects or steps can influence the cluster distance distribution. Also anisotropy in the diffusion of adatoms on the substrate will show up in the cluster separation. This may be expected when the substrate is anisotropic, as is the case for TiO_2 (110). Along the 'fast' direction clusters will nucleate further apart than along the 'slow' direction.

From the relative positions of the clusters, obtained from our STM images, we have calculated the radial distribution of the clusters, both before and after heating the sample. The result is shown in Figure 5.6. As expected, no clusters are found at very short distances (no overlap). Figure 5.6 also shows that there is no preferred distance between the clusters. The cluster density is constant at large distances.

Because of the anisotropy of the TiO_2 (110) surface we also investigated the
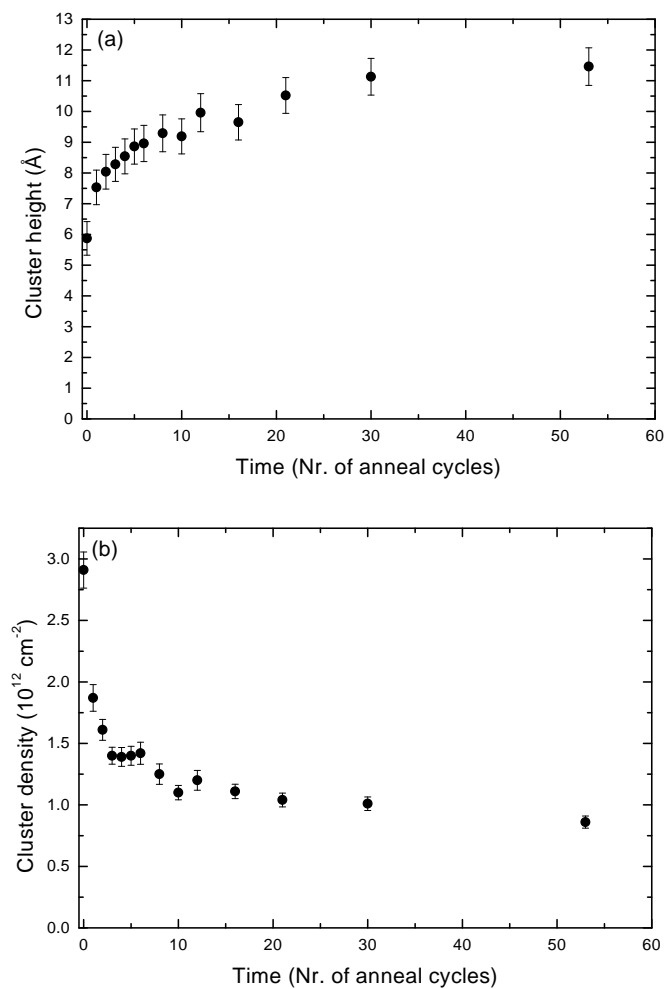
Figure 5.5: *Cluster growth as a function of heating time. The sample was heated to 672 K in 10 min cycles. During growth the average size increases (a) and the cluster density decreases (b).*
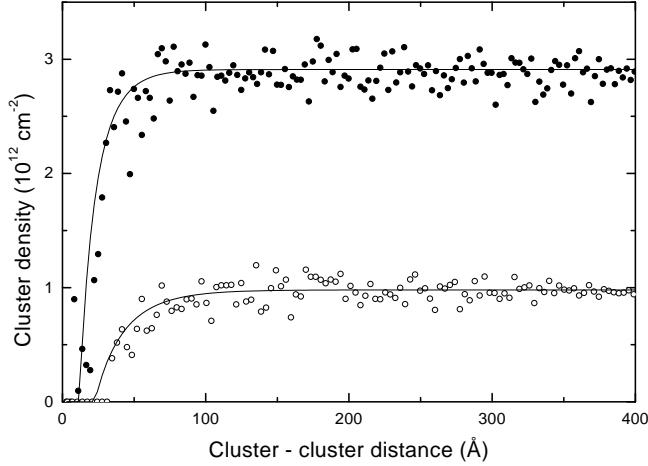
Figure 5.6: *Cluster density as a function of the distance from the center of a cluster (radial distribution function). Filled circles have been measured immediately after deposition, the open circles after annealing to 672 K for 300 min. The solid lines are given by $n(r) = n_0[1 - K_0(r\sqrt{4\pi n_0})/K_0(d\sqrt{4\pi n_0})]$, with n_0 the average cluster density and d the average cluster diameter, the average distance at which two clusters will touch (see Refs. [96,98]). K_0 is the modified zero order Bessel function.*

angular dependence of the cluster distance distribution. This, however, was not completely straightforward. Anisotropy is only expected to be noticeable in the distance between *nearest-neighbour* clusters. The probability to find clusters at large distances, will always be independent of the direction, even if diffusion is completely anisotropic. Our approach was that we constructed for every cluster a Voronoi polygon as described in Ref. [99] to determine the local environment of the cluster. If neighbouring clusters are far away, the polygon is large and if they are nearby, the polygon is small. Once the polygon is obtained, the distance from the cluster center to this polygon along a certain direction can be determined. By doing this for all the polygons, one obtains an average distance from the cluster center to the polygon edge *in this specific direction*. Repeating this procedure for a set of directions results in the average shape of all the polygons. This is plotted in Figure 5.7a. In Figure 5.7a one can see that there is a slight anisotropy in the distribution of the clusters, both before and after heating the sample. Along the [001] direction the average distance between clusters is larger than along the [1$\overline{1}$0] direction. This implies that diffusion in the [001] direction is faster. However, Figure 5.7a does

not give the magnitude of the diffusion anisotropy, but suggests a much too low value. This is caused by the use of Voronoi polygons, which employ an isotropic measure, the absolute distance between the clusters, to determine which clusters are direct neighbours and which clusters are not. The autocorrelation function of the STM images, such as shown in Figure 5.7b, suggests that the anisotropy in the distribution of the clusters is much larger than indicated in Figure 5.7a.

5.3.4 Cluster shape

In most of the images the clusters are very flat, i.e. the width of the particles is larger than the height, typically 40 Å versus 10 Å. As was mentioned in Section 5.2 this can very well be due to tip convolution. If we compare the amount of material as 'seen' in the STM images with the total amount of material deposited, as determined with the quartz crystal deposition monitor, we indeed find that there is too much material in the image. Therefore the clusters cannot be as flat as they appear to be in the images. From our images we obtain two pieces of information on the real average cluster size: the cluster density and the average cluster height (see Fig. 5.5). In Figure 5.8 we replotted the data presented in Fig. 5.5. The average number of atoms per cluster, obtained by dividing the density of deposited palladium atoms by the density of clusters, is plotted as a function of the average cluster height. We also plotted what one would expect for hemispherical particles (contact angle 90°) and spherical particles (contact angle 180°). It is clear that the particles cannot be as flat as suggested by the images. In fact the contact angle is larger than 90°, which agrees with what one would expect for a noble metal on an oxide [23]. Of course we cannot tell with this analysis whether the particles really are spherical caps as assumed here for simplicity. They could for example also be pyramids [22].

If the particle shape would remain constant during the growth process, the cluster volume, and therefore also the average number of atoms in a cluster should be proportional to h^3, where h is the average height of the particles. This is not only true for spheres or spherical caps, but for any shape that can change its size continuously. As can be seen in Figure 5.8 our data does not agree with this. This means that the shape of the clusters is changing during the growth process. The small clusters are flatter than the large clusters. Also Xu *et al.* [64] report that very small clusters at low coverages may be flatter than large clusters. However, they also report shapes which are close to hemispherical, in contrast to our conclusion

(a)

(b)
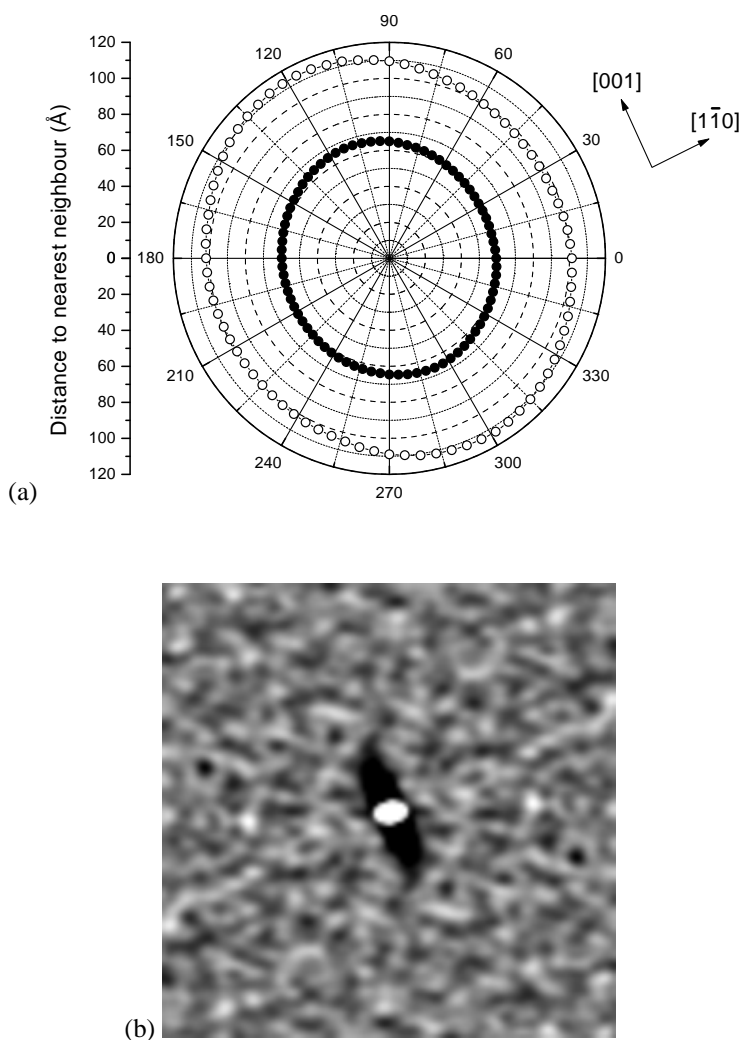
Figure 5.7: *(a) Angular dependence of the average nearest neighbour distance before and after heating (see text). Filled circles indicate the situation immediately after deposition at room temperature. Open circles have been determined after annealing to 672 K for 300 min. (b) Two dimensional autocorrelation (1000 × 1000 Å) of a STM image measured after annealing to 672 K for 300 min. The dark ellipse corresponds to the 'denuded zone'.*
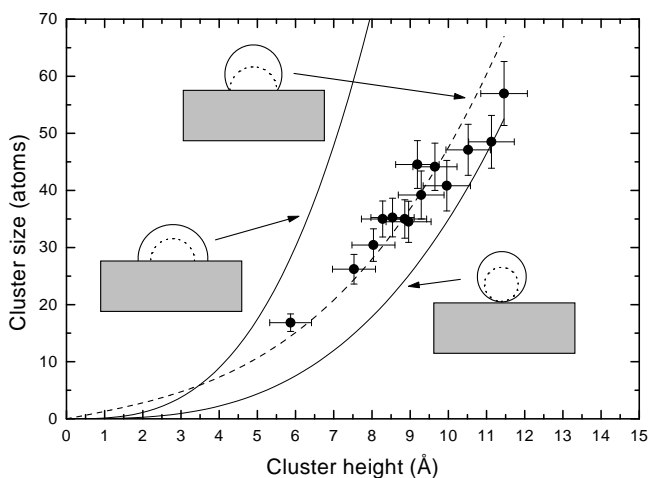
Figure 5.8: *Average cluster size, expressed as the number of palladium atoms, as a function of average cluster height. The size is obtained by dividing the density of deposited atoms by the density of clusters in the STM images. The solid curves show what would be expected for hemispherical or spherical particles. The experimental data do not follow such a simple volume~(height)^3 law, which implies that the particles change shape during the growth process. The dashed curve indicates the expected behaviour for clusters growing with a constant average contact diameter with the support of 6.9 Å.*

that the particles are closer to a spherical shape. They claim not to be bothered by tip convolution.

A possible explanation for the observed change in wetting behaviour is that the particles do not grow with a constant contact angle, but with a constant contact area with the support. This model gives a much better agreement with the data (Fig. 5.8), but we cannot exclude other shapes or growth scenarios. We can think of two reasons for a constant area of contact. First of all, the investigated clusters are very small, between 15 and 60 atoms. The contact area used to calculate the dashed line in Fig. 5.8 corresponds approximately to a compact 7-atom hexagon. It may well be that the larger clusters have reached the equilibrium shape for an infinite cluster, with the corresponding contact angle, but that the minimum contact area is simply 7 atoms, so that small clusters necessarily have a flatter shape. Second, the interaction of the clusters with the substrate is probably different at defect sites, such as oxygen vacancies. Therefore, if the clusters reside preferentially on

86

these defects, the constant contact area could correspond to the effective area of a defect site. The trend in Fig. 5.8 cannot be explained by desorption of Pd from the surface. If the amount of Pd on the surface would have decreased during the anneal periods, our analysis would have resulted in the opposite trend, i.e. towards apparently flatter particles.

5.4   Growth models

5.4.1 Ostwald ripening

A theoretical description of Ostwald ripening has been developed already a long time ago [100, 101], but for clarity we summarize the major points here. We will assume that our particles form spherical caps with a constant contact angle θ to the substrate. The average cluster size increases, driven by the system's tendency to minimize its surface free energy. The concentration of adatoms on the substrate between the clusters is responsible for the mass transport necessary for cluster growth. The growth or decay of clusters is governed by the Gibbs-Thomson effect:

$$c(r) = c_\infty \exp\left[\frac{2\gamma\Omega}{rkT}\right] \; .$$

(5.2)

The equilibrium concentration of adatoms c on the substrate close to a cluster depends on the radius of curvature r and therefore on the size of the cluster. In equation 5.2 γ is the surface free energy, which we assume to be isotropic, Ω the atomic volume in the cluster and c_∞ is the equilibrium concentration of an infinitely large cluster with a flat surface. The clusters will not have precisely equal sizes. The larger ones have a lower equilibrium adatom concentration, and the smaller ones have a higher equilibrium adatom concentration. This causes the small clusters to shrink and the large ones to grow.

If we assume that mass transport takes place via surface diffusion and that this diffusion is the rate limiting step, then the gradients in the adatom density between the clusters will determine the rate of the mass transport according to Fick's law. The flux of atoms per unit length, j into or away from the cluster is given by

$$j = -D^{Pd}_{TiO_2} \nabla c \; ,$$

(5.3)

in which $D^{Pd}_{TiO_2}$ is the diffusion constant of the adatoms on the substrate. In order to calculate the gradient in the adatom concentration at the interface with the cluster

usually a mean-field approach is used. This implies solving the radial form of Fick's law, with the boundary conditions that the concentration at the interface with the cluster is given by Eq. 5.2 and the concentration 'far away' from the cluster is equal to the average concentration $\bar{c}$. Since in two dimensions the radial solution of Fick's law diverges, this 'far away' cannot be infinitely far away. Therefore a dimensionless screening factor l is introduced such that at a distance $l \times r$ from the center of the cluster the concentration reaches its far field value $\bar{c}$. This screening factor is assumed to be constant[1]. The rate of growth of a cluster of size r is then given by [101, 102]

$$\frac{dr}{dt} = \frac{\Omega D_{TiO_2}^{Pd}}{2\,\alpha_V(\theta)\ln l} \frac{1}{r^2} \left[\bar{c} - c(r)\right] . \tag{5.4}$$

Here, $c(r)$ is the equilibrium concentration of the cluster as given by equation 5.2 and $\alpha_V(\theta)$ is a geometrical factor which is used to account for the volume of a spherical cap [101].

The cluster size distribution f has to obey a continuity equation

$$\frac{\partial f(r,t)}{\partial t} = -\frac{\partial}{\partial r}\left(f(r,t)\frac{dr}{dt}\right) , \tag{5.5}$$

and the average concentration $\bar{c}$ is determined with the condition that there is mass-conservation in the system:

$$\int_0^\infty f(r,t)r^3\,\mathrm{d}r = constant . \tag{5.6}$$

The most common way to solve this problem is to assume that for the majority of clusters the radius of curvature is large. The exponential in the Gibbs-Thomson equation can then be approximated by $e^x \approx 1+x$:

$$c(r) = c_\infty \left[1 + \frac{2\gamma\Omega}{rkT}\right] . \tag{5.7}$$

With this assumption one can show that the average radius r will grow, and the cluster density n will decrease according to universal power laws:

$$\begin{aligned}
\bar{r}(t) &= \bar{r}(0)\left(1+\frac{t}{\tau}\right)^{1/4} , \\
n(t) &= n(0)\left(1+\frac{t}{\tau}\right)^{-3/4} .
\end{aligned} \tag{5.8}$$

---

1. This problem can also be solved self-consistently without the introduction of the screening factor l [98]. Strictly speaking l is *not* constant but depends on cluster size and density. However, in our case $\ln l$ is always between 1 and 3 and therefore it can safely be assumed to be constant in Eq. 5.4.

This situation corresponds to $m = 4$ in equation 5.1. It also results in so-called scaling behaviour. In the course of time the total number of clusters will decrease and the average size will increase, but the shape of the cluster size distribution will not change [101].

However, in our case we are dealing with very small particles and therefore the approximation leading to Eq. 5.7 does not necessarily hold. Therefore we will use Eq. 5.2 and the evolution of the cluster density and the size distribution will be calculated numerically by solving Eq. 5.5.

5.4.2 Cluster diffusion

As was mentioned in the introduction, clusters can also grow via a sequence of coalescence events. This requires the clusters to be mobile. The key element in this model is the cluster diffusion constant and, in particular, its size dependence. This size dependence will be determined by the actual mechanism responsible for the motion of the cluster. We assume that the 3-dimensional clusters move due to the random diffusion of the palladium adatoms on the surface of the clusters. A jump of an adatom will result in a small shift in the center of mass of the cluster, and therefore many of these jumps make the cluster diffuse. Our treatment of this motion is similar to that by Morgenstern *et al.* [103] and Khare *et al.* [104] of the motion of two-dimensional vacancy islands on Ag(111). If n adatoms jump ν times per second over a distance a, the center of mass of a cluster of s atoms jumps $n\nu$ times per second over a distance a/s. The diffusion constant D_{Pd}^{Pd} of the adatoms over the surface of the cluster is given by νa^2, and for the cluster diffusion constant D_c it follows that $D_c = D_{Pd}^{Pd} n/s^2$. However, on the surface of a hemispherical cluster not all jumps of the adatoms are parallel to the substrate, and the component of the jumps perpendicular to the substrate surface does not contribute to a lateral displacement of the center of mass of the cluster. Taking this into account, and integrating over the surface of the cluster we find for a hemispherical cluster

$$D_c(r) = \frac{3\Omega^2 \rho D_{Pd}^{Pd}}{\pi r^4} \,.$$
(5.9)

In this equation ρ is the adatom density on the surface of the cluster. This $\frac{1}{r^4}$ dependence is consistent with a result obtained for the diffusion of pores in solids [105]. Although ρ is the adatom density on the surface of the *cluster* and not on the *substrate* it depends in the same way on the radius of curvature of the cluster. With ρ_∞

as the adatom density on a flat surface we get:

$$\rho(r) = \rho_\infty \exp\left[\frac{2\gamma\Omega}{rkT}\right] . \tag{5.10}$$

If we use this dependence (Eqs. 5.9 and 5.10) of the diffusion constant on the size we can calculate the decrease in cluster density from the frequency of binary collisions. Collisions between clusters of volume s' and $s - s'$ result in an increase in the number of metal clusters of size s, and collisions between a cluster of size s with any other cluster will result in a decrease in the number of clusters with size s [106, 107]. This can be written as[2]:

$$\frac{\partial f(s,t)}{\partial t} = \int_0^s D_c(s') f(s',t) f(s-s',t)\, ds'$$
$$- \int_0^\infty \left[D_c(s) + D_c(s')\right] f(s,t) f(s',t)\, ds' . \tag{5.11}$$

With this equation it is possible to calculate the evolution of the cluster density and the size distribution similar to the calculation for Ostwald ripening. We assume our particles to be hemispherical, and therefore $s = \frac{2}{3}\pi r^3$. If the adatom concentration ρ is independent of r, i.e. r is large, the average cluster size will grow and the cluster density will decrease according to the following power laws [108]:

$$\begin{aligned}
\bar{r}(t) &= \bar{r}(0)\left(1 + \frac{t}{\tau}\right)^{1/7} , \\
n(t) &= n(0)\left(1 + \frac{t}{\tau}\right)^{-3/7} .
\end{aligned} \tag{5.12}$$

Also in this case scaling behaviour is expected [106], but the shape of the size distribution will be different from that for Ostwald ripening. Therefore the size distribution may be the tool to distinguish between the two scenarios.

5.4.3 Comparison with experiment

First we consider the Ostwald ripening scenario. If we compare our measurements with the commonly expected universal power law (Eq. 5.8) we do not find good agreement, even with optimized values for the constants in the model (Fig. 5.9). This was to be expected, since our particles are very small, $r \sim 10\,\text{Å}$. If we use the surface tension of liquid palladium, $1.5\,\text{J/m}^2$, and take Ω from the bulk density of

----

2. Here the capture numbers [98] are assumed to be constant and equal to 1. In reality they vary slowly with cluster size and are between 2 and 5.

palladium, $14.7\,\text{Å}^3$, we find that the approximation leading to equations 5.7 and 5.8 is wrong by more than an order of magnitude! When we use equation 5.2 instead and solve 5.5 numerically, we find a very good agreement with our measurement as is shown by the dashed curve in Figure 5.9. In the calculations we assumed all particles to be hemispherical, and assumed all the 'action' to be happening during the time the heating power is on, i.e. the time related to one anneal cycle is taken to be 10 min. The product $c_\infty D_{TiO_2}^{Pd}$ is the only free fitting parameter, and the best fit was obtained for $c_\infty D_{TiO_2}^{Pd} = (1.5 \pm 0.5) \times 10^{-7}\,\text{Hz}$. In fact the error made by using approximation 5.7 was much bigger than suggested by the solid curve in Fig. 5.9, because completely different values for the parameters $(c_\infty D_{TiO_2}^{Pd})$ had to be used. If we use the values which give good agreement for equation 5.2, and substitute them in equation 5.7, we see a much larger discrepancy as is also shown in Figure 5.9. This implies that for such small particles care should be taken when conclusions on the diffusion mechanism are based on the power law found. In fact, strictly speaking the particles do not grow according to a power law, but over a limited size range one can always fit a power law. However, the exponent of that power law will depend on the particle size.

We can also compare the data with our coalescence model, by using equations 5.9 and 5.11. With these equations we again calculate the decrease in cluster density as a function of time. As can be seen in Figure 5.9 this fits our data very well. Also in this case we used the surface tension of liquid palladium and the known bulk density in the calculation. The best fit was obtained for $\rho_\infty D_{Pd}^{Pd} = (4 \pm 1) \times 10^{-4}\,\text{Hz}$. Since both the models agree with our measurements of the growth of the particles we cannot distinguish between the two cases on the basis of these measurements and fits alone. In both models the values obtained for the rate constants, i.e. $c_\infty D_{TiO_2}^{Pd}$ for Ostwald ripening and $\rho_\infty D_{Pd}^{Pd}$ for coalescence growth, seem very low. In the next chapter we will show that the rate constants can be very strongly affected (lowered) by the defects in the substrate.

Further information is obtained by evaluating the size distribution of the clusters, both before and after heating of the sample. The result is shown as the columns in Figure 5.10. In this analysis we have assumed that the clusters are hemispherical.

As was mentioned before, equations 5.5 and 5.11 not only allow for a calculation of the total cluster density, but also for a calculation of the size distribution of the clusters. The results for both models were scaled with the same total cluster
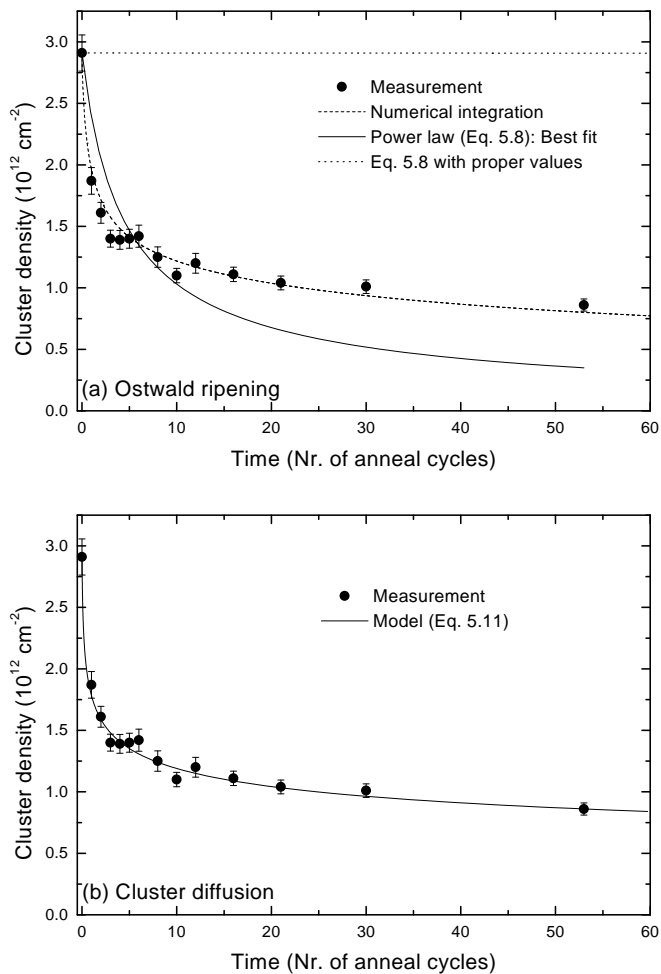
Figure 5.9: *Measured decrease in cluster density as a function of time at 672 K (cf. Fig. 5.5) and a comparison with the two models. (a) Ostwald ripening. The solid curve is the best fit with equation 5.8. Better agreement is obtained when equation 5.2 is not approximated by Eq. 5.7 (dashed curve). The dotted curve is obtained when we re-evaluate Eq. 5.8 for the best fit parameter values obtained from the dashed curve. (b) Best fit obtained with our model of diffusion and coalescence of clusters (Eq. 5.11).*
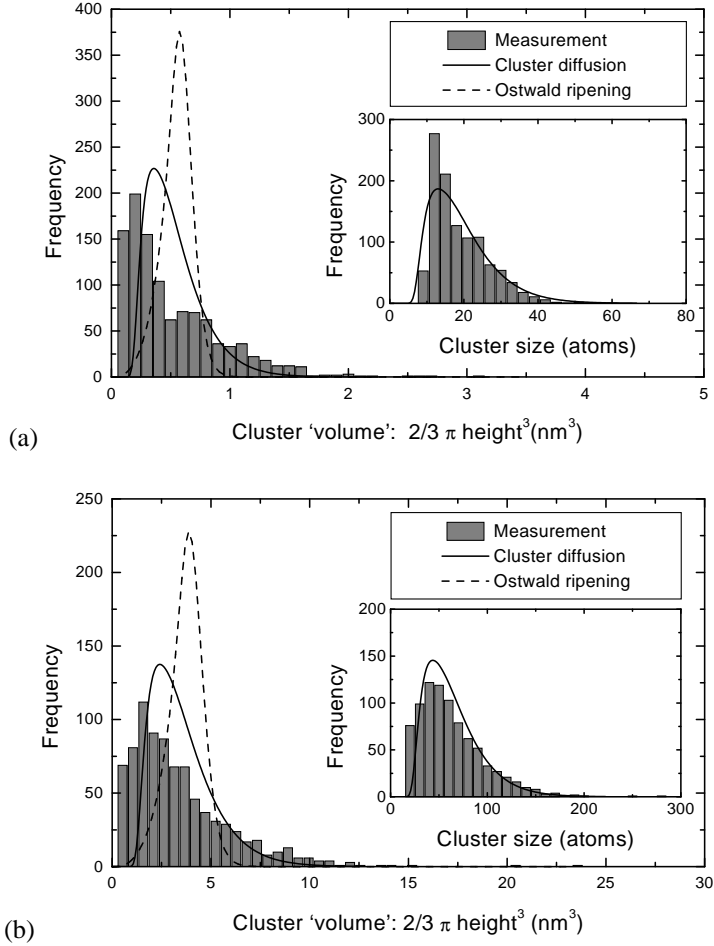
Figure 5.10: *Size distribution of the clusters (a) after deposition at room temperature and (b) after annealing to 672 K for 300 min. Clusters are assumed to be hemispherical and a comparison is made with the predictions for the two different growth models. The dashed curve is the predicted size distribution for Ostwald ripening and the solid line is the prediction for coalescence of diffusing clusters. In both cases the total cluster density and average cluster size were fixed to the experimental values. In the two insets the cluster sizes have been determined according to the data in Figure 5.8 in order to correct for the change in cluster shape. This improves the agreement with the cluster diffusion model considerably.*

density and average size as the measurement and are compared with our data in Figure 5.10. The calculated size distributions do not depend on the growth rate and thus involve no fitting parameters. Both before and after heating the observed size distribution deviates considerably from the theoretical distribution for Ostwald ripening. The theoretical size distribution for coalescence of diffusing clusters fits the observed distribution better. The remaining deviation occurs for small clusters, especially for the distribution obtained immediately after deposition, before heating.

The most obvious reason for this deviation is the change in cluster shape, described in Section 5.3.4. Since the small particles are flatter, their radius of curvature will be larger than assumed in the model, and hence they will be slower. If we convert the measured height of each cluster into the clusters volume according to the data shown in Figure 5.8, we see that indeed the agreement with the calculated curve for coalescence growth improves considerably. This is shown in the two insets in Figure 5.10. Since both before and after heating the size distribution matches the one expected for coalescence growth we conclude that this mechanism has also been responsible for the formation of the clusters observed at room temperature, before annealing.

Another possible cause for the discrepancy between the calculated and measured size distributions is pinning of a fraction of the clusters. This could cause some small clusters to disappear more slowly.

5.5 Discussion

In this paper we have presented our observations of the growth of palladium clusters on TiO$_2$ (110) and have tested two models to explain the growth: Ostwald ripening versus cluster diffusion and coalescence. We conclude from the size distribution of the clusters that cluster diffusion and coalescence forms the dominant growth mechanism. Stone *et al.* [89] have come to the same conclusion for this system. They based their conclusion mainly on the shape of a few of the particles and on the absence of small clusters, which they had expected in the case of Ostwald ripening, since small particles are continually produced in that case. The latter argument is questionable, as can be seen from the calculated curves in Figure 5.10. For both models the density of small particles is very low. The reason for this is simple. Even though small particles are produced during all stages of Ostwald

ripening, they disappear faster and faster, resulting in a progressive decrease in their concentration.

We have seen that an analysis of the growth mechanism based solely on the power law with which the particles grow can be completely inconclusive. This is evident from the fact that both models can fully explain the rate of cluster growth. Furthermore there is no easy interpretation of the growth exponent. A growth exponent for Ostwald ripening of $m = 4$ is only expected for relatively large particles, for which equation 5.7 holds. Small particles naturally result in higher values of m. The same is true for our model for the diffusion of the clusters. Therefore the wide scatter in the values for m observed for practical catalysts is really no surprise. Also the general trend that higher temperatures lead to lower values of m can be explained in terms of particle sizes. At higher temperatures the average particle size is larger and therefore m will be lower (closer to 7 or 4).

The models used here contain several assumptions. The mean-field description only holds if the clusters do not cover more than a small fraction of the surface. In our case the total coverage is only 3% and since the palladium forms 3D particles, the areal coverage is even lower.

The mean-field approach completely ignores local effects. However, local variations can be important in Ostwald ripening [65, 99, 109–111]. Clusters 'feel' the adatom concentration due to their direct neighbours rather than the average over the entire surface. This effect effect broadens the size distribution [112] which would slightly improve the agreement between the calculation for Ostwald ripening and the experimental data.

We have made several direct observations of small mobile clusters at room temperature, but it is difficult to completely rule out a possible influence of the STM tip. We note that the shapes of the size distributions and spatial distributions of the clusters before and after heating of the sample are very similar. It therefore seems likely that the configurations before and after annealing both resulted from the same growth mechanism. This implies that already before the first measurements, i.e. during and immediately after deposition, many coalescence events must have occurred. Otherwise a size distribution typical for nucleation would have been observed. The anisotropy in the spatial distribution of the clusters indicates that the clusters move faster along the [001] direction than along the [1$\bar{1}$0] direction. Due to the coalescence events, the probability of finding clusters very close together is smaller than finding clusters far away. The distance over which this effect is important depends on the diffusion constant of the particles, and there-

fore an anisotropy in the diffusion causes an anisotropy in the distribution of the particles on the surface.

The TiO$_2$ surface contains a high density of defects, the oxygen vacancies. These defects may be expected to influence the nucleation and diffusion process. If clusters would nucleate preferentially at defect sites and stay there, their spatial distribution would directly reflect the spatial distribution of these defects. However, the observed cluster density is much lower than the defect concentration. In addition we see that the cluster density decreases with time and that this decrease proceeds similarly, albeit at different rates, at different temperatures. From this we conclude that the defects can at most modify the *magnitudes* of the diffusion constants, but that the growth mechanism is not affected. In the following chapter we will report on this in more detail and we will show that the growth rate indeed does depend on the defect concentration [113].

5.6   Conclusions

We have used STM to follow the growth of palladium clusters on TiO$_2$ (110) at 672 K. We find that the observed growth law and particle size distribution are well reproduced by a model based on Pd adatom induced mobility of palladium clusters and cluster coalescence. Surprisingly, our mean-field type theory works well even though the surface is far from homogeneous; it contains non-stoichiometric added rows and oxygen vacancies. Our study shows that, in spite of what seems to be common practice in the analysis of practical catalysts, the particle growth cannot be modelled by a single, universal power law, with a straightforward interpretation of the growth exponent. The approximation leading to such laws bitterly fails for small particles, which makes the exponent a strong function of the average particle size. After a proper treatment of this effect, we find that it is not possible to distinguish Ostwald ripening from cluster diffusion and coalescence on the basis of the measured growth law of the average particle size. Based on the particle size distribution we conclude that cluster diffusion and coalescence form the dominant growth mechanism for palladium clusters on TiO$_2$ (110). This conclusion is supported by direct observations of mobile clusters at room temperature. The spatial distribution of clusters shows that their diffusion is faster along the [001] direction than along the [1$\bar{1}$0] direction. Finally we observe a gradual change in the wetting of the palladium clusters on the TiO$_2$ substrate during the growth; small clusters are flatter than large clusters.

VI

The influence of substrate defects on the growth rate of palladium nanoparticles on a TiO$_2$ (110) surface

We investigated the growth rate of small palladium particles on TiO$_2$ (110) substrates with high and modest defect concentrations, using Scanning Tunneling Microscopy (STM). The defects on the substrate surface are created as a consequence of reduction of the oxide crystal in ultra-high vacuum (UHV). The level of oxygen depletion depends on the preparation conditions, resulting in either a strongly reduced surface with a high level of oxygen depletion, or a mildly reduced surface with a modest level of oxygen depletion. After deposition of palladium at room temperature on a mildly reduced titania surface, palladium clusters predominantly cover steps. On a strongly reduced sample, clusters are smaller and distributed over the terraces. At elevated temperatures the particles grow in both cases, but the growth rate on the mildly reduced surface is higher than on the strongly reduced surface. Finally, on a mildly reduced substrate the particles are flatter than on a strongly reduced substrate.

6.1   Introduction

Growth or sintering of small supported metal particles is of great importance in several practical settings, such as heterogeneous catalysis. Particle growth leads to a decrease in active surface area and can therefore lead to a decrease in activity of a catalyst [90, 91]. Unfortunately, information about the factors controlling the growth rate is still rather limited. This is mainly caused by the complex structure and composition of catalysts and the difficulty to measure the surface evolution under operating conditions, i.e. high temperatures and high pressures.

Some of these problems can be avoided by using model systems [20–23]. With such a model system individual factors which can influence the growth rate such as temperature and atmosphere can be studied independently. In Chapter 5 we have investigated the growth of small palladium particles on TiO_2 (110) using Scanning Tunneling Microscopy (STM) [114]. At elevated temperatures the particles grow. A comparison between the observed growth rate and particle size distributions and model predictions for ripening and coalescence growth revealed that the palladium particles are mobile and grow due to coalescence. In this chapter we investigate the influence of the defect density of the titania support on the rate of particle growth. In particular we compare the growth rate of palladium particles on a mildly reduced titania substrate with the growth rate on a strongly reduced substrate. Since defects usually play an important role in the nucleation of metals on insulators by limiting the diffusion of the deposited atoms [92,93], they are also likely to influence the diffusion and therefore the coalescence rate of small clusters of atoms.

6.2   Experimental procedures

Our experiments were performed in a UHV set-up with a base pressure of 1×10^{-10} mbar (see Chapter 2). A $1 \times 1 \, cm^2$ polished TiO_2 single crystal [61] with (110) surface orientation was mounted in a molybdenum holder which could be heated by thermal radiation and electron bombardment from a tungsten filament. As described in Chapter 3, it is still only partly understood how to prepare TiO_2 (110) surfaces with a controlled defect density [49,66,70,71,76]. The defect density depends e.g. on annealing time and temperature and on exposure to oxygen, but also on the history of the sample. We used two different recipes to clean and prepare our sample. In the first recipe we used several cycles of 30 min Ar^+-ion sputtering with an energy of 600 eV and a net current on the sample of $1 \, \mu A/cm^2$, followed by 20 min annealing to 950 K. In the second recipe we used cycles of 30 min sputtering and 10 min annealing to 920 K. In both cases the contamination level was below the detection limit of Auger Electron Spectroscopy (AES) and the sample showed a 1×1 LEED pattern. Both preparation procedures resulted in a blue sample, indicating a mild reduction of the bulk of the crystal.

Palladium was deposited from an e-beam evaporator. The amount of material deposited was measured with a Quartz Crystal Microbalance thickness moni-

tor. This thickness monitor was calibrated by deposition of Pd on a Si substrate and subsequent measurement of the deposited amount *ex-situ* with Rutherford Backscattering Spectroscopy (RBS), as described in Chapter 2. The depositions were performed at room temperature at a rate of $(3.4 \pm 0.2) \times 10^{11}$ atoms/s·cm^2, in each case to a total coverage of $(4.9 \pm 0.2) \times 10^{13}$ atoms/cm^2. We assumed all deposited palladium atoms to stick to the surface.

6.3   Results

Both preparation procedures for the TiO$_2$ crystal usually result in a surface with large terraces. However, these terraces are depleted in oxygen, which leads to specific defects. As shown in Chapter 3, the terraces contain isolated oxygen vacancies, but the oxygen vacancies also organize into added row structures [52, 53, 66, 70, 71, 76]. This is illustrated in Figure 6.1. The added rows are thought to have a Ti$_2$O$_3$ or Ti$_3$O$_5$ composition [52, 70, 71]. We find that the first preparation procedure (30 min sputtering and 20 min annealing to 950 K), results in a surface with a much higher density of added rows than the second procedure (30 min sputtering and 10 min annealing to 920 K), although sample history definitely plays a role too. We will refer to the substrates obtained in these two cases as the strongly reduced sample, with many added rows, and the mildly reduced sample, with just a few added rows. The difference in both the number and the total length of the rows is about a factor 13. The average length of the rows is similar in both cases, namely $\sim$ 50 Å.

In order to study the effect of the degree of reduction of the TiO$_2$ (110) surface on the growth of palladium particles we deposited precisely the same amount of material on both substrates. The data for the 'strongly' reduced surface have been published before in Ref. [114], and were described in Chapter 5. In Figure 6.2 we show STM images of the two surfaces immediately after deposition. On the strongly reduced substrate the cluster density is much higher than on the mildly reduced surface. On the mildly reduced surface we clearly see decoration of substrate steps ($\sim$ 45 % of the clusters is located at step sites) whereas on the strongly reduced substrate the clusters are distributed over the terraces and only a very small fraction of the clusters is at the steps. This behaviour can be explained by a difference in the diffusion coefficient of Pd on the two surfaces. Although there is just a modest degree of step decoration on the 'strongly' reduced surface, step deco-
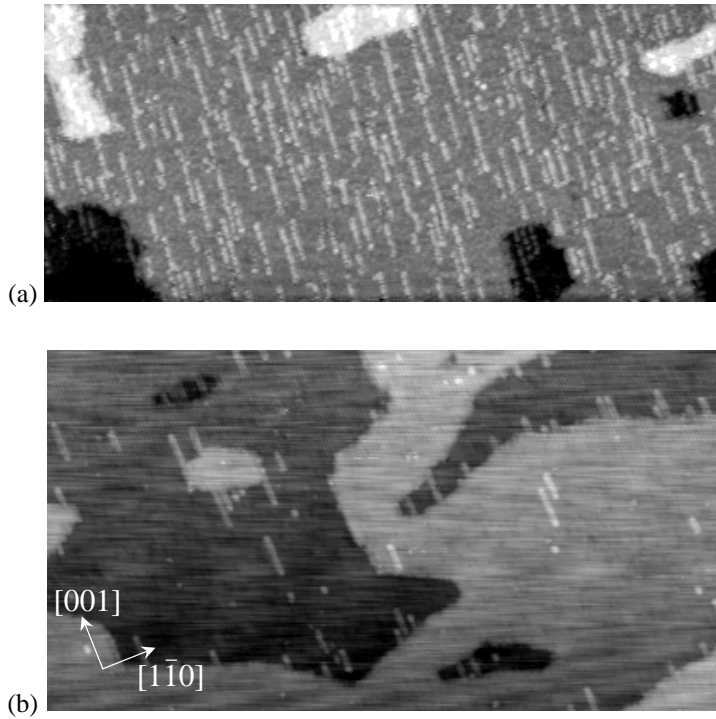
Figure 6.1: *STM images of the TiO$_2$ (110) substrate. (a) Strongly reduced surface (1110 Å × 484 Å, V$_t$ = +2.50 V, I$_t$ = 0.05 nA). The image was measured in 80 s. (b) Mildly reduced surface (1110 Å × 590 Å, V$_t$ = +2.27 V, I$_t$ = 0.05 nA). The image was measured in 130 s. In both images one can observe several terraces separated by single height steps (3.25 Å). In both images the terraces are decorated by added rows along the [001] direction, but the density of these rows is much higher on the strongly reduced surface than on the mildly reduced surface.*

ration does occur in both cases. The steps clearly act as 'sinks' for the palladium atoms or clusters. However, on the strongly reduced surface the mobility of the palladium is so low that it cannot reach the step. A lower diffusion coefficient also results in a higher density of nuclei [94]. Therefore a reduced mobility explains both the higher cluster density and the smaller amount of material accumulated at steps on the strongly reduced sample. We note that the clusters on the terraces seem to have a preference for residing at the end points of added rows.

Since tip convolution might strongly influence the apparent lateral size of the clusters in the STM images, the height of the clusters with respect to the terrace is the only reliable measure of the size of the clusters. Therefore, it is hard to determine the size of the clusters at the steps very accurately. Nevertheless, the estimates we obtain for the sizes of the clusters at the steps do not deviate significantly from the sizes of the clusters on the terrace.

From STM images like Figure 6.2b one can see that the cluster density is much higher at the steps than on the terrace. The combination of a high cluster density at the steps with a non-reduced average cluster size at the steps can be explained as follows. The steps act as nucleation sites for new clusters or as binding sites for diffusing clusters. Pd atoms and clusters predominantly diffuse along the [001] direction. Also diffusion of clusters at the steps is not allowed perpendicular to the [001] direction. Within this simple description, the combination of nucleation and growth of the clusters, and the step nucleation or sticking reduce to a one-dimensional problem, with each channel along the [001] direction behaving virtually independently from the neighbouring channels. Our earlier analysis of the spatial distribution and the motion of Pd clusters on the strongly reduced titania substrate confirms the high degree of one-dimensionality of the Pd diffusion [114]. The frizzy appearance of most clusters in Fig. 6.2b reflects the continual motion and/or shape fluctuations of these clusters during the time necessary to record the image [115]. We cannot exclude a possible influence of the STM tip on the motion completely, but none of our tests indicated such an influence. The particles move preferably along the [001] direction of the substrate, and the motion is independent of the STM's scanning speed and scanning direction. In order to minimize potential interactions between tip and surface, we measured most of our images with low tunneling currents ($\leq 0.1\,$nA) and bias voltages between 2 and 3 V. An additional piece of evidence for the strongly one-dimensional motion is the variation of the step cluster density with step orientation. On the mildly reduced surface the

(a)

(b)
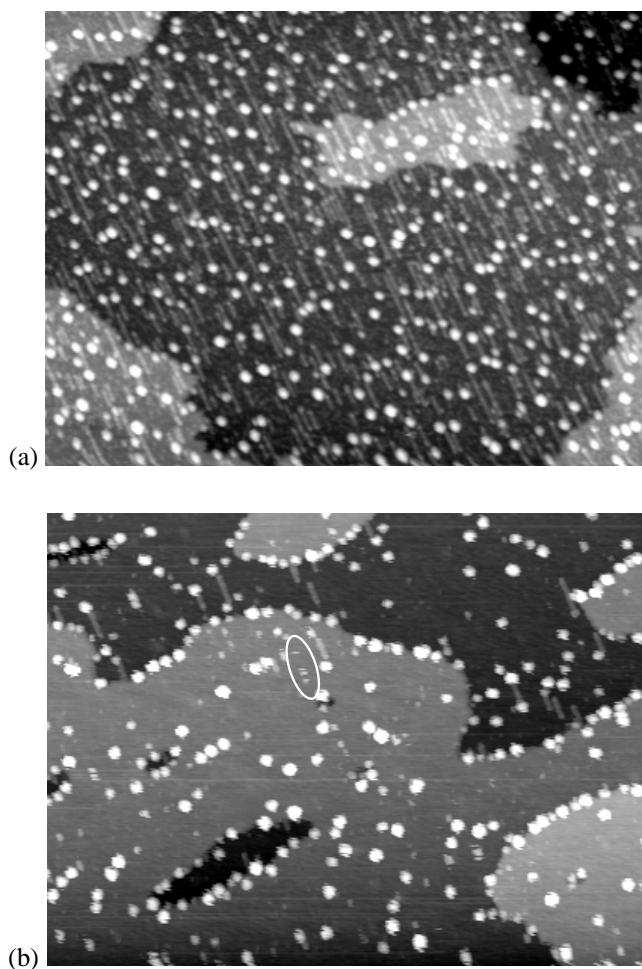
Figure 6.2: *STM images after deposition at room temperature of 0.03 ML palladium on (a) a strongly reduced titania surface ($V_t = +2.50\,V$, $I_t = 0.1\,nA$, measured in 125 s) and (b) a mildly reduced titania surface ($V_t = +2.50\,V$, $I_t = 0.1\,nA$, measured in 240 s). Both images are $1667\,\text{Å} \times 1250\,\text{Å}$. In both cases small 3-dimensional clusters are formed. On the strongly reduced surface the clusters are distributed over the terraces and just a few clusters are found at step sites. On the mildly reduced surface the cluster density is much lower and a large fraction of the clusters is positioned at step sites, mainly at steps running perpendicular to the [001] direction. The ellipse indicates one of the mobile clusters in the image [115].*

cluster density is very high at steps running perpendicular to the [001] direction, whereas the cluster density is lower at steps running parallel to the [001] direction. Similar conclusions can be drawn from the observations by Xu *et al.* [64].

In order to study the growth rate of the particles we annealed both samples to $672\,\mathrm{K}$ in cycles of $10\,\mathrm{min}$, followed by cooling to room temperature. In Figure 6.3 characteristic images of the strongly reduced surface after 21 heating cycles (Fig. 6.3a) and the mildly reduced surface after 9 heating cycles (Fig. 6.3b) are shown. On both surfaces the particles grow and the particle density decreases. At all times the particle density remains lower on the mildly reduced surface. On the strongly reduced surface the clusters are still distributed over the terraces. On the mildly reduced surface we still find many clusters at step edges, but there is also still a substantial number of clusters present on the terraces. Similar to the situation after deposition at room temperature the clusters at the steps are neither bigger nor smaller than the clusters on the terrace and the clusters have a preference for steps running perpendicular to the [001] direction.

One might have expected the clusters on the terrace to have diffused to steps and become stuck there. This would have resulted in a situation with all the clusters at step edges. This is not the case. This means either that not all clusters have reached the step, or that clusters can detach from steps at $672\,\mathrm{K}$. Inspection of Figure 6.3b reveals that even though the cluster density is a lot lower than on the strongly reduced surface (Fig. 6.3a), the average distance between the clusters is still significantly smaller than the average distance from a cluster to the nearest step. Therefore it is very likely that most clusters experience one or more coalescence events on the terrace, before reaching the step. Since the mobility of the clusters depends very strongly on the size of the clusters [114], the coalesced clusters have probably been too slow to reach the step during the 9 annealing cycles, even at $672\,\mathrm{K}$.

In Figure 6.4 the decrease in cluster density as a function of time is shown for both cases, the strongly reduced and the mildly reduced surface. One can see that on the mildly reduced surface the cluster density is not only lower, which corresponds to a larger average cluster size, but also levels off earlier. This corresponds to what one would expect if the process proceeds faster than on the strongly reduced surface. The solid lines in Figure 6.4 have been calculated with the model for coalescence growth introduced in Chapter 5 [114]. In this model it is assumed that a cluster moves as a consequence of the random motion of the adatoms on its
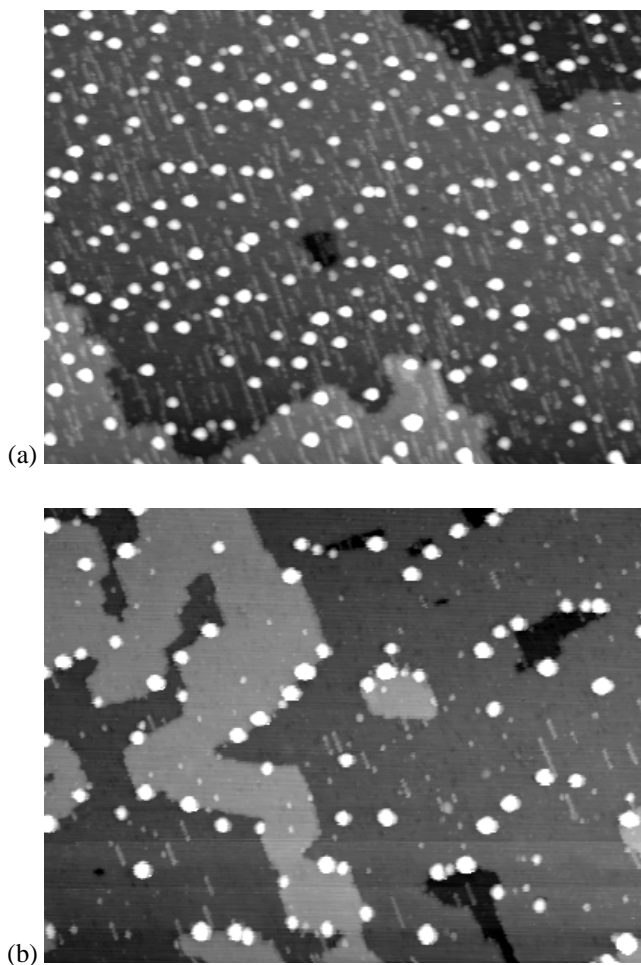
Figure 6.3: *STM images of 0.03 ML palladium on TiO$_2$ (110) after heating to 672 K. (a) Strongly reduced titania substrate, heated for 21 × 10 minutes (V$_t$ = +2.55 V, I$_t$ = 0.1 nA) (b) Mildly reduced titania substrate, heated for 9 × 10 minutes (V$_t$ = +3.24 V, I$_t$ = 0.15 nA). Both images are 1667 Å × 1250 Å. In both cases the average cluster size increases and the cluster density decreases upon heating. The images were measured in (a) 240 s and (b) 125 s.*
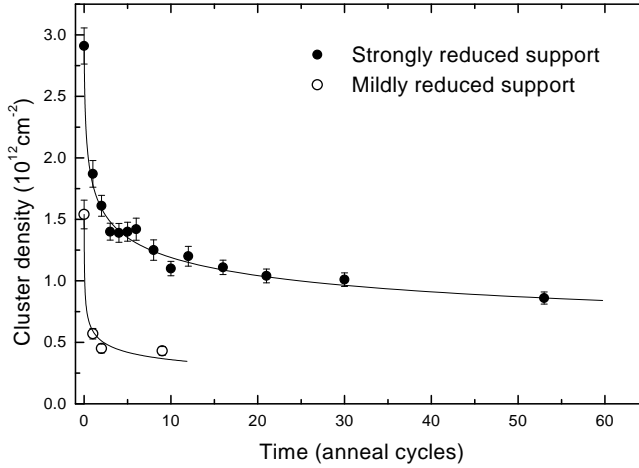
Figure 6.4: *Decrease in cluster density as a function of annealing time (10 min/cycle) at 672 K. On the mildly reduced surface (open circles) the cluster density is not only lower, but also decreases faster than on the strongly reduced surface (solid circles). The solid lines are calculated with our model for cluster growth by binary collisions of diffusing clusters (Eqs. 6.1 and 6.2) with $\kappa\rho_\infty D_{Pd}^{Pd}$ values of 1.5×10^{-1} Hz and 4×10^{-4} Hz respectively (see Section 6.3).*

own surface. The diffusion constant D_c of a hemispherical cluster with radius r is then given by [105, 114]:

$$D_c(r) = \frac{3\Omega^2}{\pi r^4}\rho_\infty D_{Pd}^{Pd}\exp\left[\frac{2\gamma\Omega}{rkT}\right] \ . \tag{6.1}$$

Here, Ω is the volume per atom in the cluster, for palladium this is $14.7\,\text{Å}^3$. Furthermore, k is Boltzmann's constant, T refers to temperature and γ denotes the surface free energy, which we will assume to be equal to the surface free energy of liquid palladium: $1.5\,\text{J/m}^2$ [23, 116]. The surface free energy of liquid metals is generally lower than that of solid metals, but independent of orientation. Usually, it stays within roughly 20% of the surface free energy of the solid [117]. Finally, D_{Pd}^{Pd} is the diffusion constant of a single palladium atom on a palladium surface and ρ_∞ is the concentration of adatoms on a *flat* palladium surface at the given temperature. Since none of these parameters depends on the density and kind of defects in the substrate we introduce an extra parameter κ to account for the combined effect

of these additional variables:

$$D'_c(r) = \kappa D_c(r) .$$ (6.2)

The parameter κ depends on the defect density and interaction strength of the defects with the Pd clusters, but we assume it to be independent of the cluster size.

The growth rate can be calculated by calculating the frequency of binary collisions. The collision frequency between clusters with sizes i and j is given by $(D_i + D_j) n_i n_j$, with D_i (D_j) the diffusion constant, and n_i (n_j) the density of clusters with size i (j). The only free fitting parameter in the model is the product $\kappa \rho_\infty D_{Pd}^{Pd}$. For the strongly reduced surface we find $\kappa \rho_\infty D_{Pd}^{Pd} = (4 \pm 1) \times 10^{-4}\,\text{Hz}$ and for the mildly reduced surface we find $\kappa \rho_\infty D_{Pd}^{Pd} = (1.5 \pm 0.7) \times 10^{-1}\,\text{Hz}$, a difference of almost a factor 400. Both fits in Fig. 6.4 are excellent.

Particle growth is characterized by a decreasing particle density and an increasing particle height. By determining both the particle density and the average particle height two independent measures of particle size are obtained. As was shown in Chapter 5, this provides us with an indication of the shape of the particles, which is not affected by the tip convolution effects, familiar in STM images. In Figure 6.5 the average cluster size, the coverage divided by the cluster density, is plotted as a function of average cluster height, both for the mildly and for the strongly reduced substrate. The data for the strongly reduced substrate were presented already in Chapter 5. The clusters on the mildly reduced substrate are clearly flatter than those on the strongly reduced substrate. In the STM images the clusters appear to be much wider than indicated in Fig. 6.5. This is probably caused by tip convolution. Xu *et al.* [64] also reported relatively wide, flat particles in their STM images of Pd particles on TiO_2. However, they claim not to suffer from tip convolution effects.

6.4 Discussion

We have shown that similar growth experiments of palladium clusters on differently prepared TiO_2 (110) substrates result in different average cluster sizes and spatial distributions. At this stage we cannot decide what is responsible for the large difference in the reduction of the titania surface between the two different treatments. The difference between the two treatments is modest. In each preparation cycle the strongly reduced surface was annealed twice as long, at 30 degrees higher than the mildly reduced surface. The sputter dose per cycle was equal.
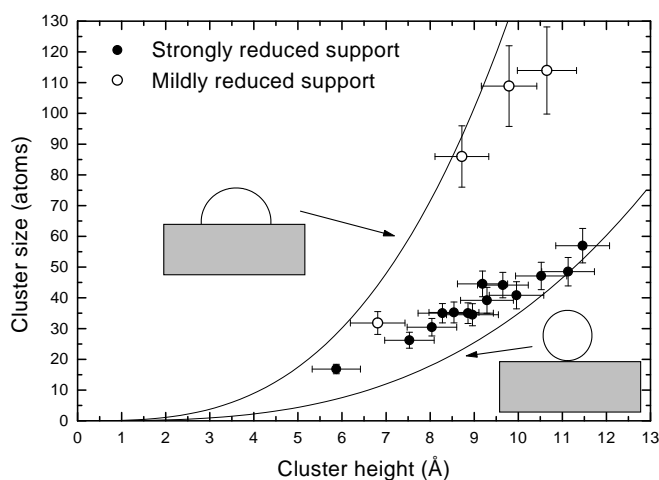
Figure 6.5: *The average cluster size (coverage divided by cluster density) as a function of average cluster height. The solid curves show the relation between size and height for spheres and hemispheres. Clusters on a mildly reduced substrate (open circles) are flatter than clusters on a strongly reduced substrate (filled circles, see Chapter 5).*

The damage and disorder created by sputtering results in the formation of Ti^{3+} in the surface region [50, 118]. Both the damage and the Ti^{3+} are removed again by annealing [50]. However, at elevated temperatures oxygen leaves the sample, and oxygen vacancies are created at the surface. Therefore the temperature and duration of the annealing treatments are probably the two most important factors controlling the final reduction and morphology of the surface.

The depletion of oxygen typically reported for the surface layer is much higher than the oxygen depletion of the bulk of the crystal [59, 77]. The range over which this effect extends into the bulk will probably depend on the rates of diffusion of Ti interstitials and oxygen vacancies from the bulk to the surface and vice versa. The extent to which this more strongly reduced surface region is removed during sputtering might thus be a third important factor. If the reduced surface region is completely removed by sputtering, every annealing step in the cleaning cycles will start from a more or less similar situation. If the surface layer is not completely removed, the annealing step will start with a more and more reduced surface with every cleaning cycle, and the reduced region will grow in width. Therefore the *ratio* between sputtering time and annealing time may be one of the

key parameters determining the final degree of reduction at the surface. However, as was discussed in Chapter 3, a more detailed investigation of the preparation of the TiO_2 (110) surface [118] shows that the resulting surface morphology depends in a even more complex way on the full sample history, for example via the degree of bulk reduction.

As shown in Chapter 5, Pd clusters on TiO_2 (110) do not grow by ripening but mainly by coalescence of mobile clusters [114]. The observed difference in growth rate implies a difference in palladium cluster diffusion coefficients on the TiO_2 surfaces. The only structural difference that we can directly observe is in the density of added Ti_2O_3 rows on the TiO_2 surface. With both AES and STM we did not detect any contamination on the surface, which might account for the remarkable difference in growth rate. Also the pressure and composition of the residual gas in the chamber ($p < 10^{-9}$ mbar) was comparable in both cases. Thus, it is likely that the difference in the degree of reduction at the surface is directly responsible for the difference in palladium particle growth rate. Indeed there seems to be a clear preference for Pd clusters to reside at the end points of added rows (see e.g. Fig. 6.2).

The added rows are not the only kind of defect on a reduced TiO_2 (110) surface. Also in the terrace isolated oxygen vacancies are present. Unfortunately in most of our images the resolution was not sufficient to identify these vacancies. Also, the appearance of these vacancies in the STM images was found to depend strongly on the state of the tip. However, since both the isolated vacancies and the added rows are caused by the reduction of the oxide crystal, it seems likely that on a sample with a high density of added rows, the density of isolated vacancies is high too. It is very well possible that also the isolated vacancies reduce the growth rate. Finally, since the steps trap the clusters, also they slow down the growth process.

We can think of two possible ways by which the defects can change the diffusion constant of the palladium clusters. If the clusters form a stronger bond with the substrate at defect sites, these sites can act as traps and effectively slow down the particles. This is probably the case for the steps and added rows, since the clusters are preferentially located on these sites. An alternative mechanism by which the oxygen vacancies might reduce the mobility of Pd clusters is strong repulsion. If Pd clusters avoid the vacancies, the one-dimensional motion of the clusters can be hindered strongly by a modest density of vacancies (see below).

The two values that we have found for $\kappa\rho_\infty D_{Pd}^{Pd}$ are very small, especially

on the strongly reduced surface. The product $\rho_\infty D_{Pd}^{Pd}$ represents the frequency with which each site on a flat palladium surface would on average be visited by a Pd adatom. At roughly one third of the melting temperature this frequency is very likely to be much higher than observed here. We can make a lower limit estimate using values from Effective Medium Theory calculations by Stoltze [119]. The adatom creation energy is highest on the (111) plane of Pd and was calculated to be $\approx 0.6\,\mathrm{eV}$ [119]. The activation energy for diffusion is higher on the (001) plane than on the (111) plane. For the (001) plane $0.5\,\mathrm{eV}$ was calculated [119]. However, probably an additional activation barrier is involved in the transfer of a Pd atom from one facet of the cluster to another [120]. Therefore we use a higher value for the activation energy for diffusion of $0.6\,\mathrm{eV}$ and a low pre-exponential factor of $10^{11}\,\mathrm{Hz}$ for a lower limit estimate, and predict $\rho_\infty D_{Pd}^{Pd} \approx 100\,\mathrm{Hz}$. Combining the high value expected for $\rho_\infty D_{Pd}^{Pd}$ with the low values found for $\kappa\rho_\infty D_{Pd}^{Pd}$, we see that even on the mildly reduced surface κ is much smaller than unity and the influence of added rows, isolated vacancies and steps is still very large. A more sophisticated model which includes the influence of the defects on the speed of diffusion would have to incorporate both the density and interaction strength of the defects, like for example the model that has been used by Venables and Harding to describe defect-induced nucleation [93].

The flatter shape of the particles on the mildly reduced substrate conflicts with simple expectations. In a simple picture one might anticipate that palladium binds more strongly to the substrate on defect sites, and thus defects could lower the interfacial energy. This would result in improved wetting and flatter particles on a strongly reduced substrate [22], which is precisely opposite to our observations. On the mildly reduced surface many clusters are located at steps. Since our automated cluster detection algorithm measures the height of the clusters with respect to the upper terrace, it may underestimate the true height. However, since the steps are only $3.25\,\text{Å}$ high this is a modest effect that cannot explain the difference in observed particle shape. An alternative explanation is related to the growth rate. On the mildly reduced surface the growth rate is much higher than on the strongly reduced surface. Therefore coalescence events are more frequent. This may cause the clusters to have insufficient time to equilibrate their shape. However, since the clusters grow by coalescence of mobile clusters, and the clusters move by fluctuating their shape, it is impossible that the clusters cannot equilibrate their shape between subsequent coalescence events and thus the difference in growth rate can-

not explain the difference in shape.

The only explanation that we have for the dependence of the average cluster shape on the degree of substrate reduction is as follows. The data for the strongly reduced substrate suggest that the contact area with the support is not allowed to change when the particles become bigger (see Chapter 5). In Chapter 5 we suggested that it is equal to the minimum possible contact area of a cluster, which amounts to 7 Pd atoms. By contrast, Figure 6.5 shows that on a mildly reduced substrate the contact area is allowed to grow with increasing particle size. This indicates that the presence of a high density of oxygen vacancies limits the contact area. Although we cannot see with the tunneling microscope what is underneath a cluster we propose that the clusters prefer *not* to be on top of vacancy sites. Then the size of the contact area is limited by the average distance between defects, and thus by the defect density. If it is difficult for the clusters to pass defect sites, this can dramatically slow down the diffusion and growth of the particles on substrates with a higher defect density, in particular when the diffusion is almost completely one-dimensional. Typically a few percent of the oxygen atoms in the first layer of a TiO_2 (110) surface is missing. This corresponds to an average distance between missing oxygen atoms of just a few atomic spacings, which agrees reasonably well with the typical contact diameter, ranging from $6.5\,\text{Å}$ on the strongly reduced surface to $20\,\text{Å}$ on the mildly reduced surface. The avoidance by clusters of the oxygen vacancies is corroborated by STM movies of the cluster motion [115]. In addition, the movies suggest a tendency for the clusters to be attracted to positions directly next to a vacancy.

6.5 Conclusions

Using Scanning Tunneling Microscopy we have shown in this chapter that the growth rate of small palladium particles on TiO_2 (110) is very strongly affected by the oxidation state of the TiO_2 surface. Oxygen vacancies and added rows are created as a consequence of a reduction of the oxide at high temperatures. The defects and steps hinder diffusion and therefore slow down particle growth. After deposition at room temperature, clusters are distributed over the terraces on a substrate with a high defect concentration, whereas a large fraction of the clusters is found at steps running perpendicular to the [001] direction on a substrate with a low defect density. The growth rate of the palladium particles at $672\,\text{K}$ was changed by nearly

a factor 400 as a result of a modest change in the preparation of the oxide surface. A simple model for coalescence growth can reproduce the observed growth rates, but only for very low values for the rate-determining parameter. We expect that on a truly perfect substrate, i.e. without any oxygen defects or steps, the growth can be even several orders of magnitude faster than has been observed here on the substrate with the lowest defect concentration. On a substrate with a low defect density the clusters are flatter than on a substrate with a high density. We propose that clusters energetically disfavour positions directly on top of vacancy sites and that the average contact area between a cluster and the substrate is limited by the average distance between these vacancies.

VII

Supported Pd nanoparticles in a reducing environment

In this chapter we present our first results in a study of the effect a H_2 atmosphere on a Pd/TiO$_2$ model catalyst. We find that annealing a TiO$_2$(110) surface at 672 K in 10^{-5} mbar H_2 results in an increased density of added rows on the surface, which is indicative of an increased depletion of oxygen of this surface. In the presence of small supported Pd particles, this process proceeds in a similar manner. The shape and growth rate of the Pd particles seem to be unaffected by the presence of hydrogen gas.

7.1   Introduction

In the previous two chapters (Chapters 5 and 6) we showed that very small metallic clusters (Pd) can easily be prepared by the deposition in ultra-high vacuum of small amounts of metal on an oxide surface (TiO$_2$). We investigated the growth process and the influence of the substrate preparation on the growth rate. The experiments on this model supported catalyst that were described in the previous chapters were all performed under Ultra-High Vacuum (UHV) conditions. In practical settings a catalyst is obviously not used in vacuum. Instead the operating pressures can be very high. It is possible, and even likely that the presence of the reactants and reaction products influence several important properties of the catalyst. For example, the surfaces of many metals undergo reconstruction upon the exposure to several gases [14]. Gas adsorption lowers the surface free energy [15]. The amount of energy lowering is usually different on different crystal faces. As a consequence, gas adsorption results in a change in the balance of free energies of the faces of a crystal. For large size crystals this can lead to adsorption-induced faceting [121–123].

113

Nanocrystals can respond by changing their shape [22]. In addition, the presence of a gaseous atmosphere may alter existing diffusion mechanisms or even promote new ones, which will result in a higher or lower sintering rate. It has been shown for example that the presence of hydrogen can significantly increase the diffusion rate of single adatoms on the Pt (110) surface [124]. In this chapter we present our first results on the effect of a reducing (H_2) atmosphere on our 'model catalyst', Pd on TiO_2 (110).

7.2 Experimental procedures

The experiments were performed in a UHV chamber with a base pressure of 1×10^{-10} mbar. This set-up was described in detail in Chapter 2. A polished $1 \times 1\,cm^2$ TiO_2 single crystal with (110) surface orientation was mounted in a molybdenum holder which could be heated by thermal radiation and electron bombardment from a filament. The surface was cleaned by several cycles of 30 min 600 eV Ar^+-ion bombardment with a target current of $1\,\mu A$ and annealing at 920 K for 10 min. This resulted in a light blue sample, which indicated a mild reduction of the bulk of the crystal. The contamination level was below the detection limit of Auger Electron Spectroscopy (AES) and the surface showed a clear 1×1 Low Energy Electron Diffraction (LEED) pattern. The preparation procedures used for this surface were described in more detail in Chapter 3.

Pd was deposited with an e-beam evaporator, while the sample was kept at room temperature. The amount of deposited material was measured with a Quartz Crystal Microbalance thickness monitor and was the same as in the previous chapters, namely $(4.9 \pm 0.2) \times 10^{13}$ atoms/cm². The deposition rate was also the same: $(3.4 \pm 0.2) \times 10^{11}$ atoms/s·cm². The thickness monitor was calibrated *ex-situ* with Rutherford Backscattering Spectrometry, as was described in Chapter 2.

Both before and after deposition the samples were investigated with Scanning Tunneling Microscopy (STM). The STM measurements were all performed at room temperature with positive sample bias voltages between 1.5–2.5 V and low tunneling currents of typically 0.05–0.1 nA. The tip was electrochemically etched from a 0.25 mm diameter tungsten wire. The sizes and positions of Pd clusters in the STM images were extracted using the automated cluster detection algorithm described in Chapter 2.

The samples were exposed to H_2 (Messer Griesheim, 99.999 % purity) by
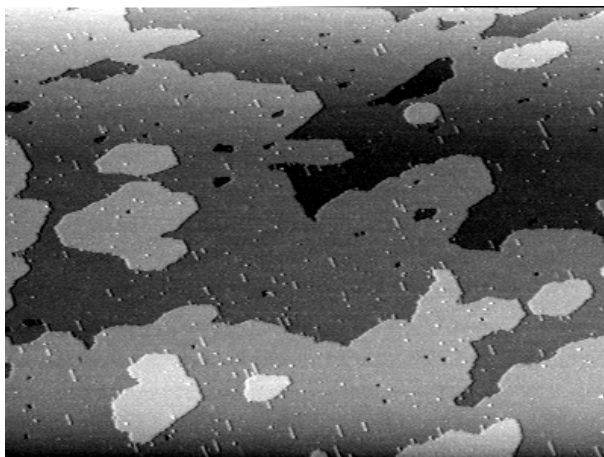
Figure 7.1: *This $3330\,\text{Å} \times 2497\,\text{Å}$ STM image shows the topography of the TiO$_2$ (110) substrate after several cycles of 30 min sputtering with 600 eV Ar$^+$ ions, followed by 10 min annealing at 920 K. Contamination could not be detected, and large terraces are visible, separated by single height steps. A relatively low density of added rows is formed. The image was recorded with a sample bias of $V_t = 2.5\,V$ and a tunneling current of $I_t = 0.04\,nA$.*

admitting the gas into the chamber via a needle valve. Exposures were performed both at room temperature and at 672 K.

7.3   Results

The morphology of the TiO$_2$ (110) surface after preparation in UHV was discussed in detail in Chapter 3. Due to the mild reduction of the sample at the elevated preparation temperature both isolated oxygen vacancies and 'added rows' were formed (see Chapter 3 and Refs. [49, 52, 53, 55, 62, 70, 71]). The precise substrate morphology depends critically on the details of the preparation conditions and on the preceding sample history. Figure 7.1 shows an STM image of the TiO$_2$ (110) surface topography after several cycles of sputtering and 10 min annealing at 920 K. The image shows large terraces and a relatively low density of added rows (see Chapters 3 and 6).

As was shown in Chapter 5, deposition of small quantities of Pd results in the formation of small 3-dimensional clusters. This is illustrated in Figure 7.2 which shows an STM image after deposition of $\sim 0.03\,$ML of palladium on the
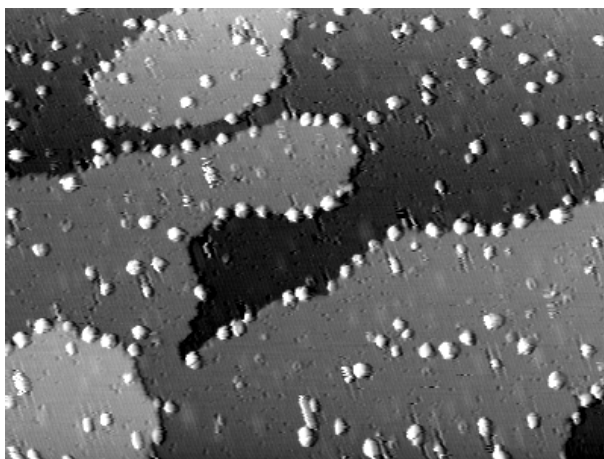
Figure 7.2: *STM image (1110 Å × 833 Å) after deposition of 4.9 × 10^{13} atoms/cm^2 (≈ 0.03 ML) Pd on the TiO$_2$ substrate (V_t =2.5 V, and I$_t$ =0.05 nA). Deposition was performed at room temperature. The deposited palladium atoms form three-dimensional clusters. The clusters are located preferentially at step sites, but are also present on the terraces.*

surface shown in Figure 7.1. Many clusters are located at step edges, but also on the terraces clusters are found. These observations agree well with the description given in Chapter 6 for palladium deposition on a mildly reduced surface. In Fig. 7.2 the added rows are imaged as line depressions. We have sometimes observed changes in contrast of the added rows from elevations to depressions and back at random moments, and attribute these to changes at the apex of the STM tip, for example due to adsorption or desorption of molecules from the residual gas.

In order to investigate the behaviour of this surface under reducing conditions, we exposed it to 10^{-5} mbar H$_2$ at room temperature for 20 minutes. This exposure did not result in noticeable changes in either substrate or clusters. Figure 7.3 shows STM images after annealing the sample at 672 K in 10^{-5} mbar H$_2$ for 20 min (Fig. 7.3a) and for 180 min (Fig. 7.3b). Annealing of the sample in hydrogen results in a decrease in the Pd cluster density and a growth of the average particle size. Furthermore the density of added rows on the substrate increases with annealing time. The added row density in Fig. 7.3b is higher than that in Fig. 7.3a, which is again higher than the added row densities in Figs. 7.1 and 7.2.

Under UHV conditions added rows are formed on the TiO$_2$ (110) surface

(a)

(b)
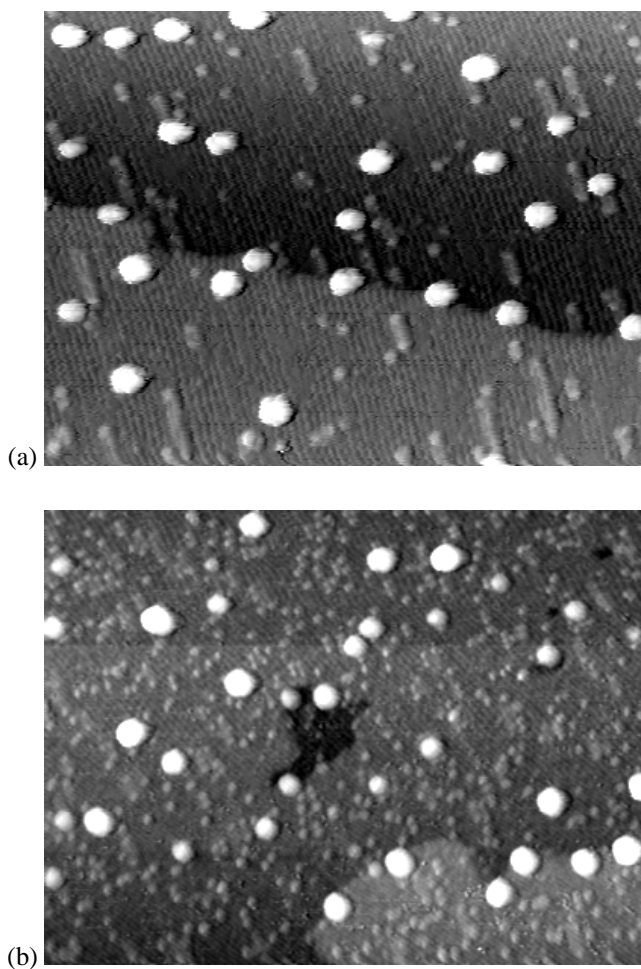
Figure 7.3: *These two STM images illustrate the effect of annealing the Pd/TiO$_2$ sample in H$_2$. Image (a) was recorded after 20 min annealing to 672 K in 10^{-5} mbar H$_2$. Image dimensions are 555 Å × 416 Å (V_t =2.51 V, I_t =0.1 nA). Image (b) was recorded after a total of 180 min annealing under the same conditions as image (a). This image measures 1110 Å × 833 Å and was recorded with V_t =2.45 V, and I_t =0.1 nA. The images illustrate that upon annealing the Pd particles grow in size. At the same time the particle density decreases. During annealing in a H$_2$ atmosphere the TiO$_2$ substrate is modified. After 20 min annealing (image a) the density of bright rows and spots has increased with respect to the situation after deposition, before annealing in H$_2$. Further annealing (image b) results in a further increase of these features.*
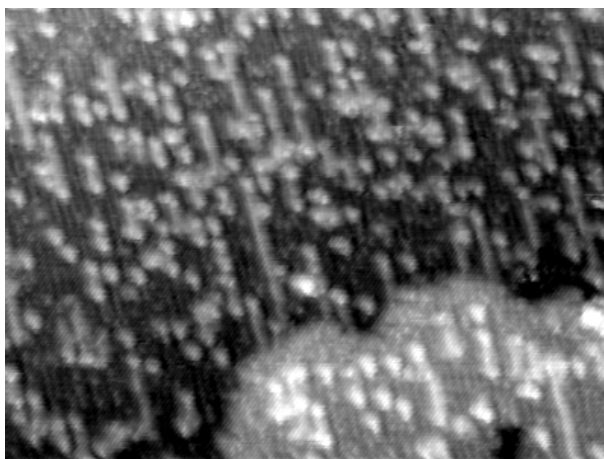
Figure 7.4: *Upon annealing of the bare TiO$_2$ (110) substrate in a hydrogen atmosphere the added row density increases dramatically, indicating a reduction of the surface layer. This STM image was measured after annealing a freshly prepared substrate (like in Fig. 7.1) at 672 K for 80 min in 10^{-5} mbar H$_2$. The image measures 500 Å × 375 Å and was recorded with V$_t$ = 2.36 V and I$_t$ = 0.07 nA.*

as a consequence of reduction of the crystal at elevated temperatures (> 800 K) [52, 53, 55, 62, 70, 71]. At lower temperatures, like the 672 K used here, we never observed large changes in surface morphology in UHV. Therefore the increased added row density must be related to the exposure to hydrogen. Since palladium possibly assists in the dissociation of the hydrogen molecules, the presence of the Pd clusters on the surface might be a necessary ingredient in the observed accelerated reduction. In order to investigate this, we also annealed a bare substrate at 672 K in 10^{-5} mbar hydrogen. The results are shown in Figure 7.4. Clearly the added row density on the substrate also increases in the absence of palladium. At this point we could not yet detect any changes in surface composition with XPS, even though the STM images clearly show that the surface had been modified.

The rate of growth of the Pd nanoparticles can be studied quantitatively by evaluating the cluster densities as a function of annealing time. The cluster density is easily obtained by counting the clusters in the STM images. As was explained in Chapters 2 and 5 we used an automated cluster detection algorithm to obtain these numbers. In Figure 7.5 the cluster density is presented as a function of the number of 10 minute annealing cycles at 672 K. We performed two series of
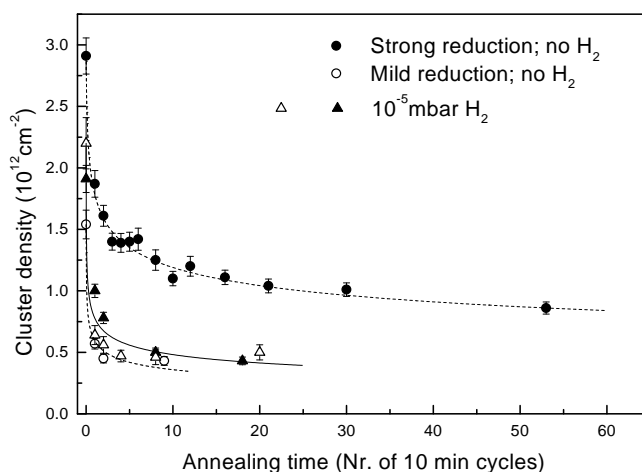
Figure 7.5: *Palladium particle growth as a function of annealing time. The sample was heated in 10 min cycles to 672 K. The solid and open circles were obtained in the absence of a hydrogen atmosphere on strongly and mildly reduced substrates respectively. They were presented in in Chapters 5 and 6, together with the dashed curves that represent the best fits with the coalescence growth model. The solid and open triangles were obtained in two separate series of experiments, in which the sample was exposed to 10^{-5} mbar H_2 during the annealing cycles. The solid curve is a calculation for the decrease in cluster density according to the coalescence model with $\kappa\rho_\infty D_{Pd}^{Pd} = 4 \times 10^{-2}$ Hz.*

experiments in 10^{-5} mbar H_2, and in Figure 7.5 these data are combined with the data presented in Chapters 5 and 6. The solid curve was calculated with the model for coalescence growth described in these chapters. The best-fit value for the rate constant in this model, $\kappa\rho_\infty D_{Pd}^{Pd}$, was found to be $(4 \pm 2) \times 10^{-2}$ Hz. Both the initial cluster density and the growth rate for the two series of experiments performed in H_2 are in between those observed in the two cases discussed in Chapter 6, for a mildly reduced substrate and for a strongly reduced substrate.

In Chapter 5 we demonstrated how information on the shape or 'flatness' of the particles can be obtained by comparing the average size (volume) of the clusters with the average height. This is shown in Figure 7.6. The average size is easily obtained by dividing the total density of deposited material by the observed density of clusters. In Fig. 7.6 the data obtained in 10^{-5} mbar H_2, are compared with previously presented data for particle growth on a strongly reduced substrate
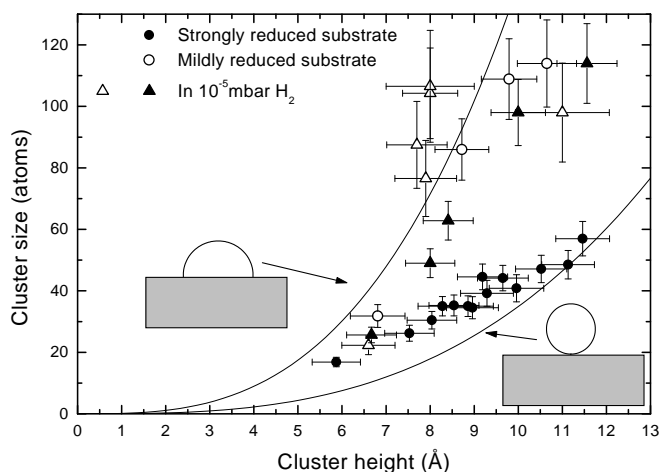
Figure 7.6: *An indication of the shape of the particles is obtained when the average cluster size is plotted as a function of average cluster height. The average size is obtained by dividing the density of deposited material by the density of clusters. The solid circles were obtained for particles on a strongly reduced substrate, growing in UHV. The open circles were obtained on a mildly reduced surface in UHV, whereas the solid and open triangles were obtained for particles growing in 10^{-5} mbar H_2 on a relatively mildly reduced surface. The solid and open circles were taken from Chapters 5 and 6. The solid curves indicate the relation between size and height for spheres and hemispheres.*

(see Chapter 5) and for a mildly reduced surface (see Chapter 6). As was explained before, the lateral dimensions of the particles in the images are often much larger than the true diameter because of the convolution of particle and tip shapes. Therefore the apparent diameters of the particles were not used in our analysis. Although one of the series shows quite some scatter, Figure 7.6 shows that the data for the hydrogen annealed sample are very close to those for the mildly reduced sample in UHV, and they deviate considerably from the trend observed in Chapter 5 for the strongly reduced substrate.

7.4 Discussion

Our measurements show that the morphology of the TiO_2 (110) substrate is strongly affected by annealing the surface at 672 K in 10^{-5} mbar H_2. The high-temperature exposure to hydrogen gas results in an increase in the density of added rows,

whereas annealing at the same temperature in UHV does not result in noticeable changes at the surface. Since the formation of these added rows is associated with the reduction of the sample, we conclude that hydrogen is responsible for an enhanced reduction of the titania surface. However, we do not observe changes in XPS, which probes several layers deep. This implies that the reducing effect of H_2 stays limited to the very surface layer. On stoichiometric $TiO_2(110)$ the sticking and dissociation probabilities for H_2 are very low, but on step and defect sites sticking and dissociation may be much more likely [19, 50]. At room temperature, exposure to 10^{-5} mbar H_2 did not result in noticeable changes at the surface. Probably dissociation of the H_2 molecule or its reaction with the surface are activated processes that require more energy than available at room temperature.

The presence of palladium particles does not have a large influence on the reduction of the oxide substrate. Nevertheless, dissociation of the hydrogen molecules is probably much easier on these particles [14], so that one might expect that Pd acts as a catalyst for the reduction of the oxide. There can be several reasons for the absence of an increased rate of reduction. First of all, the dissociation may not be the rate limiting step. Instead the reduction rate may be limited by the reaction rate of hydrogen atoms with the oxide crystal, or by the desorption rate of water molecules. Alternatively, hydrogen atoms or molecules might not spill over from the Pd particles to the oxide substrate, or, if they do, desorb before they can diffuse significant distances over the substrate.

In Chapter 6 we showed that both the initial cluster density and the growth rate of the clusters are strongly influenced by the density of defects (oxygen vacancies and added rows) on the substrate surface. The results presented here are close to those for the mildly reduced surface. The initial cluster density is slightly higher, and the growth rate is slightly lower. Both features indicate that the substrate is probably slightly more reduced than the mildly reduced surface described in Chapter 6. However, during annealing in hydrogen the surface becomes more and more reduced. Based on this we should expect the growth of the Pd particles to slow down dramatically during the process. Nevertheless, the solid curve shown in Fig. 7.5 was calculated without taking such a deceleration of the growth into account. We explain this as follows. The largest changes in cluster density occur in the very first annealing cycle. However, as the particles grow larger, the process slows down rapidly (see Chapter 5). The hydrogen induced reduction of the substrate on the other hand does not follow this behaviour. Instead the reduction

increases steadily. As a consequence, during the first annealing cycle when most of the growth takes place, the substrate is still only mildly reduced. After the second annealing cycle the added row density on the surface has clearly increased, but still it is about a factor 5 lower than the added row density on the strongly reduced sample. Only after 8 annealing cycles the level of reduction is comparable with that on the strongly reduced surface. In that stage however, the growth has become so slow anyway that an additional reduction of the growth rate due to the ongoing reduction of the surface, would be very difficult to distinguish. Our data show that the hydrogen atmosphere has no direct effect on the diffusion rate of the Pd particles. Increased diffusion rates in a hydrogen atmosphere have been reported for Pt adatoms on Pt (110) [124].

Since the presence of hydrogen gas changes the surface free energies, and the reduction of the substrate due to the hydrogen may affect the interface energy, the shape of the particles may change. However, both sets of data for the hydrogen annealed samples follow the same trend as data for the mildly reduced sample annealed in UHV, and they deviate from the data for particles on a strongly reduced substrate, annealed in UHV. In Chapter 6 we argued that the average diameter of the contact of the clusters with the substrate might be limited by the average distance between oxygen vacancies in the substrate surface. Since the density of oxygen vacancies increases when the sample is annealed in hydrogen we would expect to see a cross-over in Fig. 7.6 from the behaviour for the mildly reduced surface (hemispherical particles) towards the trend for the strongly reduced surface (spherical particles). There may be a slight indication for this in the last datapoints of the two series for annealing in hydrogen, but the scatter in the data is relatively large.

7.5 Conclusions

In summary, in the presence of 10^{-5} mbar hydrogen the TiO_2 (110) surface is reduced and added rows are formed at a lower temperature (672 K) than under UHV conditions. This reduction seems to be limited to the surface layer only. The growth of Pd nanoparticles in this hydrogen atmosphere can be described by the same model for coalescence growth as the one that explains the growth in vacuum (Chapters 5 and 6). The growth rate of the Pd particles and the average particle shape found during annealing in hydrogen are very close to those found in the ab-

sence of hydrogen on TiO$_2$ substrates with a similar mild degree of reduction. We did not find indications that the presence of hydrogen influences the growth rate of the palladium particles directly. Also the shape of the particles is not affected noticeably by the presence of hydrogen.

References

[1] G. Mie, Beitrage zur Optik trüber Medien, speziell kolloidaler Metallösungen, Ann. Phys. **25**, 377–445 (1908).

[2] U. Kreibig and M. Vollmer, *Optical properties of metal clusters*, volume 25 of *Springer series in materials science*, Springer-Verlag, Berlin, 1995.

[3] R. F. Service, Small clusters hit the big time, Science **271**, 920–922 (1996).

[4] A. P. Alivisatos, Semiconductor clusters, nanocrystals, and quantum dots, Science **271**, 933–937 (1996).

[5] D. J. Wales, Structure, dynamics, and thermodynamics of clusters: Tales from topographic potential surfaces, Science **271**, 925–929 (1996).

[6] S. Veprek, Electronic and mechanical properties of nanocrystalline composites when approaching molecular size, Thin Solid Films **297**, 145–153 (1997).

[7] M. Brack, Metal clusters and magic numbers, Sci. Am. **277**, 30–35 (1997).

[8] Y. Volokitin, J. Sinzig, L. J. de Jongh, G. Schmid, M. N. Vargaftik, and I. I. Moiseev, Quantum-size effects in the thermodynamic properties of metallic nanoparticles, Nature **384**, 621–623 (1996).

[9] J. M. Thomas and W. J. Thomas, *Principles and practice of heterogeneous catalysis*, VCH, Weinheim, 1997.

[10] R. A. van Santen, P. W. N. M. van Leeuwen, J. A. Moulijn, and B. A. Averill, *Catalysis: An integrated approach, Second, revised and enlarged edition*, Elsevier, Amsterdam, 1999.

[11] G. C. Bond, *Heterogeneous catalysis: Principles and applications*, Oxford University Press, Oxford, 1987.

[12] P. Stoltze, Introduction to heterogeneous catalysis, `http://www.aue.auc.dk/~stoltze/catal/book/main.htm`.

[13] P. L. J. Gunter, J. W. Niemantsverdriet, F. H. Ribeiro, and G. A. Somorjai, Surface science approach to modeling supported catalysts, Catal. Rev.—Sci. Eng. **39**, 77–168 (1997).

[14] G. A. Somorjai, *Introduction to surface chemistry and catalysis*, John Wiley & Sons, New York, 1994.

[15] A. Zangwill, *Physics at surfaces*, Cambridge University Press, Cambridge, 1988.

[16] G. Ertl, Oscillatory kinetics and spatiotemporal self-organization in reactions at solid-surfaces, Science **254**, 1750–1755 (1991).

[17] G. K. Wertheim, Electronic structure of metal clusters, Z. Phys. D **12**, 319–326 (1989).

[18] M. Valden, X. Lai, and D. W. Goodman, Onset of catalytic activity of gold clusters on titania with the appearance of nonmetallic properties, Science **281**, 1647–1650 (1998).

[19] V. E. Henrich and P. A. Cox, *The surface science of metal oxides*, Cambridge University Press, Cambridge, 1994.

[20] M. Bäumer and H.-J. Freund, Metal deposits on well-ordered oxide films, Prog. Surf. Sci. **61**, 127–198 (1999).

[21] D. W. Goodman, Model catalysts: From extended single crystals to supported particles, Surface Review and Letters **2**, 9–24 (1995).

[22] C. R. Henry, Surface studies of supported model catalysts, Surf. Sci. Rep. **31**, 231–325 (1998).

[23] C. T. Campbell, Ultrathin metal films and particles on oxide surfaces: structural, electronic and chemisorptive properties, Surf. Sci. Rep. **27**, 1–111 (1997).

[24] E. W. Kuipers, C. Laszlo, and W. Wieldraaijer, Deposition of nanocrystals on flat supports by spin-coating, Catal. Lett. **17**, 71–79 (1993).

[25] H. Poppa, Nucleation, growth and TEM analysis of metal particles and clusters deposited in UHV, Catal. Rev.–Sci. Eng. **35**, 359–398 (1993).

[26] A. K. Datye and D. J. Smith, The study of heterogeneous catalysts by high-resolution Transmission Electron Microscopy, Catal. Rev.–Sci. Eng. **34**, 129–178 (1992).

[27] G. Binnig, H. Rohrer, Ch. Gerber, and E. Weibel, Tunneling through a controllable vacuum gap, Appl. Phys. Lett. **40**, 178–180 (1982).

[28] G. Binnig, H. Rohrer, Ch. Gerber, and E. Weibel, Surface studies by Scanning Tunneling Microscopy, Phys. Rev. Lett. **49**, 57–61 (1982).

[29] J. C. Chen, *Introduction to Scanning Tunneling Microscopy*, Oxford University Press, New York, 1993.

[30] G. Binnig, H. Rohrer, Ch. Gerber, and E. Weibel, 7×7 reconstruction on Si(111) resolved in real space, Phys. Rev. Lett. **50**, 120–123 (1983).

[31] M. S. Hoogeman, *Surfaces in motion: A variable-temperature scanning tunneling microscopy study*, PhD thesis, Leiden University, Leiden, The Netherlands, 1998.

[32] P. B. Rasmussen, B. L. M. Hendriksen, H. Zeijlemaker, H. G. Ficke, and J. W. M. Frenken, The "Reactor STM": A scanning tunneling microscope for investigation of catalytic surfaces at semi-industrial reaction conditions, Rev. Sci. Instrum. **69**, 3879–3884 (1998).

[33] B. J. McIntyre, M. Salmeron, and G. A. Somorjai, A variable pressure/temperature scanning tunneling microscope for surface science and catalysis studies, Rev. Sci. Instrum. **64**, 687–691 (1993).

[34] F. J. Giessibl, Atomic resolution of the Silicon (111)-(7×7) surface by Atomic Force Microscopy, Science **267**, 68–71 (1995).

[35] L. Kuipers, R. W. M. Loos, H. Neerings, J. ter Horst, G. J. Ruwiel, A. P. de Jongh, and J. W. M. Frenken, Design and performance of a high-temperature, high-speed scanning tunneling microscope, Rev. Sci. Instrum. **66**, 4557–4565 (1995).

[36] A. J. M. Mens and O. L. J. Gijzeman, AES study of electron beam induced damage on TiO_2 surfaces, Appl. Surf. Sci. **99**, 133–143 (1996).

[37] H. J. Hopman, J. Verhoeven, J. J. Scholtz, and R. Fastenau, Time variation of secondary electron emission during electron bombardment of rutile, Appl. Surf. Sci. **111**, 270–275 (1997).

[38] J. C. Russ, *The image processing handbook*, CRC Press, Boca Raton, Florida, 2nd edition, 1995.

[39] I. T. Young, J. J. Gerbrands, and L. J. van Vliet, *Lecture notes: Fundamentals of image processing*, Delft University of Technology, Delft, The Netherlands, 1995, see also: `http://www.ph.tn.tudelft.nl/Courses/FIP/frames/fip.html`.

[40] A. D. Weisman, E. R. Dougherty, H. A. Mizes, and R. J. D. Miller, Nonlinear digital filtering of scanning-probe-microscopy images by morphological pseudoconvolutions, J. Appl. Phys. **71**, 1565–1578 (1992).

[41] N. Bonnet, S. Dongmo, P. Vautrot, and M. Troyon, A mathematical morphology approach to image formation and image restoration in scanning tunnelling and atomic force microscopies, Micros. Microanal. Microstruct. **5**, 477–487 (1994).

[42] V. E. Henrich, Metal-oxide surfaces, Prog. Surf. Sci. **50**, 77–90 (1995).

[43] H. Over, Y. D. Kim, A. P. Seitsonen, S. Wendt, E. Lundgren, M. Schmid, P. Varga, A. Morgante, and G. Ertl, Atomic-scale structure and catalytic reactivity of the RuO_2(110) surface, Science **287**, 1474–1476 (2000).

[44] P. L. Gai-Boyes, Defects in oxide catalysts: Fundamental studies of catalysis in action, Catal. Rev.—Sci. Eng. **34**, 1–54 (1992).

[45] A. Fujishima and K. Honda, Electrochemical photolysis of water at a semiconductor electrode, Nature **238**, 37–38 (July 1972).

[46] R. L. Kurtz, Stimulated desorption studies of defect structures on TiO_2, Surf. Sci. **177**, 526–552 (1986).

[47] P. J. Møller and M.-C. Wu, Surface geometrical structure and incommensurate growth: ultrathin Cu films on TiO_2(110), Surf. Sci. **224**, 265–276 (1989).

[48] U. Diebold, J.-M. Pan, and T. E. Madey, Ultrathin metal film growth on TiO_2(110): an overview, Surf. Sci. **331–333**, 845–854 (1995).

[49] G. S. Rohrer, V. E. Henrich, and D. A. Bonnell, A scanning tunneling microscopy and spectroscopy study of the TiO_{2-x}(110) surface, Surf. Sci. **278**, 146–156 (1992).

[50] J.-M. Pan, B. L. Maschhoff, U. Diebold, and T. E. Madey, Interaction of water, oxygen, and hydrogen with TiO_2 (110) surfaces having different defect densities, J. Vac. Sci. Technol. A **10**, 2470–2476 (1992).

[51] B. Grossmann and P. Piercy, High resolution Low Energy Electron Diffraction study of flattening on the TiO_2(110) surface, Phys. Rev. Lett. **74**, 4487–4490 (1995).

[52] H. Onishi and Y. Iwasawa, Reconstruction of TiO_2 (110) surface: STM study with atomic-scale resolution, Surf. Sci. **313**, L783–L789 (1994).

[53] H. Onishi, K. Fukui, and Y. Iwasawa, Atomic-scale surface structures of TiO_2 (110) determined by scanning tunneling microscopy: A new surface-limited phase of titanium oxide, Bull. Chem. Soc. Jpn. **68**, 2447–2458 (1995).

[54] A. Szabo and T. Engel, Structural studies of TiO_2(110) using scanning tunneling microscopy, Surf. Sci. **329**, 241–254 (1995).

[55] P. W. Murray, N. G. Condon, and G. Thornton, Effect of stoichiometry on the structure of TiO_2 (110), Phys. Rev. B **51**, 10989–10997 (1995).

[56] A. Berkó and F. Solymosi, Study of clean TiO_2(110) surface by Scanning Tunneling Microscopy and Spectroscopy, Langmuir **12**, 1257–1261 (1996).

[57] G. Charlton, P. B. Howes, C. L. Nicklin, P. Steadman, J. S. G. Taylor, C. A. Muryn, S. P. Harte, J. Mercer, R. McGrath, D. Norman, T. S. Turner, and G. Thornton, Relaxation of TiO_2(110)-(1 × 1) using surface X-ray diffraction, Phys. Rev. Lett. **78**, 495–498 (1997).

[58] C. J. Kevane, Oxygen vacancies and electrical conduction in metal oxides, Phys. Rev. A **133**, 1431–1436 (1964).

[59] P. Kofstad, Note on the defect structure of rutile (TiO_2), J. Less-Common Metals **13**, 635–638 (1967).

[60] M. Aono and R. R. Hasiguti, Interaction and ordering of lattice defects in oxygen-deficient rutile TiO_{2-x}, Phys. Rev. B **48**, 12406–12414 (1993).

[61] Surface Preparation Laboratory, Penningweg 69F, 1507 DE Zaandam, The Netherlands, `http://www.surface-prep-lab.com`.

[62] S. Fischer, A. W. Munz, K.-D. Schierbaum, and W. Göpel, The geometric structure of intrinsic defects at TiO_2(110) surfaces: an STM study, Surf. Sci. **337**, 17–30 (1995).

[63] U. Diebold, J. F. Anderson, K.-O. Ng, and D. Vanderbilt, Evidence for the tunneling site on transition-metal oxides: TiO_2 (110), Phys. Rev. Lett. **77**, 1322–1325 (1996).

[64] C. Xu, X. Lai, G. W. Zajac, and D. W. Goodman, Scanning tunneling microscopy studies of the TiO_2(110) surface: Structure and the nucleation growth of Pd, Phys. Rev. B **56**, 13464–13482 (1997).

[65] M. S. Hoogeman, M. A. J. Klik, R. van Gastel, and J. W. M. Frenken, On the smoothing of rough surfaces, J. Phys.: Condens. Matter **11**, 4349–4365 (1999).

[66] U. Diebold, J. Lehman, T. Mahmoud, M. Kuhn, G. Leonardelli, W. Hebenstreit, M. Schmid, and P. Varga, Intrinsic defects on a TiO_2 (110)(1 × 1) surface and their re-

action with oxygen: a scanning tunneling microscopy study, Surf. Sci. **411**, 137–153 (1998).

[67] S. Suzuki, K. Fukui, H. Onishi, and Y. Iwasawa, Hydrogen adatoms on TiO_2 (110)-(1×1) characterized by Scanning Tunneling Microscopy and Electron Stimulated Desorption, Phys. Rev. Lett. **84**, 2156–2159 (2000).

[68] Q. Guo, I. Cocks, and E. M. Williams, Surface structure of (1×2) reconstructed TiO_2(110) studied using Electron Stimulated Desorption Ion Angular Distribution, Phys. Rev. Lett. **77**, 3851–3854 (1996).

[69] K. Fukui, H. Onishi, and Y. Iwasawa, Atom-resolved image of the TiO_2 (110) surface by noncontact Atomic Force Microscopy, Phys. Rev. Lett. **79**, 4202–4205 (1997).

[70] C. L. Pang, S. A. Haycock, H. Raza, P. W. Murray, G. Thornton, O. G. se ren, R. James, and D. W. Bullett, Added row model of TiO_2 (110) 1×2, Phys. Rev. B **58**, 1586–1589 (1998).

[71] R. A. Bennett, P. Stone, and M. Bowker, Two (1×2) reconstructions of TiO_2 (110): Surface rearrangement and reactivity studied using elevated temperature Scanning Tunneling Microscopy, Phys. Rev. Lett. **82**, 3831–3834 (1999).

[72] M. A. Henderson, Mechanism for the bulk-assisted reoxidation of ion sputtered TiO_2 surfaces: diffusion of oxygen to the surface or titanium to the bulk?, Surf. Sci. **343**, L1156–L1160 (1995).

[73] M. Li, W. Hebenstreit, L. Gross, U. Diebold, M. A. Henderson, D. R. Jennison, P. A. Schultz, and M. P. Sears, Oxygen-induced restructering of the TiO_2(110) surface: a comprehensive study, Surf. Sci. **437**, 173–190 (1999).

[74] H. Onishi and Y. Iwasawa, Dynamic visualization of a metal-oxide-surface/gas-phase reaction: Time-resolved observation by Scanning Tunneling Microscopy at 800 K, Phys. Rev. Lett. **76**, 791–794 (1996).

[75] M. Li, W. Hebenstreit, and U. Diebold, Morphology change of oxygen-restructured TiO_2(110) surfaces by UHV annealing: Formation of a low-temperature (1×2) structure, Phys. Rev. B **61**, 4926–4933 (2000).

[76] P. Stone, R. A. Bennett, and M. Bowker, Reactive re-oxidation of reduced TiO_2 (110) surfaces demonstrated by high temperature STM movies, New Journal of Physics **1**, 1.1–1.12 (1999).

[77] P. Kofstad, *Nonstoichiometry, diffusion and electrical conductivity in binary metal oxides*, John Wiley & Sons, New York, 1972.

[78] S. Rusponi, C. Boragno, and U. Valbusa, Ripple structure on Ag(110) surface induced by ion sputtering, Phys. Rev. Lett. **78**, 2795–2798 (1997).

[79] S. Rusponi, G. Constantini, C. Boragno, and U. Valbusa, Ripple wave vector rotation in anisotropic crystal sputtering, Phys. Rev. Lett. **81**, 2735–2738 (1998).

[80] S. Rusponi, G. Constantini, C. Boragno, and U. Valbusa, Scaling laws of the ripple morphology on Cu(110), Phys. Rev. Lett. **81**, 4184–4187 (1998).

[81] S. van Dijken, *Pattern formation and magnetic anisotropy in thin metal films*, PhD thesis, University of Twente, Enschede, The Netherlands, 2000.

[82] C. Herring, Some theorems on the free energies of crystal surfaces, Phys. Rev. **82**, 87–93 (1951).

[83] G. Wulff, Zur Frage der Geschwindigkeit des Wachsthums und der Auflösung der Krystallflächen, Z. Krist. **34**, 449–531 (1901).

[84] R. A. Bennett, S. Poulston, P. Stone, and M. Bowker, STM and LEED observations of the surface structure of TiO_2(110) following crystallographic shear plane formation, Phys. Rev. B **59**, 10341–10346 (1999).

[85] M. Bäumer, J. Libuda, A. Sandell, H.-J. Freund, G. Graw, T. Bertrams, and H. Neddermeyer, The growth and properties of Pd and Pt on Al_2O_3/NiAl(110), Ber. Bunsenges. Phys. Chem. **99**, 1381–1386 (1995).

[86] M. Meunier and C. R. Henry, Nucleation and growth of metallic clusters on MgO(100) by helium diffraction, Surf. Sci. **307–309**, 514–518 (1994).

[87] J. Evans, B. E. Hayden, and G. Lu, The adsorption of carbon monoxide on TiO_2(110) supported palladium, Surf. Sci. **360**, 61–73 (1996).

[88] P. W. Murray, J. Shen, N. G. Condon, S. J. Pang, and G. Thornton, STM study of Pd growth on TiO_2(100)-(1 $\times$ 3), Surf. Sci. **380**, L455–L458 (1997).

[89] P. Stone, S. Poulston, R. A. Bennett, and M. Bowker, Scanning tunnelling microscopy investigation of sintering in a model supported catalyst: nanoscale Pd on TiO_2(110), Chem. Commun. **13**, 1369–1370 (1998).

[90] P. J. F. Harris, Growth and structure of supported metal catalyst particles, Int. Mater. Rev. **40**, 97–115 (1995).

[91] C. H. Bartholomew, Sintering kinetics of supported metals: New perspectives from a unifying GPLE treatment, Appl. Catal. A **107**, 1–57 (1993).

[92] K. R. Heim, S. T. Coyle, G. G. Hembree, J. A. Venables, and M. R. Scheinfein, Growth of nanometer-size metallic particles on CaF_2(111), J. Appl. Phys. **80**, 1161–1170 (1996).

[93] J. A. Venables and J. H. Harding, Nucleation and growth of supported metal clusters at defect sites on oxide and halide (001) surfaces, J. Cryst. Growth **211**, 27–33 (2000).

[94] J. A. Venables, G. D. T. Spiller, and M. Hanbücken, Nucleation and growth of thin films, Rep. Prog. Phys. **47**, 399–459 (1984).

[95] Y. W. Mo, J. Kleiner, M. B. Webb, and M. G. Lagally, Surface self-diffusion of Si on Si(001), Surf. Sci. **268**, 275–295 (1992).

[96] J. W. Evans and M. C. Bartelt, Irreversible island formation during deposition: separation distributions and diffraction profiles, Surf. Sci. **284**, L437–L443 (1993).

[97] J. A. Stroscio and D. T. Pierce, Scaling of diffusion-mediated island growth in iron-on-iron homoepitaxy, Phys. Rev. B **49**, 8522–8525 (1994).

[98] J. A. Venables, Rate equation approaches to thin film nucleation kinetics, Philos. Mag. **27**, 697–738 (1973).

[99] N. C. Bartelt, W. Theis, and R. M. Tromp, Ostwald ripening of two-dimensional islands on Si(001), Phys. Rev. B **54**, 11741–11751 (1996).

[100] I. M. Lifshitz and V. V. Slyozov, The kinetics of precipitation from supersaturated solid solutions, J. Phys. Chem. Solids **19**, 35–50 (1961).

[101] B. K. Chakraverty, Grain size distribution in thin films - 1. Conservative systems, J. Phys. Chem. Solids **28**, 2401–2412 (1967).

[102] M. Zinke-Allmang, L. C. Feldman, and M. H. Grabow, Clustering on surfaces, Surf. Sci. Rep. **16**, 377–463 (1992).

[103] K. Morgenstern, G. Rosenfeld, B. Poelsema, and G. Comsa, Brownian motion of vacancy islands on Ag(111), Phys. Rev. Lett. **74**, 2058–2061 (1995).

[104] S. V. Khare, N. C. Bartelt, and T. L. Einstein, Diffusion of monolayer adatom and vacancy clusters: Langevin analysis and Monte Carlo simulations of their Brownian motion, Phys. Rev. Lett. **75**, 2148–2151 (1995).

[105] E. E. Gruber, Calculated size distributions for gas bubble migration and coalescence in solids, J. Appl. Phys. **38**, 243–250 (1967).

[106] D. Kandel, Selection of the scaling solution in a cluster coalescence model, Phys. Rev. Lett. **79**, 4238–4241 (1997).

[107] E. Ruckenstein and B. Pulvermacher, Growth kinetics and the size distributions of supported metal crystallites, J. Catal. **29**, 224–245 (1973).

[108] D. Kashchiev, Kinetics of thin film coalescence due to crystallite surface migration, Surf. Sci. **55**, 477–493 (1976).

[109] W. Theis, N. C. Bartelt, and R. M. Tromp, Chemical potential maps and spatial correlations in 2D-island ripening on Si(001), Phys. Rev. Lett. **75**, 3328–3331 (1995).

[110] G. R. Carlow, R. J. Barel, and M. Zinke-Allmang, Ordering of clusters during late-stage growth on surfaces, Phys. Rev. B **56**, 12519–12528 (1997).

[111] G. Rosenfeld, K. Morgenstern, I. Beckmann, W. Wulfhekel, E. Lægsgaard, F. Besenbacher, and G. Comsa, Stability of two-dimensional clusters on crystal surfaces: from Ostwald ripening to single-cluster decay, Surf. Sci. **402–404**, 401–408 (1998).

[112] T. R. Mattson, G. Mills, and H. Metiu, A new method for simulating the late stages of island coarsening in thin film growth: The role of island diffusion and evaporation, J. Chem. Phys. **110**, 12151–12160 (1999).

[113] M. J. J. Jak, C. Konstapel, A. van Kreuningen, J. Chrost, J. Verhoeven, and J. W. M. Frenken, The influence of substrate defects on the growth rate of palladium nanoparticles on a TiO_2 (110) surface, submitted to Surf. Sci., Chapter 6 in this thesis.

[114] M. J. J. Jak, C. Konstapel, A. van Kreuningen, J. Verhoeven, and J. W. M. Frenken, Scanning tunnelling microscopy study of the growth of small palladium particles on TiO_2 (110), Surf. Sci. **457**, 295–310 (2000), Chapter 5 in this thesis.

[115] A STM movie of a mobile Pd cluster on TiO_2 (110) is shown on the World Wide Web at `http://www.amolf.nl/research/thin_layer_lab`.

[116] A. R. Miedema and R. Boom, Surface tension and electron density of pure liquid metals, Z. Metallk. **69**, 183–190 (1978).

[117] B. Pluis, D. Frenkel, and J. F. van der Veen, Surface-induced melting and freezing II. A semi-empirical Landau-type model, Surf. Sci. **239**, 282–300 (1990).

[118] M. J. J. Jak, A. van Kreuningen, C. Konstapel, J. Chrost, J. Verhoeven, and J. W. M. Frenken, On the preparation of the TiO_2 (110) surface, Chapter 3 in this thesis.

[119] P. Stoltze, Simulation of surface defects, J. Phys.: Condens. Matter **6**, 9495–9517 (1994).

[120] F. Baletto, C. Mottet, and R. Ferrando, Molecular dynamics simulations of surface diffusion and growth on silver and gold clusters, Surf. Sci. **446**, 31–45 (2000).

[121] B. J. McIntyre, M. Salmeron, and G. A. Somorjai, In situ scanning tunneling microscopy study of platinum (110) in a reactor cell at high pressures and temperatures, J. Vac. Sci. Technol. A **11**, 1964–1968 (1993).

[122] J. S. Ozcomert, W. W. Pai, N. C. Bartelt, and J. E. Reutt-Robey, Kinetics of oxygen-induced faceting of vicinal Ag(110), Phys. Rev. Lett. **72**, 258–261 (1994).

[123] J. S. Ozcomert, W. W. Pai, N. C. Bartelt, and J. E. Reutt-Robey, Scanning tunneling microscopy study of the faceting dynamics of stepped Ag(110) upon oxygen exposure, J. Vac. Sci. Technol. A **12**, 2224–2228 (1994).

[124] S. Horch, H. T. Lorensen, S. Helveg, E. Lægsgaard, I. Stensgaard, K. W. Jacobsen, J. K. Nørskov, and F. Besenbacher, Enhancement of surface self-diffusion of platinum atoms by adsorbed hydrogen, Nature **398**, 134–136 (1999).

Summary

The interest in very small particles, or nanoparticles, originates from their special physical properties. They are not only of fundamental importance, but also of interest for many potential applications such as heterogeneous catalysis. We have used Scanning Tunneling Microscopy (STM) to study the formation and growth properties of very small palladium particles, supported on a flat substrate, TiO_2 (110). The results of these investigations are described in this thesis.

In order to obtain quantitative information from STM images, image processing and pattern recognition techniques are very valuable tools. Chapter 2 describes an algorithm that we developed to automatically determine the positions and sizes of small particles, and other possible nanostructures, in STM images. Using this procedure, first a filtered 'background' image is subtracted from the original STM image to eliminate height variations in the substrate, such as atomic steps. The particles can then be found by discrimination with respect to a threshold height. Once the particles are located, their exact position and size are determined and used for further analysis. This algorithm has been tested and used in the analysis of the measurements described in Chapters 5, 6 and 7.

The preparation of clean, well ordered oxide surfaces is often not straightforward. In that respect the TiO_2 (110) surface is no exception. The equilibrium composition of titanium oxide depends on temperature and partial oxygen pressure. Deviations from the TiO_2 stoichiometry cause changes in color and an increase in electrical conductivity. This is a major advantage as it allows the use of many experimental techniques that require some degree of conductivity. However, it also affects the surface morphology. Using STM we investigated the surface morphology and its dependence on preparation procedures, i.e. sputtering and annealing, in ultra-high vacuum (UHV). This is described in Chapter 3. Low temperature annealing does not completely restore the damage created by sputtering, whereas high temperature annealing results in the loss of oxygen from the crystal. At elevated temperatures in UHV TiO_2 is reduced. At the surface, the reduction results both in isolated atomic size defects which are attributed to oxygen vacancies, and in line defects (added rows). After reoxidation of the crystal the surface is rough.

This can be explained by the nucleation and growth of new layers of oxide.

A different kind of response of the surface to a changing composition is discussed in Chapter 4. In this chapter ex-situ Atomic Force Microscopy (AFM) observations are presented. They show that changes in stoichiometry also affect the morphology of steps on the $TiO_2(110)$ surface. Upon annealing a sputtered stoichiometric surface at $1135\,K$ first hexagonal islands are formed. During further annealing these hexagonal shapes do not simply grow in size. Instead elongated structures form along the [001] direction, and the surface tends to maximize the length of the [001] steps. We propose that the formation of a [001] step allows the surface to make a non-stoichiometric structure without destroying the crystal structure. Finally, after annealing at $1170\,K$, we find that [001] is still a favoured step direction but the elongated structures are no longer formed. We suggest that other structures are formed to accommodate the non-stoichiometry, such as the added rows that were found in Chapter 3.

In Chapter 5 it is shown that vacuum deposition of small quantities of palladium on $TiO_2(110)$ at room temperature leads to the formation of very small 3-dimensional particles. This indicates a Volmer-Weber growth type, and shows that the 'up-step' diffusion barrier for Pd on Pd is low enough to be overcome at room temperature. We studied the thermal stability of these very small palladium clusters. Upon heating, the number of particles decreases and the average size of the particles increases. This corresponds to a decrease of palladium surface area of this model catalyst. An analysis of the decrease in particle density as a function of time cannot be used to distinguish between different kinds of mass transport over the surface, but on the basis of the resulting size distribution we conclude that the coalescence of diffusing particles is the main mechanism. This is supported by a direct observation of mobile clusters. The spatial distribution of the palladium particles shows that diffusion is faster along the [001] direction of the TiO_2 substrate than in the perpendicular [$1\bar{1}0$] direction. Finally, the palladium clusters change their shape as they grow.

The defects on the substrate surface that are created as a consequence of reduction of the oxide crystal in ultra-high vacuum have a very large influence on the growth rate of small palladium particles on $TiO_2(110)$. This is shown in Chapter 6. The level of oxygen depletion depends on the preparation conditions, resulting in either a strongly reduced surface with a high level of oxygen depletion, or a mildly reduced surface with a modest level of oxygen depletion. After deposition of pal-

ladium at room temperature on a mildly reduced titania surface, palladium clusters predominantly cover steps. On a strongly reduced sample, clusters are smaller and distributed more homogeneously. At elevated temperatures the particles grow in both cases, but the growth rate on the mildly reduced surface is higher than on the strongly reduced surface. Finally, on a mildly reduced substrate the particles are flatter than on a strongly reduced substrate. We propose that palladium particles prefer to avoid oxygen vacancies in the substrate. The average distance between defects limits the maximum contact area between particle and substrate. Furthermore the defects limit the mobility and the growth rate of the particles.

In the final chapter of this thesis, Chapter 7, our first results in a study of the effect a H_2 atmosphere on the Pd/TiO_2 model catalyst are presented. We find that annealing a TiO_2 (110) surface at $672\,K$ in 10^{-5}mbar H_2 results in an increased density of so called added rows on the surface, which is indicative of an increased depletion of oxygen of this surface. In the presence of small supported Pd particles, this process proceeds in a similar manner. The shape and growth rate of the Pd particles seem to be unaffected by the presence of hydrogen gas.

In summary, our investigations have shown that the growth process of very small supported particles can be well described in terms of the motion of each particle as a whole. On the atomic scale this motion results from random movements of the particle's own atoms over its own surface. Furthermore, the natural tendency of titanium oxide to form defects on its surface strongly limits the growth rate of supported particles. In this case non-perfectness is a stabilizing factor that may also be important in practical catalysts.

Summary

Samenvatting

De afgelopen jaren heb ik onderzoek gedaan naar zeer kleine palladiumdeeltjes op een substraat van titaanoxide. Deze deeltjes bestaan uit slechts tien tot een paar honderd atomen. Daarmee zijn ze ongeveer een nanometer (0.000001 mm) groot en worden ze ook wel nanodeeltjes genoemd. Nanodeeltjes vertonen vaak fysisch en chemisch gedrag dat afwijkt van de eigenschappen van normale vaste stof, maar ook van de eigenschappen van losse atomen. Door deze speciale eigenschappen zijn dergelijke kleine deeltjes interessant voor een scala van toepassingen. Een van de toepassingen waarin kleine deeltjes veel gebruikt worden, is de zogenaamde heterogene katalyse. Een katalysator wordt gebruikt om chemische reacties te versnellen, zonder daarbij zelf verbruikt te worden. Voor heterogene katalyse is vooral de grootte van het oppervlak van het actieve materiaal van belang. Dat is een van de belangrijkste redenen waarom daarvoor *kleine* deeltjes worden gebruikt, want kleine deeltjes hebben relatief veel oppervlak en weinig volume.

Het onderzoek dat staat beschreven in dit proefschrift, is van fundamenteel wetenschappelijke aard. Het is ons doel geweest om inzicht te verkrijgen in de fundamentele processen die belangrijk zijn op de schaal van nanodeeltjes. Daarom hebben we de palladiumdeeltjes bestudeerd in een geïdealiseerde situatie. Ze liggen op een schoon en vlak oppervlak. In de praktijk, bijvoorbeeld in een echte katalysator, is de geometrie vaak veel complexer.

De palladiumdeeltjes zijn zo klein, dat ze met een conventionele optische microscoop niet meer zijn waar te nemen. Daarom is in dit onderzoek een andere techniek gebruikt, waarmee in principe zelfs individuele atomen nog te zien zijn. Deze techniek, 'Scanning Tunneling Microscopy' ofwel STM, bestaat nog maar sinds het begin van de jaren 80. Toen werd deze uitgevonden door Binnig en Rohrer van het IBM onderzoekslaboratorium in Zwitserland. In een dergelijke microscoop wordt het oppervlak afgetast met de punt van een scherpe naald, die enkele atoomafstanden van het oppervlak verwijderd blijft. Doordat er een elektrische spanning staat tussen de naald en het oppervlak gaat er een elektrische stroom lopen die heel sterk afhankelijk is van de afstand. Deze stroom wordt gebruikt om de variaties in hoogte van het oppervlak te bepalen wanneer de naald

daar overheen wordt bewogen. Om het oppervlak schoon te houden, is het grootste deel van de metingen uitgevoerd in ultrahoog vacuüm. De opstelling die hiervoor gebruikt is, staat beschreven in hoofdstuk 2.

In microscoopbeelden is vaak heel veel te zien. Om uit deze beelden kwantitatieve informatie te verkrijgen, is software voor beeldverwerking en patroonherkenning een zeer nuttig hulpmiddel. In hoofdstuk 2 wordt een algoritme beschreven waarmee automatisch de grootte en positie van kleine deeltjes kan worden bepaald in STM-plaatjes. Dit algoritme is getest, en het blijkt zeer goed te werken. Het is gebruikt om de grote hoeveelheden metingen in de hoofdstukken 5, 6 en 7 te analyseren. De methode is van algemene aard en kan ook worden gebruikt voor de detectie van andere kleine structuren dan de deeltjes die in dit proefschrift beschreven worden.

Een belangrijk deel van het onderzoek is gericht geweest op het prepareren van een geschikt substraat. In dit geval is dat een één-kristallijn oxideoppervlak. Het prepareren van schone, geordende oxideoppervlakken is over het algemeen niet eenvoudig. Het hier gebruikte TiO_2 (110) is daarop geen uitzondering gebleken. De evenwichtssamenstelling van titaanoxide is afhankelijk van zowel de temperatuur als de partiële zuurstofdruk. In het vacuümsysteem is de zuurstofdruk erg laag. Daardoor wordt bij hoge temperaturen de verhouding zuurstof:titaan een fractie lager dan de perfecte 2:1-verhouding. Hierdoor verandert de kleur van het kristal en neemt het elektrische geleidingsvermogen sterk toe. Aangezien dit geleidingsvermogen het mogelijk maakt om een groot aantal verschillende technieken te gebruiken is dit een groot voordeel, maar de veranderde samenstelling heeft ook gevolgen voor de structuur van het oppervlak. Met onze microscoop hebben we onderzocht hoe de uiteindelijke oppervlaktestructuur afhankelijk is van de preparatiecondities. Dit onderzoek staat beschreven in hoofdstuk 3. Aan het oppervlak ontstaan geïsoleerde defecten met de afmeting van ongeveer één atoom. Waarschijnlijk zijn dat ontbrekende zuurstofatomen. Bovendien worden er atoomrijen op het oppervlak gevormd langs de [001]-richting. Wanneer we proberen om het kristal opnieuw te oxideren, wordt het oppervlak ruw. Dit kan worden verklaard door de nucleatie en groei van nieuwe lagen oxide op het kristal.

De metingen die in hoofdstuk 4 worden gepresenteerd, laten zien dat de veranderende samenstelling van titaanoxide ook gevolgen kan hebben voor de voorkeursrichting van stappen op het oppervlak. Als een oppervlak dat eerst door middel van ionenbombardement ruw is gemaakt, slechts 10 minuten wordt verhit

naar 1135 K, geeft het oppervlak de voorkeur aan hexagonale eilanden. Wanneer het kristal verder wordt verhit, worden deze structuren niet alleen groter, zoals gebruikelijk, maar rekken ze ook steeds meer uit langs de [001]-richting. Bovendien worden smalle excursies langs deze richting gevormd. Op deze manier wordt er veel staplengte langs de [001]-richting gecreëerd, en wordt de totale staplengte groter dan 'noodzakelijk'. Wij vermoeden dat het oppervlak door het maken van deze stappen het gebrek aan zuurstof op kan vangen zonder dat daarvoor de kristalstructuur moet worden aangepast. Bij hogere temperaturen is er nog steeds een voorkeur van de stappen voor de [001]-richting, maar de smalle excursies worden niet meer gemaakt. Waarschijnlijk worden er bij deze temperaturen andere structuren gevormd om de veranderende samenstelling op te vangen.

Het maken van kleine palladiumdeeltjes op TiO_2 (110) blijkt relatief eenvoudig. Door het laten neerslaan van palladiumdamp op het oxidekristal worden drie-dimensionale clustertjes gevormd. In hoofdstuk 5 wordt de stabiliteit van deze deeltjes bij hoge temperaturen (400°C) beschreven. Door het kristal te verhitten neemt de dichtheid van deeltjes af, en neemt de gemiddelde grootte toe. Dit betekent dat de hoeveelheid palladiumoppervlak afneemt. In een echte katalysator zou een kleiner oppervlak resulteren in een verminderde katalytische activiteit. We hebben onze metingen van de deeltjesgroei vergeleken met twee verschillende theoretische modellen voor massatransport tussen de deeltjes. Een model gaat ervan uit, dat atomen zich los kunnen maken van de deeltjes en over het substraat lopen. Dit resulteert in rijping. Het andere model gaat ervan uit, dat de willekeurige bewegingen van de atomen aan de buitenkant van het deeltje resulteren in een beweging van het deeltje als geheel, zonder dat de atomen hierbij het deeltje verlaten. In dit laatste model groeien de deeltjes doordat ze samensmelten wanneer ze elkaar toevallig tegenkomen. Het blijkt dat beide modellen de groei van de clusters als functie van de tijd uitstekend kunnen voorspellen. De grootteverdeling van de clusters komt echter het best overeen met het model dat uitgaat van mobiele deeltjes die samensmelten wanneer ze elkaar tegenkomen. Bovendien blijkt uit opeenvolgende plaatjes dat deeltjes inderdaad bewegen. De ruimtelijke verdeling van de deeltjes over het oppervlak laat zien dat ze sneller bewegen in de [001]-richting dan in de richting loodrecht daarop. In de [001]-richting liggen ze namelijk gemiddeld verder van elkaar. De vorm van kleine palladiumclusters verandert ook als ze groeien. De kleinste clusters zijn platter dan de grotere.

De defecten op het substraatoppervlak die worden gevormd als gevolg van

de reductie van het oxidekristal in vacuüm, hebben een zeer grote invloed op de groeisnelheid van kleine palladiumdeeltjes op TiO_2 (110). Dit wordt gedemonstreerd in hoofdstuk 6. Door kleine variaties in de condities kunnen substraatoppervlakken worden geprepareerd waarin veel of juist relatief weinig zuurstof ontbreekt. Na het opdampen van palladium op een slechts licht gereduceerd oppervlak liggen de palladiumclusters vooral langs de stappen van het substraat. Op een sterk gereduceerd oppervlak zijn er na opdampen veel meer deeltjes. Deze deeltjes zijn kleiner, en ze liggen over het gehele oppervlak verspreid. Als het preparaat wordt verhit, groeien de deeltjes in beide gevallen, maar op het licht gereduceerde substraat gebeurt dit veel sneller dan op het sterk gereduceerde substraat. Op het licht gereduceerde substraat zijn de deeltjes bovendien veel platter dan op het sterk gereduceerde substraat. Wij vermoeden dat de palladiumdeeltjes de geïsoleerde zuurstofvacatures in het substraat proberen te vermijden. Het maximale contactoppervlak tussen een deeltje en het substraat wordt daardoor beperkt door de gemiddelde afstand tussen zuurstofvacatures. Bovendien hinderen deze vacatures de deeltjes in hun beweging en veroorzaken deze defecten dus een afname van de groeisnelheid van de deeltjes.

In hoofdstuk 7 worden de eerste resultaten van ons onderzoek naar de invloed van een omgeving van waterstofgas op onze Pd/TiO_2 'modelkatalysator' gepresenteerd. De verwachting was dat de aanwezigheid van het waterstofgas grote invloed zou hebben op de groeisnelheid of op de vorm van de palladiumdeeltjes. Dit bleek niet het geval, althans niet bij de door ons gebruikte druk van 10^{-5} mbar. In deze atmosfeer heeft verhitting naar 400°C wel grote invloed op het oppervlak van titaanoxide. Er worden dan veel rijen gevormd die bij afwezigheid van waterstof pas bij veel hogere temperaturen gevormd zouden worden, als gevolg van een tekort aan zuurstof aan het oppervlak. Dit proces wordt niet versneld of vertraagd door de aanwezigheid van palladiumclusters.

Uit ons onderzoek kan geconcludeerd worden dat de groei van kleine metaaldeeltjes op oxideoppervlakken uitstekend beschreven kan worden op basis van de bewegingen van de individuele atomen waaruit een deeltje bestaat. Verder heeft de natuurlijke neiging van titaanoxide om defecten te maken aan het oppervlak een grote invloed op de groeisnelheid van de metaaldeeltjes. Het niet perfect zijn van het oppervlak is in dit geval een belangrijke stabiliserende factor, die wellicht ook bij praktische katalysatoren van cruciaal belang is.

Nawoord

Een groot aantal mensen heeft een belangrijke bijdrage geleverd aan het tot stand komen van dit proefschrift.

De technische ondersteuning van Hans Zeijlemaker was onmisbaar bij het opbouwen en draaiend houden van de opstelling. Bovendien dacht hij altijd actief mee over de technische en wetenschappelijke problemen die onderweg opdoken. Ook Noëlle Rutte, Maurice van den Boer, Jan ter Beek en Johan Derks ben ik erkentelijk voor de steun die ik van hen gekregen heb. René Koper heeft mij vele malen bijgestaan met de kristallen. Bovendien heeft hij mij meegesleept naar de 22-dorpentocht. De chocolademelk 'plus' die we na afloop dronken, zal zelden zo goed gesmaakt hebben.

De inspanningen van Arie van Kreuningen en Chris Konstapel tijdens hun stageperiode bij AMOLF zijn zeker ook belangrijk geweest. Een groot deel van het proefschrift zal ze dan ook bekend voorkomen. Ook Els Homan mag in dit verband niet onvermeld blijven. Ik heb haar meetprogramma's tot aan het einde van m'n promotie gebruikt. Jürgen Chrost heeft mij er met zijn kritische houding en enorme kennis meerdere keren toe aangezet om de resultaten nog maar eens goed te bekijken. Bovendien heeft hij prachtige metingen gedaan.

Bij het onderzoek was de hulp van de ondersteunende afdelingen onontbeer-lijk. Dankzij het constructiebureau en de werkplaats stond zelfs al voor mijn komst naar AMOLF een groot deel van de opstelling gereed. Hier wil ik in het bijzonder Herman Ficke, Ille Cerjak, Dick Glastra van Loon, Wim Brouwer, Henk Neerings, Wim Barsingerhorn en Jan van der Linden noemen. Ook als we plotseling weer eens iets wilden veranderen, stonden ze voor ons klaar. Dit geldt zeker ook voor de mensen van E&I. In het bijzonder Hans ter Horst, Anton Vijftigschild, Henk Dekker, Guus Ruwiel, Paul van Deenen, Ben Okhuysen, en Jan van Elst, ben ik zeer erkentelijk.

Het omgaan met de kuren van de STM koste in het begin van mijn promotie wel eens wat moeite. Dankzij de 'opvoeding' van Mischa Hoogeman, maar ook die van Menno Chang, is het toch allemaal nog goed gekomen. Bovendien zal ik de skilessen met beide heren tijdens een conferentie in Bulgarije niet snel ver-

geten. De samenwerking met de overige 'STM-ers', Marcel, Raoul, Mark, Joost, Jan, Onno, Bas, Peter, Martin, Jenny, Dennis en Gertjan was gelukkig ook altijd bijzonder prettig. Ik vond het dan ook jammer dat jullie een voor een vertrokken. Voor de goede sfeer, zowel binnen als buiten AMOLF, wil ik ook graag noemen Marcel, Jacob, Dirk, Willem Jan, Steven, Joost, Michel, Paul, Mike, Richard, Martin, Sander, Gerbrand, Cendrine, Astrid, Anand, Marco en Wouter.

Mijn voormalige huisgenoten uit de Hoptille, Wilko, Harro en Pjotr mogen hier uiteraard ook niet ontbreken, want zonder hen had ik het zo net nog niet geweten. Waar al die fantastische gesprekken over gingen is me nog steeds een raadsel, maar ach, dat geeft ook eigenlijk niet. De regelmatige etentjes met Bart en Sander hebben zeker ook meegeholpen om te ontspannen en de stress onder de duim te houden. Nu de druk van de ketel is, zal ik ook weer eens voor hen gaan koken.

Als laatste, maar zeker niet minste, wil ik Hans, Marijke, Rob en mijn vader en moeder bedanken voor alle steun en belangstelling.

Curriculum Vitae

Op 21 april 1971 ben ik geboren in de gemeente Opmeer in Noord-Holland. Na het behalen van mijn VWO diploma aan de scholengemeenschap Oscar Romero in Hoorn in 1989, ben ik begonnen aan de studie Technische Natuurkunde aan de Universiteit Twente in Enschede. In juni 1990 haalde ik daar mijn propedeuse. Tijdens de doctoraalfase van mijn studie heb ik in 1993 een stageperiode van vier maanden doorgebracht bij het Department of Physics and Measurement Technology van de Universiteit van Linköping in Zweden. Hier heb ik onder begeleiding van prof. dr. H. Arwin de elektrochemische oxidatie van titanium bestudeerd met behulp van spectroscopische ellipsometrie. Het afstudeeronderzoek heb ik uitgevoerd in de vakgroep Vastestoffysica van de Universiteit Twente. Gedurende een jaar heb ik daar onder begeleiding van dr. ir. H. Wormeester gewerkt aan een opstelling om met behulp van het magneto-optische Kerr-effect de magnetisatie van dunne lagen te kunnen meten. In 1995 ben ik hierop afgestudeerd bij prof. dr. ir. B. Poelsema.

In juli 1995 ben ik als onderzoeker in opleiding (OIO) begonnen bij het FOM-Instituut voor Atoom- en Molecuulfysica. In de groep Dunne Lagen heb ik onder supervisie van ir. J. Verhoeven en prof. dr. J.W.M. Frenken een ultrahoog vacuüm opstelling opgebouwd en daarin kleine metaaldeeltjes op oxideoppervlakken onderzocht. De opstelling en de resultaten van het onderzoek staan beschreven in dit proefschrift.